Liquid Jet Impingement with Spent Flow Management for Power Electronics Cooling

by

John Franklin Maddox, Jr.

A dissertation submitted to the Graduate Faculty of
Auburn University
in partial fulfillment of the
requirements for the Degree of
Doctor of Philosophy

Auburn, Alabama
August 1, 2015

Keywords: jet impingment, single-phase, spent flow management, angled confining wall, power electronics, local heat flux measurement

Approved by

Roy W. Knight, Co-Chair, Assistant Professor of Mechanical Engineering
Sushil H. Bhavnani, Co-Chair, Professor of Mechanical Engineering
Jeyhoon M. Khodadadi, Professor of Mechanical Engineering
Narendra K. Govil, Professor of Mathematics & Statistics

Abstract

The high levels of heat generated by power electronics, on board electric and hybrid-electric vehicles, require the use of aggressive liquid cooling techniques. Incorporating the electronics cooling into the radiator flow loop is an attractive option, from a manufacturing and cost perspective, because it makes use of the existing infrastructure already on the vehicle. Therefore, it is advantageous to have a liquid cooling solution that can use a water based ethylene glycol mixture. Many of the power electronic components used in vehicles come packaged in modules which spread the heat to a large surface area. Impinging liquid jets provide the highest single-phase heat transfer coefficient at the stagnation point of currently available cooling techniques, which makes them an excellent method for removing the heat from the module surface. Since the rate of heat transfer decreases with distance from the stagnation point, it is necessary to utilize multiple jets in an array to cool large surface areas. However, it is common for the spent fluid from upstream jets to become entrained in downstream jets, successively degrading the performance of each subsequent downstream jet. In order to counteract this effect, an inclined confining wall was used to allow the spent fluid from upstream jets to be diverted around the downstream jets, thus avoiding entrainment and reducing degradation in the heat transfer coefficients of the downstream jets. A measurement technique was developed that allows the local thermal properties to be measured at the impingement surface. This technique was used to measure the effects of jet Reynolds number, confining wall angle, nozzle to plate spacing, and nozzle pitch for single-phase, normal, circular jets. A model was developed in ANSYS® Fluent to support and extended the conclusions of the experimental study. The angled confining wall was found to be an effective method of spent flow management, allowing the nozzles to be placed closer to

each other and closer to the surface without interfering with the performance of neighboring jets.

Acknowledgments

I would like to thank my advisory committee: Dr. Roy W. Knight, Dr. Sushil H. Bhavnani, Dr. Jeyhoon M. Khodadadi, and Dr. Narendra K. Govil with special thanks to Dr. Knight and Dr. Bhavnani for their constant encouragement and guidance throughout my graduate career.

I would also like to thank Zenda Davis, Jordan Roberts, and the rest of my friends and colleagues who have helped me both technically and motivationally on a daily basis.

Most of all I would like to thank my mother, father, and daughter for their endless love, encouragement, support, and patience. I could not have completed this work without their help.

Table of Contents

List of Figures

List of Tables

Nomenclature

Acronyms

API	application program interface
ASM	algebraic stress model
CFD	computational fluid dynamics
DNS	direct numerical simulation
GTO	gate turn-off thyristor
GUI	graphical user interface
HPCC	high performance computing cluster
IGBT	insulated-gate bipolar transistor
IGCT	integrated gate-commutated thyristor
IR	infrared
LES	large eddy simulation
MOSFET	metal-oxide-semiconductor field-effect transistor
PID	proportional-integral-derivative controller
RANS	Reynolds-averaged Navier-Stokes
RNG	renormalization group theory
RSM	Reynolds stress model
RSTM	Reynolds stress transport model
SMC	second moment closure
TIM	thermal interface material
TLC	thermochromic liquid crystals

VFD	variable frequency drive
vSMP	virtual symmetric multiprocessing
WEG	water/ethylene glycol mixture

English Letter Symbols

A	area, m^2
b	intercept in linear regression
C	turbulence model constant
D_n	jet diameter, m
F	turbulence model constant
f	elliptical relaxation function, 1/s
G	generation
H	jet height, m
H_0	initial confining wall height, m
h	local heat transfer coefficient, $W/(m^2 \cdot K)$
$\overline{h}$	mean heat transfer coefficient, $W/(m^2 \cdot K)$
k	thermal conductivity, $W/(m \cdot K)$
k	turbulent kinetic energy, m^2/s^2
L	turbulent length scale, s
L_n	nozzle length, m
m	slope in linear regression
Nu_{D_n}	local jet Nusselt number
$\overline{Nu}_{D_n}$	mean jet Nusselt number
p	pressure, Pa
P	jet pitch, m
$\dot{q}''$	heat flux, W/m^2

Re_{D_n}	jet Reynolds number
S	source term
S	strain rate magnitude, 1/s
T	temperature, °C
T	turbulent time scale, s
Tu	turbulence intensity
u	velocity, m/s
U_n	average nozzle velocity, m/s
$\|\boldsymbol{U}\|$	magnitude of velocity vector, m/s
$\overline{v^2}$	velocity fluctuation normal to the streamlines, m^2/s^2
x	downstream distance from jet array center, m
Y	dissipation
y	distance to closest wall, m
y	transverse distance from jet array center, m
z	vertical distance from impingement surface, m

Greek letter symbols

α	diffusivity
β	diffusion coefficient
δ	uncertainty
ε	turbulent dissipation, m^2/s^3
Γ	effective diffusivity, $Pa \cdot s$
γ	intermittency
μ	dynamic viscosity, $Pa \cdot s$
γ	angle of confining wall, degrees
λ	length scale, m

ν	kinematic viscosity, m^2/s
Ω	vorticity, m/s
ω	specific turbulence dissipation, 1/s
ρ	density, kg/m^3
σ	turbulent Prandtl number
τ	shear stress, Pa
θ	momentum thickness, m
Θ	temperature difference, °C

Superscripts

$+$	nondimensionalized with respect to turbulent length scale
$*$	nondimensionalized with respect to D_n

Subscripts

c	copper
g	thermocouple group
∞	free stream
in	inlet
n	nozzle
s	surface
t	turbulent
TC	thermocouple
w	wall
w	water

Chapter 1

Introduction

1.1 Electronics Thermal Management

As modern electronics have decreased in size and increased in power output, the heat fluxes generated have become too large to be efficiently removed by traditional air cooled thermal management techniques. This has created a demand for more aggressive cooling strategies, many of which incorporate either single phase or two phase liquid cooling.

For a thermal management solution to be attractive, it must first remove the heat generated by the device without allowing the temperature of the device to rise above its acceptable operating range. There exist methods of heat removal that can achieve this goal for any heat flux present in current devices. However, simply removing the heat while maintaining a low device temperature is not the only criterion that must be considered when designing a thermal management solution. Cost, size, weight, complexity, and reliability are confounding factors that limit the applicability of the more aggressive solutions.

As with all engineering decisions, monetary cost is a driving factor that must be considered when designing a thermal management solution. While this is less of an issue for high end specialty products, it is very important for commodity products where the profit margin is already vanishingly small. Particularly in the automotive and consumer electronics industries, a thermal solution will not be economically viable unless its monetary cost is much less than the cost of the overall system.

As we move toward mobile electronics, there is pressure to decrease the size of all the components within the system, including the thermal management portion. Therefore, when one of the more aggressive cooling strategies is being considered, its overall size must be taken into consideration. Although the more advanced liquid solutions provide the opportunity to

have a smaller footprint at the surface of the device than traditional air cooled solutions, they still often require as much or more space for their accompanying infrastructure, i.e. pumps, condensers, etc.

In general the amount of heat that can be removed by a thermal management solution is inversely proportional to its size. The heat that gets generated by a device must eventually be transmitted to the environment. This usually means that at some point in the system, there will need to be a component that rejects heat through convective exchange with the ambient air.

The amount of heat that is transmitted through convection,

$$\dot{q} = hA(T_s - T_\infty),$$

is directly proportional to the area of the convective surface, A, the heat transfer coefficient, h, and the temperature difference between the convective surface and the surrounding fluid, $(T_s - T_\infty)$. It is not cost effective to decrease the temperature of the environment. The temperature of the convective surface is driven by the need to keep the device at a desired temperature. The heat transfer coefficient is usually improved by adding a fan to create forced convection; however, there are limits to how high it can go. This leaves the area as the last option for increasing the heat transfer. The most common method to increase the convective surface area is to incorporate a finned structure which can be optimized, based on the properties of the fluid and fin material, for heat load, volume, mass, etc.

Traditional solutions, such as natural or forced convection heat sinks, interact directly with the device and the environment. Heat is conducted through one or more thermal interface materials and spreaders then into the fins and finally into the environment through convection. The newer, more aggressive solutions move the convective surface away from the device and use a fluid to move the heat from the device to the convective surface. This approach allows the devices to be more tightly packed because the footprint and volume of

the portion of the liquid cooled system that interacts directly with the device can be much smaller than an equivalent air cooled heat sink. However, this does not remove the need for the convective heat sink, it just allows it to be placed in a more convenient location rather than directly on top of the device. Therefore, the more advanced cooling solutions will be larger than the traditional solutions because they will have approximately the same size and mass associated with the convective surface plus the additional size and mass of the supporting components.

The reliability of a thermal management solution and the cost of failure must also be taken into account when considering some of the more aggressive thermal management solutions. The more complex a system becomes, the more opportunity there is for one of its components to fail, i.e. pump failure, leaking fluid, flow instabilities, vapor flooding, flow obstructions, interface degradation, etc. When a thermal management solution fails, depending on the mode of failure, it can lead to a gradual or immediate rise in temperature of the device. Depending on the application and mode of failure, the consequences of this temperature rise can range from increased internal mechanical stresses to temporary inoperability to permanent catastrophic damage.

1.2 Automotive Power Electronics Cooling

Power electronics such as metal-oxide-semiconductor field-effect transistors (MOSFETs), gate turn-off thyristors (GTOs), insulated-gate bipolar transistors (IGBTs), and integrated gate-commutated thyristors (IGCTs), on board modern electric, hybrid-electric, and military vehicles dissipate large amounts of heat during operation and need to be actively cooled to improve both reliability and performance. The heat fluxes of these devices are too high to be removed with convective air cooling techniques; therefore, it is necessary to utilize liquid cooling [1–4].

Many power electronics, such as the IGBT module shown in Figure 1.1, are packaged in a module with an integrated metal plate which acts as a heat spreader to conduct the heat

away from the silicon device. One method to remove the heat from the metal plate is to attach the module to a liquid cooled cold plate with a thermal interface material (TIM) to minimize the contact resistance. However, even with the use of a TIM, the contact resistance between the module and the cold plate can be a significant portion of the total thermal resistance of the system. Additionally, the TIMs used for this purpose have performance and reliability concerns, such as pump-out and dry-out [4–6]. An alternative approach is to bring the liquid coolant into direct contact with the heat spreader, rather than isolating it in a cold plate [3, 4]. This completely removes the TIM from the heat path, thus decreasing the total thermal resistance and eliminating the reliability concerns associated with TIMs.

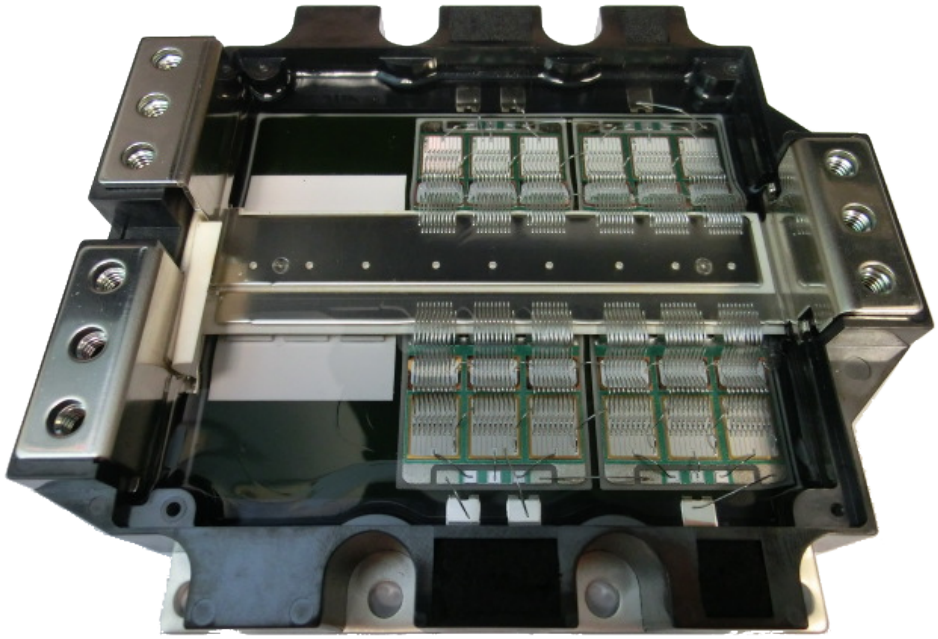

Figure 1.1: IGBT module [6]

Microchannels and jet impingement arrays have emerged as the preferred methods for high performance single-phase liquid cooling applications. While both methods can be used to achieve high levels of heat transfer, the fundamental differences in their approaches make them better suited for different types of applications. In comparison to each other, microchannels operate with lower flow rates and higher pressure drops; while jet impingement systems operate with higher flow rates and lower pressure drops, which is desirable from a

fluid containment point of view. It has been shown that microchannels offer better performance for smaller surface areas, while jet impingement arrays are preferable when the target dimension is larger than 0.07 m by 0.07 m if proper treatment is applied to the spent flow after impingement [7, 8].

In the context of vehicular electronics cooling, it is desirable to utilize the engine coolant that is already present. By incorporating the electronics directly into the radiator flow loop, the need for a dedicated electronics cooling flow loop is removed. This decreases the manufacturing, maintenance, and operational costs by reducing the number of components on the vehicle. Therefore, it is desirable to have a liquid cooling solution that can use a water based ethylene glycol mixture (WEG) with a flow rate and pressure drop that is compatible with the existing infrastructure on board modern vehicles, which has made jet impingement the preferred technique for this type of system [2, 3, 6].

Chapter 2

Background

An impinging jet is a stream of fluid, directed at a surface. The stream is often formed by forcing the fluid through an orifice or a nozzle. Normal jets are perpendicular to the surface, while oblique jets approach from an angle. Depending on the method and rate of spent flow removal, the fluid may operate as either a free jet or a submerged jet. A number of reviews have discussed the performance and use of impinging jets for a range of heat and mass transfer applications [9–14].

2.1 Impinging Jet Regions

Submerged jets go through a number of distinct flow regions driven by different physical mechanisms. The shape, size, and transfer properties of the different regions are dependent on the geometry and flow properties of the jet or jet array. The design of an effective jet impingement system requires an understanding of the behavior of each of the regions and their effects on the overall transfer characteristics of the flow.

2.1.1 Free Jet

As the fluid leaves the orifice or nozzle and approaches the surface, a shearing layer forms due to viscous effects between the jet and the surrounding fluid, as shown in Figure 2.1. This causes momentum from the jet to be transferred to the surrounding fluid. The shearing layer thickness grows with distance from the nozzle outlet. As a result, the portion of the fluid unaffected by the viscous effects, called the potential core, decreases in thickness with distance from the nozzle outlet. The core is defined as ending at the axial position where the centerline flow dynamic pressure reaches 95% of its original value [14].

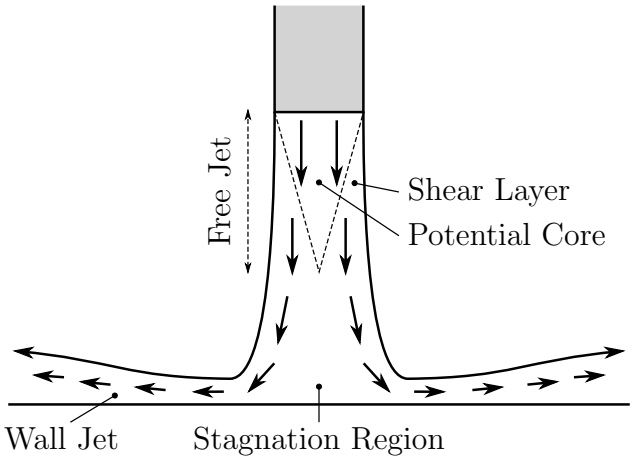

Figure 2.1: Regions of an impinging jet

The velocity profile at the exit of the nozzle can have a significant impact on the development of the free jet and the magnitude of the heat transfer at the surface. In general it is preferable to have a wide path for the incoming fluid with a sharp reduction in cross-sectional area prior to exiting the nozzle. This can be achieved by having a sharp edged orifice at the exit of the nozzle. Although the pressure drop is larger for the orifice, is has been shown that orifice plates produce higher rates of heat transfer than smooth pipes with fully developed velocity profiles at the nozzle exit [15–17].

2.1.2 Decaying Jet

The core typically extends four to eight nozzle diameters from the nozzle exit [14]. If the core ends prior to impinging on the surface, the jet will enter a region of core decay. In this region, the axial velocity decreases and the width increases with axial distance from the nozzle exit. The velocity profile in the decaying jet region has been described by Martin [10] and Viskanta [12], with the fully developed flow reaching a Gaussian velocity profile.

2.1.3 Stagnation Region

When the fluid stream reaches the surface, it is forced to change direction and flow parallel to the surface. The region near the surface where the fluid changes direction, called

the stagnation or impingement region, produces the highest local heat transfer coefficient of currently available single-phase cooling technologies. The stagnation region is expected to extend 1.2 nozzle diameters from the surface [10]. As a way to define the start of the stagnation region, Maurel and Solliec [18] identified it as having a negative normal-parallel velocity correlation. When the nozzle exit is within two jet diameters of the surface, the high static pressure in the stagnation region can effect the fluid at the nozzle exit, which prevents the formation of a free jet region [14].

2.1.4 Wall Jet

After the fluid leaves the stagnation region, it flows parallel to the surface in a region called the wall jet. Viscous effects from the surrounding fluid and the no-slip condition at the surface cause a boundary layer to form in the wall jet region. As a result, the heat transfer coefficient decreases with distance from the stagnation region. The wall jet boundary layer begins within the stagnation region, at a distance of 0.75–3 diameters from the jet axis [14], and has an initial thickness of no more than 1% of the jet diameter [10]. For round jets the fluid experiences additional deceleration due to mass conservation as it spreads outward.

2.1.5 Fountain

Since the velocity and heat transfer coefficient decrease with distance from the stagnation region, multiple jets are often used to cool large surface areas. When the wall jets from neighboring nozzles in an array collide, the fluid changes direction and flows away from the surface, forming an inverted jet called the fountain region, as illustrated in Figure 2.2. For closely spaced jets, the fountain may be close enough to exchange momentum with the free jet, which results in decreased heat transfer at the surface [19]. When the fountain occurs far away from the free jet, the second stagnation region that forms at the base of the fountain can have a heat transfer rate comparable in magnitude to the impingement region [14].

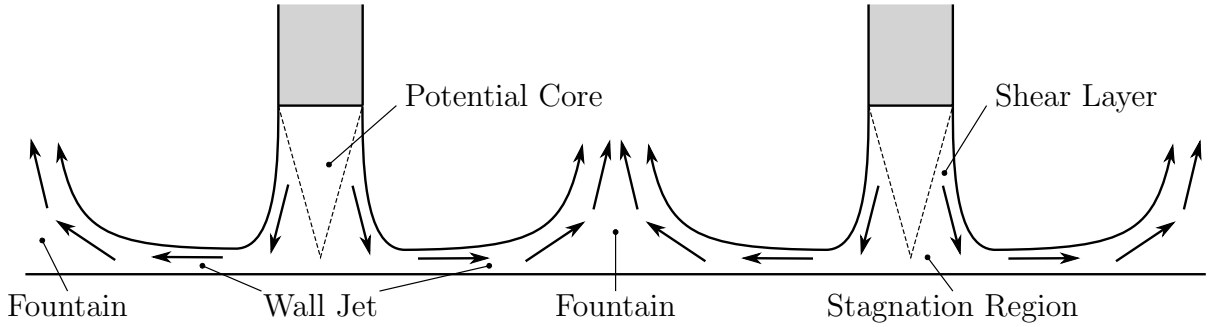

Figure 2.2: Regions of an array of impinging jets

2.1.6 Spent Flow

When the fluid leaves the fountain region it is referred to as spent fluid and must be removed from the system. The method by which the spent fluid is removed can have detrimental effects on the total heat transfer of the array if care is not taken to avoid interfering with the incoming jets.

When a common outlet is used for the spent fluid from multiple jets, complex interactions take place as the spent fluid from upstream jets combines with the spent fluid from downstream jets while moving toward the outlet. The spent fluid from upstream jets can become entrained in and alter the trajectory of downstream jets, as shown in Figure 2.3, causing a degradation of the heat transfer within the stagnation region of the downstream jets. At the same time, the increased velocity of the bulk fluid moving parallel to the surface toward the outlet can have a beneficial effect on the heat transfer in the wall jet region.

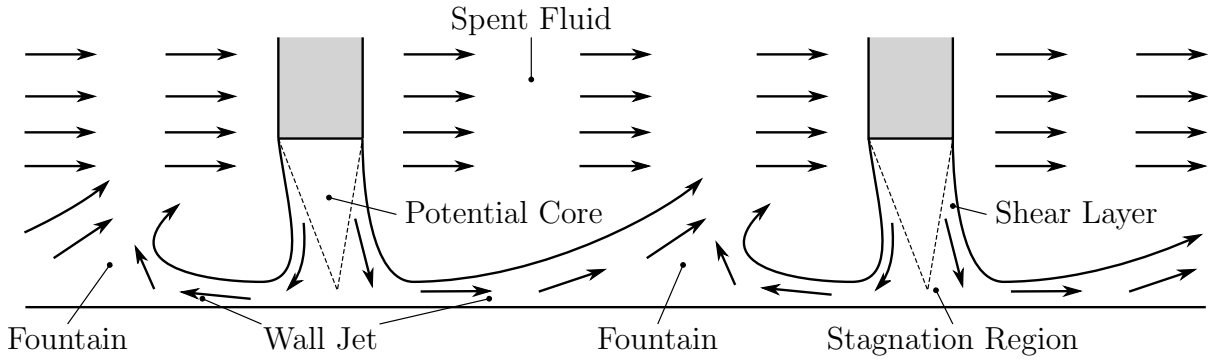

Figure 2.3: The effects of crossflow on an array of impinging jets

Spent fluid flowing perpendicular to the downstream jets is often referred to as crossflow. Aldabbagh and Sezai [20] reported that the presence of crossflow decreases the average heat transfer of a jet but not necessarily the magnitude of the local maxima, and Huber and Viskanta [21] found that the negative impacts of the crossflow come from interactions with the free jet prior to impingement, not from the crossflow interacting with the wall jet. For extremely high levels of crossflow, Chambers et al. [22] showed that the transfer rates reduced to that of film cooling with the impinging jets having negligible impact. Florschuetz et al. [23, 24, 25] measured the downstream displacement of the local heat transfer maxima and the effects of spacing the jets to create channels for the crossflow to be diverted away from the free jet regions.

2.2 Turbulence Effects

The presence of turbulence in the stagnation region and the wall jet region greatly enhances the thermal transport characteristics of jet impingement systems. Purely analytical solutions exist for lower velocity, laminar jets. However, higher velocity, turbulent jets provide more heat transfer at a given flow rate than laminar jets. Because of this, there is much more industrial and academic interest in turbulent jets. The analysis and modeling of turbulent flow is much more challenging than laminar flow, and as a result, the majority of tools for analyzing these flows are at least partially empirical in nature.

The turbulence of an impinging jet is directly related to the jet Reynolds number,

$$Re_{D_n} = \frac{U_n D_n}{\nu} \tag{2.1}$$

where U_n is the mean nozzle exit velocity, D_n is the inside diameter of the nozzle, and ν is the kinematic viscosity. The transition from laminar to turbulent flow can be predicted by the Reynolds number: for $Re_{D_n} < 1000$ the flow will be laminar and for $Re_{D_n} > 3000$ the flow will be fully turbulent, with a transition region existing for $1000 < Re_{D_n} < 3000$ [12].

The turbulence of the incoming fluid prior to entering the jet flow field can have a significant impact on the heat transfer at the surface. Turbulence can be induced upstream of the nozzle exit by the method of flow distribution or intentionally enhanced by inserting obstructions. Gao and Voke [26] experimentally showed that this has the effect of shortening the core length, which reduces the optimal height of the nozzle exit.

Turbulence is generated in the free jet region by the shear flow on the edges of the jet. This causes the formation of downstream eddies with a length scale on the order of magnitude of the jet diameter [14]. Hoogendoorn [27] experimentally showed that the formation of turbulence in the free jet affected both the profile and magnitude of the heat transfer at the surface.

In the stagnation region, the strains and stresses induced by the pressure gradient cause additional turbulence in the flow. Abe and Suga [28] showed numerically that large scale eddies dominate the heat transfer in the stagnation region, in contrast to the shear dominated heat transfer in the fully developed wall jet region.

For laminar jets, the wall jet has similar behavior to external flow along a flat plate. As the boundary layer forms, the laminar flow can transition to turbulent as the flow moves radially outward from the nozzle. Cooper et al. [29] show that for transitional or turbulent jets, the turbulence already present in the flow as it approaches the wall can cause large fluctuations in the velocity component normal to the wall. Secondary peaks in the wall jet have been observed and attributed to the turbulence effects in the wall jet [30–32]. Zuckerman and Lior [14] numerically predicted the location of the secondary peak, which agreed with the experimental results of Narayanan et al. [33].

2.3 Geometric Optimization

Decreasing the pitch between jets in an array increases the number of stagnation regions, which is beneficial due their high local rates of heat transfer. However, decreasing the pitch also makes it harder to remove the spent fluid without interfering with the incoming fluid,

which decreases the local rate of heat transfer in the stagnation regions. The effects from these interactions play a minor role when the spacing between jets is greater than eight jet diameters [14].

Decreasing the jet height, the distance the incoming fluid needs to travel before impinging on the surface, improves the local heat transfer in the stagnation region. However, for the case of orifice plates, decreasing the jet height also brings the confining wall closer to the surface, which impedes spent flow removal and degrades the overall heat transfer. The effects from interaction are greatest when the jet exit is less than two jet diameters from the surface [14].

Using nozzles that extend from a confining wall allows the jet height and the channel height to be adjusted independently. Increasing the confining wall height allows for the benefits of the small jet height while still allowing enough room for the spent fluid to avoid the incoming fluid. However, increasing the confining wall height also decreases the free stream velocity of the bulk fluid as it moves toward the exit, which decreases the heat transfer rate in the wall jet regions.

When employing a common outlet for the spent fluid, each successive downstream jet introduces more fluid into the bulk free stream fluid. This has the effect of successively increasing the volumetric flow rate and velocity of the bulk fluid. It is desirable for the bulk fluid velocity to be high enough to enhance the heat transfer in the wall jet region, but not so high that it degrades the heat transfer in the stagnation region. The momentum ratio of the spent fluid to the incoming fluid is the parameter that drives the optimum height of the confining wall. However, as the spent fluid accumulates more mass, its momentum will increase for a channel with a constant cross-sectional area. As a result, there is not a single height that will be optimal for each nozzle in the downstream direction of a jet array with a common outlet. Rather each downstream nozzle would need a larger confining wall height to maintain the optimum momentum ratio. In order to accommodate this need by maintaining a more uniform spent flow momentum with downstream position, an *angled confining wall*

was used in this work to provide enough relief for the spent fluid to avoid the incoming jet while still maintaining a high enough bulk velocity to enhance the wall jet.

2.4 Alternate Geometries and Enhancements

A wide range of variations on the simple jet geometry discussed above have been investigated. The variations from the simple geometry are made to either enhance the heat transfer or to implement impinging jets in applications with a functional requirement that precludes the use of a simple flat surface. One application that has received a great deal of attention is the jet impingement cooling of turbine blades. Actively cooling the inside surface of turbine blades with high pressure bleed air allows the working fluid to enter the turbine at a higher temperature than the material of the turbine blades would have been able to withstand otherwise, which yields a higher efficiency for the turbine [34–36]. The curved surface of these turbine blades has motivated research into jet impingement onto both concave and convex surfaces [16, 37–41]

Altering the profile of the incoming fluid prior to injection into the flow field can enhance the heat transfer at the surface [42]. Lee et al. [43] found that swirl created a more uniform heat transfer for jet heights less than two jet diameters and that the beneficial effects of swirl disappeared for jet heights greater than 6 jet diameters. Nozaki et al. [44] showed a decrease in the heat transfer of the stagnation region of a swirling jet, possibly due to recirculation.

Hwang et al. [45] used a secondary coaxial nozzle to inject a high speed annular flow near the outside of the main jet stream. This had the effect of delaying the development of the shearing layer in the free jet, which allowed the nozzle exit to be placed farther from the surface without reducing the heat transfer. Ichimiya [46] used an annular jet to get a more uniform spreading of the heat transfer at the expense of a local minimum at the axial center due to the formation of a central fountain. A drawback to both of these approaches is the additional pressure drop associated with the increased wetted surface in the nozzle.

Oblique jets impinge on the surface at an angle other than 90°. This type of configuration may be used to accommodate functional requirements of the device being cooled, to achieve a more favorable inlet or exit condition, or to reduce jet-to-jet interaction. Decreasing the angle of incidence changes the shape of the surface heat transfer profile with the local maximum moving downstream [47–49] and the upstream side of the local heat transfer distribution being less sensitive to the change in angle than the downstream side [50]. The total heat transfer of a jet decreases with decreasing angle of incidence [51].

Varying the flow conditions with time can result in transient behaviors with an increase in heat transfer compared to steady state jets. Wen [52] coupled a swirling flow with a surface vibrating at 10 Hz to increase the heat transfer by 20%. Bart et al. [53] also demonstrated a 20% increase in heat transfer by pulsing the flow at frequencies between 200 and 400 Hz for jet heights in the range of four to six jet diameters.

The total heat transfer at the surface can be increased by adding surface features which increase the available area for heat transfer. Taslim et al. [54] showed that, for jet impingement onto a surface with conical bumps, the heat transfer per unit area was unchanged, but the increase in exposed surface area caused an increase in the total heat transfer. Adding fins to the impingement surface can increase the surface area and increase the rate of heat transfer outside the stagnation region due to an increase in turbulence, but it can also cause the momentum to disperse more quickly which decreases the heat transfer within and far away from the stagnation region [55]. El-Sheikh and Garimella [56] showed that adding pin fins to the surface can help to mitigate the detrimental jet to jet interaction effects. Issa and Ortega [57] reported that the pressure loss associated with introducing square pin fins on the surface was driven by the spacing between the fins and was insensitive to Reynolds number. Liu et al. [58] showed that placing fins directly underneath a jet decreases the heat transfer, whereas placing fins outside the stagnation region increase the heat transfer. Ndao et al. [59] reported a 200% increase in heat transfer for a single jet by augmenting the surface

with micro pin fins. Narumanchi et al. [60] reported a 45% decrease in thermal resistance by impinging WEG onto a microfinned copper plate.

The detrimental effects of crossflow on the heat transfer of downstream jets have inspired a number of approaches to manage the spent fluid. One of the more popular approaches is local removal of the spent fluid from each jet, with the goal of having each jet operate as a unit cell in isolation from the other jets [61–63]. However, the current study will be looking at using an angled confining wall create a favorable flow pattern for spent flow management.

2.5 Experimental Techniques

There are two main approaches for experimentally analyzing the surface heat transfer in jet impingement systems, optical techniques and contact techniques. In contact techniques, one or more temperature sensors are placed on or near a heated surface that is being cooled by an impinging jet. For large target areas, the flow can be translated relative to the temperature sensor to increase the spatial resolution of the measured temperature profile [64, 65]. This study will combine a local heat flux meter with the translation technique to obtain a two-dimensional map of the local temperatures and local heat fluxes at the surface.

For optical methods, such as thermochromic liquid crystals (TLC), infrared (IR) radiometers, and thermal paints, a full field temperature profile can be obtained for the surface [66–68]. Thermal paints and TLCs change color with changing temperature. By calibrating the color change, a temperature profile of a surface can be extracted by post-processing an image [69]. However, the full change in color tends to take place over a small temperature range. When the temperature variation of the surface is greater than the range of the color changing material, the experiment must be run at multiple different heat fluxes to measure the different regions of the flow. The results are then adjusted and superimposed on each other to produce a full data set. This has the effect of turning a constant heat flux experiment into an almost constant temperature experiment [14]. An alternate approach is to use multiple materials with overlapping color ranges to measure the full profile in one

experiment, however this requires advance knowledge of the expected magnitude and shape of the temperature profile that will be generated.

2.6 Modeling

Having the ability to accurately predict the performance of a jet impingement system is critical to the design process because it greatly reduces the amount of time and money that must be spent on costly hardware testing. While purely analytical models exist for laminar jets [70], most jet impingement systems are designed to be turbulent over the entire flow field due to the performance enhancements provided by the turbulence. The turbulent portion of the flow field provides the greatest challenge in the effort to develop predictive models [14, 71].

2.6.1 Direct Numerical Simulation (DNS)

The full Navier-Stokes equations can be solved using direct numerical simulation (DNS) to give the most accurate solution of currently available methods. However, doing so requires a very fine grid to accurately capture the microscopic turbulent length scales that drive the behavior of the macroscopic system. This results in CFD problems with prohibitively large numbers of nodes, which must be solved using a supercomputer and even then are still limited to impractically low Reynolds numbers. Because of these limitations, the DNS approach is currently limited primarily to problems of academic interest only.

2.6.2 Large Eddy Simulation (LES)

Large eddy simulation (LES) is a method for reducing the computational load associated with solving the full Navier-Stokes through DNS. The LES model uses sub-grid-scale equations to estimate the effects of the microscopic turbulent length scale while solving the full flow field for the larger length scales. This greatly reduces the number of nodes required when compared to the DNS method; however, it still requires very high resolutions in both

space and time to produce a stable and accurate solution. Therefore, the LES model is still very computationally expensive, and its use is also currently limited to supercomputers. For cases when the computational resources are available, the LES method provides more information about the physics of the flow field than other modeling techniques and has enabled a better understanding of the effects of large turbulent structures on the transfer rate at the surface [26, 28, 72–75].

2.6.3 Reynolds-Averaged Navier-Stokes (RANS)

The high time resolution requirement of the DNS and LES methods can be relaxed by solving for a time-averaged steady-state solution. This is usually done with Reynolds-averaged Navier-Stokes (RANS) models, which account for turbulence using either a two-equation eddy-viscosity model or a full second moment closure (SMC) model. The eddy viscosity models assume the turbulent viscosity can be treated as an isotropic scalar quantity; whereas, the SMC models account for anisotropic turbulent viscosity, but they require semi-empirical equations for calculating the stresses.

The region very close to the surface is of great importance for predicting both the flow patterns and the heat transfer of an impinging jet [76], because the heat transfer rates within the viscous sublayer are significantly higher than in the other regions of the flow. The problem is that the turbulence models tend to be the least accurate in the viscous sublayer, which is the region where accuracy is most needed for jet impingement applications. The two methods to account for this are to either refine the mesh near the wall to fully resolve the viscous sublayer or to use wall functions to predict the properties of the viscous sublayer. The standard logarithmic law of the wall was developed for parallel flow and does a poor job of predicting the shear stress in the stagnation region of impinging jets. Bouainouche et al. [77] proposed a hybrid law of the wall that uses a non-equilibrium law of the wall in the stagnation region and the standard logarithmic law of the wall in the wall jet region.

Esch and Menter [78] used a scalable wall function to force the first node to lie outside the viscous sublayer.

k-ε

The k-ε model solves for the turbulent kinetic energy, k, and the turbulent dissipation, ε. It has been widely acknowledged as doing a poor job of predicting the performance of jet impingement systems [14]. This conclusion has been reached after a great deal of effort went into modifying it to be applicable for this use case. Heyerichs and Pollard [79] reported poor results from augmenting the k-ε model to use three different wall functions and five different damping functions. Craft et al. [80] reported that the k-ε model overestimates the turbulent kinetic energy in the stagnation region due to the way it relates the turbulent kinetic energy to the turbulent viscosity. Turgeon and Pelletier [81] used an adaptive model to show that the shortcomings of the k-ε model are independent of spacial resolution, with errors persisting for small mesh sizes. Merci et al. [82] developed a non-linear k-ε model which overpredicted the heat transfer at the stagnation point. Souris et al. [83] showed that the downstream solutions for the k-ε model are particularly sensitive to upstream errors. Tzeng et al. [84] used seven different damping functions to modify the k-ε model with some of the modifications providing local improvements to portions of the flow, but none of them improved the solutions over the full surface. In general, the shortcomings of the k-ε model are attributed to the isotropic assumption and the poor prediction of the behavior near the wall.

Renormalization Group Theory *k-ε*

The Renormalization Group Theory (RNG) k-ε model modifies the standard k-ε model to include an additional term that helps to account for the contributions from different length scales. Heck et al. [85] reported an improvement in the prediction of heat transfer in the wall jet region using the RNG model, but it still did a poor job of predicting the performance

in the stagnation region. The errors in the RNG solution are attributed to its tendency to overestimate the jet spreading rates.

k-ω

The k-ω model solves for turbulence intensity, k, and specific dissipation, ω. Park et al. [86] reported improvements over the k-ε model when using the k-ω model, but the k-ω model incorrectly predicted the location of the secondary peak in the heat transfer. Heyerichs and Pollard [79] also report improvements over the k-ε model and an incorrect location of the secondary peak. Apart from predicting the incorrect location of the secondary peaks, the k-ω model is also sensitive to far field boundary conditions [14].

Realizability Limits

For flows with high strain rates, some of the turbulence models can produce unrealistic normal Reynolds stress. This can be accounted for by placing realizability limits on these terms [87]. Abdon and Sundén [88] reported improvements to nonlinear k-ε and k-ω models by applying realizability limits. Park and Sung [89] applied realizability limits through a turbulent viscosity damping function to improve the prediction near the wall.

2.6.4 Algebraic Stress Models (ASM)

Algebraic Stress Models (ASM) reduce the computational costs of a CFD solution by solving a set of algebraic equations rather than the complete transport equations. This approach requires advanced knowledge of the expected turbulent length and time scales in order to calculate the other turbulence terms. Funazaki and Hachiya [90] reported improvements over the k-ε and RNG k-ε models using an ASM. Souris et al. [83] report improved predictions by an ASM in the free jet region when compared to the k-ε.

2.6.5 Reynolds Stress Transport Models (RSTM)

Reynolds Stress Transport Models (RSTM), or SMC Reynolds Stress Models (RSM), eliminate the isotropy assumption inherent in the two equation models by tracking all six components in the Reynolds stress tensor. Because of this, the RSM has the potential to give better predictions for the turning flow in the stagnation region of impinging jets than the two equation models. Craft et al. [76] reported that the errors from an RSM had a strong dependence on the distance between the nozzle exit and the surface, with errors ranging from 25% to 100% depending on the jet height. Shi et al. [91] reported that the RSM predicted the secondary peak in heat transfer at the wrong location. In general, the RSMs do not give a large enough improvement in accuracy to justify the additional computational expense.

2.6.6 v^2f

Durbin's v^2f model, or the normal velocity relaxation model, augments the k-ε model by adding two additional equations, making it a four equation model [32, 92, 93]. The v^2f model uses the velocity fluctuation normal to the streamlines, $\overline{v^2}$, to calculate the turbulent eddy viscosity. The use of $\overline{v^2}$ rather than k as the velocity scale near the surface provides damping of the turbulent transport near the wall. The anisotropy of the flow near the wall is accounted for by an elliptical relaxation function, f, which captures the effects of the wall on the fluctuation of $\overline{v^2}$. A major benefit of the v^2f model is that it can be applied all the way up to an impermeable surface, without the need to include a wall function for the viscous sublayer. Thielen et al. [94] showed that the v^2f model predicted realistic levels of turbulence in the decelerating jet core, which cannot be said of any of the k-ε or k-ω variants, but can over predict the turbulence in the shearing layer outside the core. The v^2f model is also inherently less stable and more sensitive to initial conditions than the two equation models, so it is recommended to start with a converged flow field produced by one of the simpler models, such as the k-ε model [95]. Despite added computational cost from the need

to have a very fine grid at the surface and the two additional equations, the v^2f model is recognized as one of the best choices for modeling jet impingement systems [34].

2.6.7 Hybrid Models

While none of the two equation turbulence models provide accurate solutions over the entire flow field, some of them can be tuned to provide acceptable results in one of the regions of the impinging jet. With this knowledge, hybrid CFD models can be developed that apply different sets of specialized equations for the free jet, the stagnation region, and the wall jet based on calculations to determine in which region the nodes are located. The local results from each of the regions are then combined with smoothing at the boundaries to create a consolidated solution for the whole flow field. Menter [96] proposed a hybrid model known as, Menter's shear stress transport (SST) model or the transition shear stress transport model, which uses the k-ω model near the wall and the k-ε model far away from the wall with a weighting function to blend the two solutions based on distance from the wall and a modified equation for calculating the turbulent viscosity to accommodate an adverse pressure gradient. Esch and Menter [78] showed that the SST model predicted heat transfer rates within 5% of those predicted by Durbin's v^2f model. Since the SST model requires less computational resources than the v^2f model, the small decrease in accuracy may be an acceptable compromise in some cases.

2.6.8 Summary

Impinging jets are particularly challenging to model due to the fundamental differences between the different regions of the jet. A great deal of effort has gone into developing a model that can quickly and accurately predict the performance for the whole flow field, without having to resort to the prohibitively expensive DNS or LES time-variant models. While two models have emerged as the preferred choices, SST and v^2f, they are still not perfect and depend on a number of empirically determined constants. The strengths and weaknesses

of the turbulence models commonly used for jet impingement studies were compared by Zuckerman and Lior [14, 34] and are reproduced here in Table 2.1.

2.7 Objective of Current Study

Increasing the number of jets per unit area, or decreasing the spacing between jets in an array, allows more uniform cooling of the surface. However, as jets are placed closer to each other, the local heat transfer from each jet decreases due to the effects of jet-to-jet interaction.

There are two main mechanism through which jet-to-jet interaction can decrease the heat transfer at the surface. For highly confined flows, the spent fluid from upstream jets forms a crossflow that can divert or become entrained in downstream jets, which decreases the rate of heat transfer in the stagnation region of the downstream jets. This effect is exacerbated by the increase in momentum of the crossflow as each row of jets adds to the mass of the spent fluid. For closely spaced jets, the fountain between the jets can exchange momentum with and slow down the fluid in the free jet, which also decreases the rate of heat transfer in the stagnation region.

In order to mitigate the negative effects of the jet-to-jet interaction, this work will use an angled confining wall with nozzles extending from the wall normal to the surface, as illustrated in Figure 2.4. By having the nozzles extend from the confining wall, the jet height is decoupled from the confining wall height, which allows the nozzle exit to be brought closer to the surface without the heat transfer being degraded by crossflow. The angled confining wall causes the cross-sectional area of the channel for spent flow to increase with downstream position. This helps to maintain a constant momentum ratio of the crossflow and the free jet, even as each row of jets increases the crossflow mass flow rate. The walls of the nozzles protect the incoming fluid from the crossflow and minimize the opportunity for momentum exchange between the free jet and the fountain. These three effects make the proposed geometry a

Table 2.1: Comparison of CFD turbulence models used for jet impingement problems [14]

Turbulence model	Computational cost (time required)	Impingement jet transfer coefficient prediction	Ability to predict secondary peak
k-ε	★★★★ Low cost	★ Poor: Nu error of 15–60%	★ Poor
k-ω	★★★★ Low–moderate	★★ Poor–fair: anticipate Nu errors of at least 10–30%	★★ Fair: may have incorrect location or magnitude
Realizable k-ε and other k-ε variations	★★★★ Low	★★ Poor–fair: expect Nu errors of at least 15–30%	★★ Poor–fair: may have incorrect location or magnitude
Algebraic stress model	★★★★ Low	★★ Poor–fair: anticipate Nu errors of at least 10–30%	★ Poor
Reynolds stress model (full SMC)	★★ Moderate–high	★ Poor: anticipate Nu errors of 25–100%	★★ Fair: may have incorrect location or magnitude
Shear stress transport (SST), hybrid method	★★★ Low–moderate	★★★ Good: typical Nu errors of 20–40%	★★ Fair
v^2f	★★★ Moderate	★★★★ Excellent: anticipate Nu errors of 2–30%	★★★★ Excellent
DNS/LES time-variant models	★ Extremely high (DNS available for low Re only)	★★★★ Good–Excellent	★★★★ Good–Excellent

★: undesirable model characteristics
★★★★: excellent model characteristics

simple method for spent flow management that avoids the need to locally remove the spent fluid from each jet.

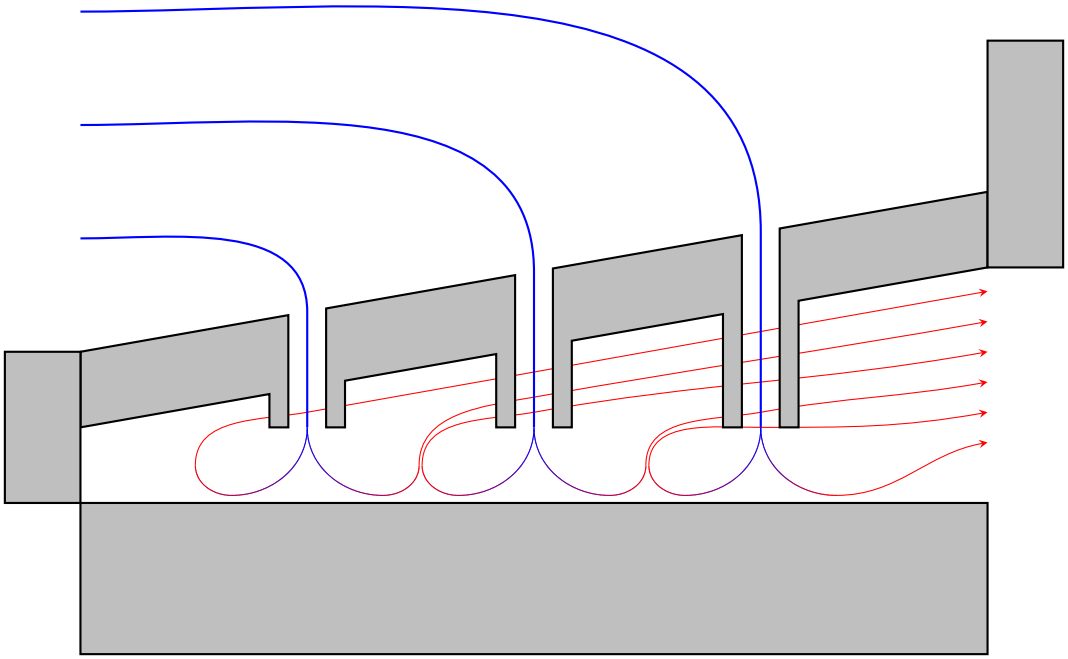

Figure 2.4: 2-D representation of desired flow pattern with an angled confining wall

Chapter 3

Experimental Methodology

3.1 Jet Plates

In order to characterize the effects of jet-to-jet interaction, it is necessary to have at least one neighboring jet on each side of the jet being measured. Therefore, a 3×3 array of jets, as shown in Figure 3.1, was used for the experimentation, with the central jet being the focus of the study. Spatial locations were described by a Cartesian coordinate system with its origin on the impingement surface at the axial center of the central jet with the x-direction toward the spent flow exit and the z-direction perpendicular to the surface.

The characteristic length of jet impingement systems is the diameter of the nozzle exit, D_n. The remaining geometric parameters, shown in Figure 3.2, were nondimensionalized by dividing by the characteristic length: $P^* = P/D_n$, $H^* = H/D_n$, $H_0^* = H_0/D_n$, and $L_n^* = L_n/D_n$.

Each jet plate confining wall was constructed from acrylic with a thickness of 5.715 mm (0.225"). The nozzles were fabricated from acrylic tubing with an inside diameter of 3.175 mm (1/8") and an outside diameter of 6.35 mm (1/4"), which was the smallest diameter readily available at the time of fabrication. The remaining dimensions of the experimental system were driven by the inside nozzle diameter.

3.2 Flow Chamber

The flow chamber, shown in Figure 3.3 and Figure 3.4, was designed to accommodate a 3×3 array of jets with a pitch of $P^* \leq 8$ and a jet height of $H^* \leq 6$. The width was limited to eight jet diameters because the effects of jet-to-jet interaction are minimal beyond

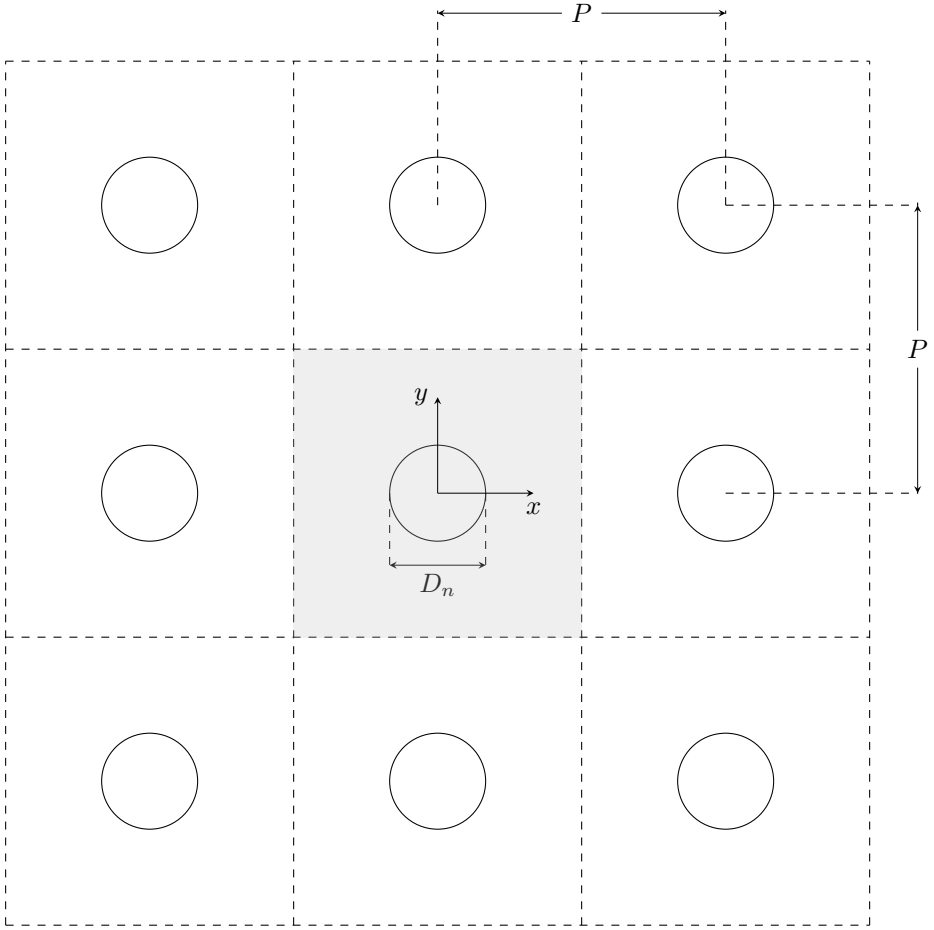

Figure 3.1: Spatial arrangement of jet array, where the shaded region represents the area of interest for the central jet

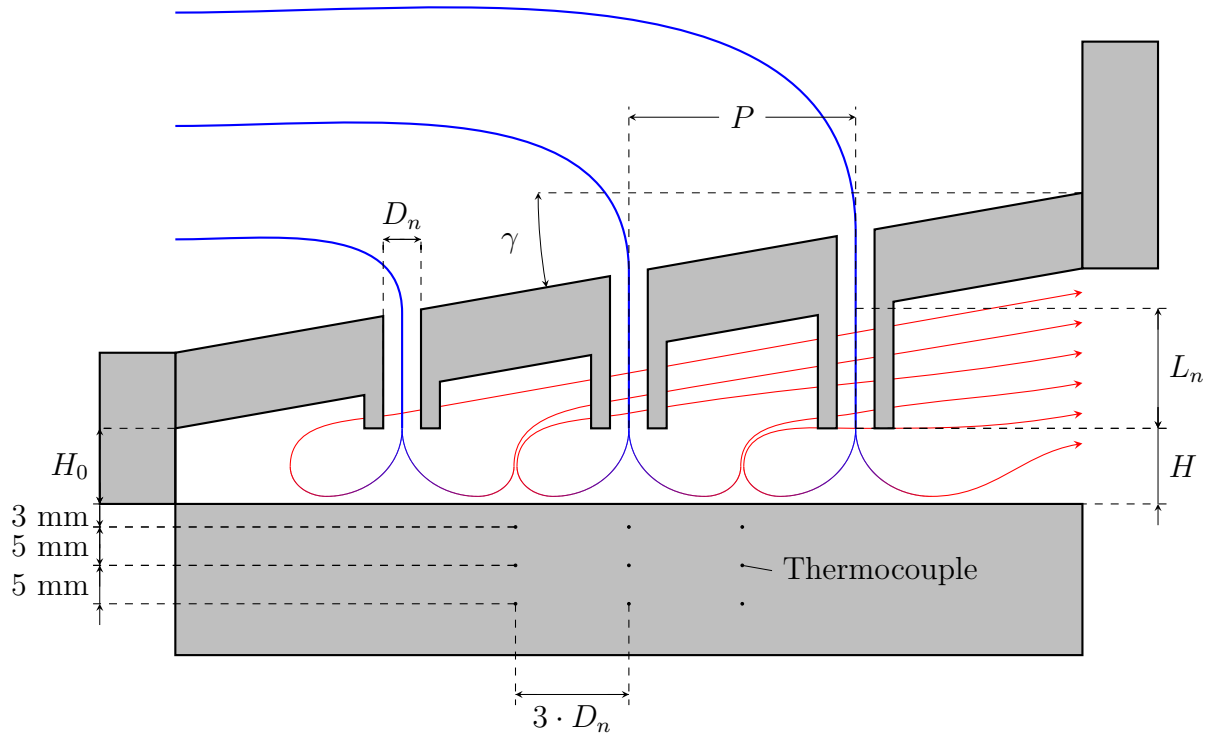

Figure 3.2: Cross-section view of jet array.

that point, even without spent flow management [14]. The expected optimal jet height without spent flow management is in the range of $2 \leq H^* \leq 4$; with effective spent flow management, it is expected that the rate of heat transfer will increase for jet heights lower than two jet diameters. The flow chamber was built to accommodate the additional height of the confining wall at the exit for angles up to 45°.

The flow chamber consisted of an outer, fixed chamber and an inner, movable chamber. The purpose of the inner, movable chamber was to allow the jet array to be translated inline with the direction of flow, the x-direction, and transverse to the direction of flow, the y-direction. The inner chamber was made of five movable walls. The left, right, and top movable walls were attached to the outer chamber with rubber gasket material to prevent fluid from bypassing the inner chamber. The inlet and outlet plenum walls prevented fluid from bypassing the jet plate. Set screws passing through the walls of the outer chamber were used to position the inner walls and to secure the seals that directed the fluid. Set screws

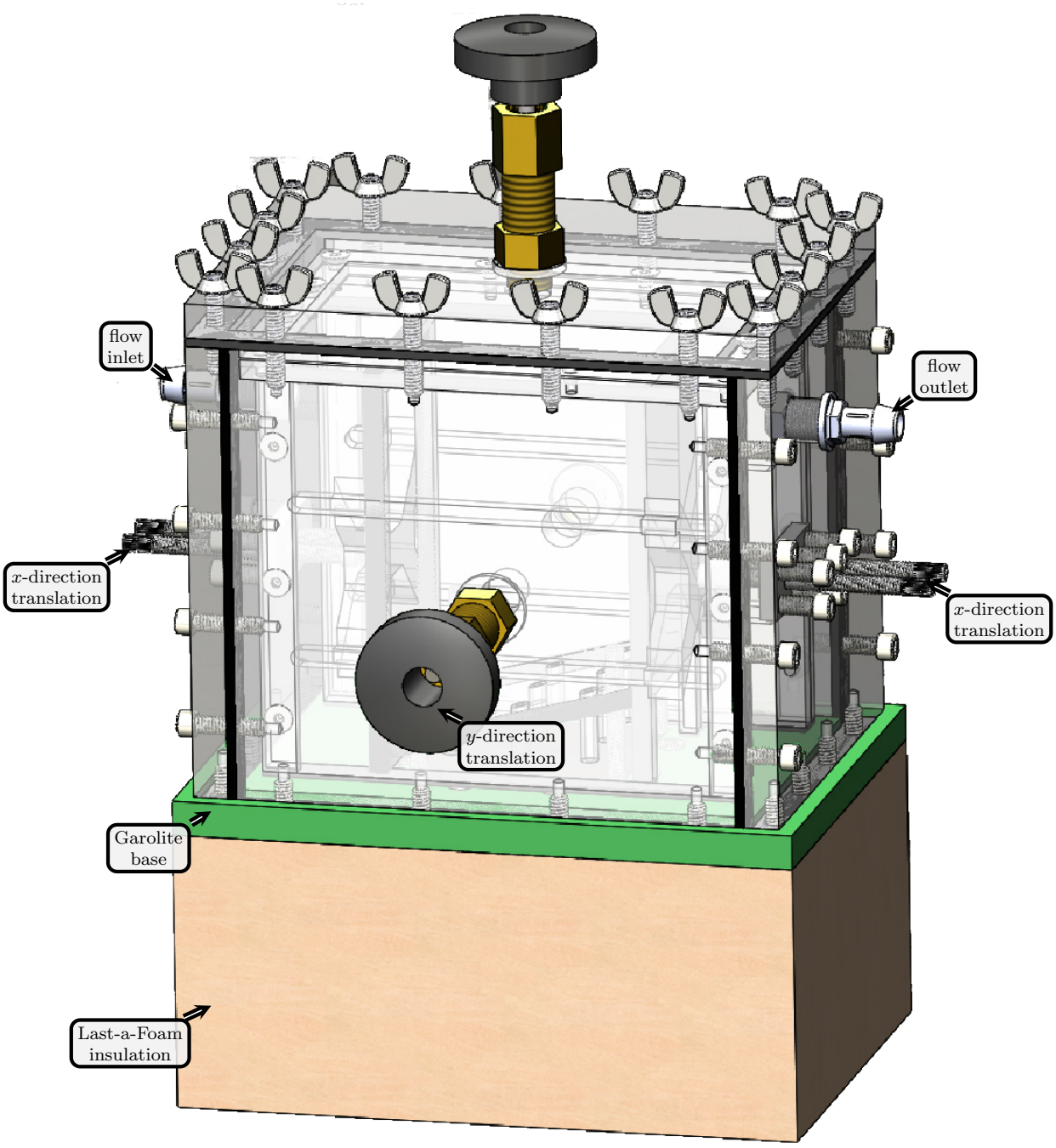

Figure 3.3: External features of jet impingement flow chamber

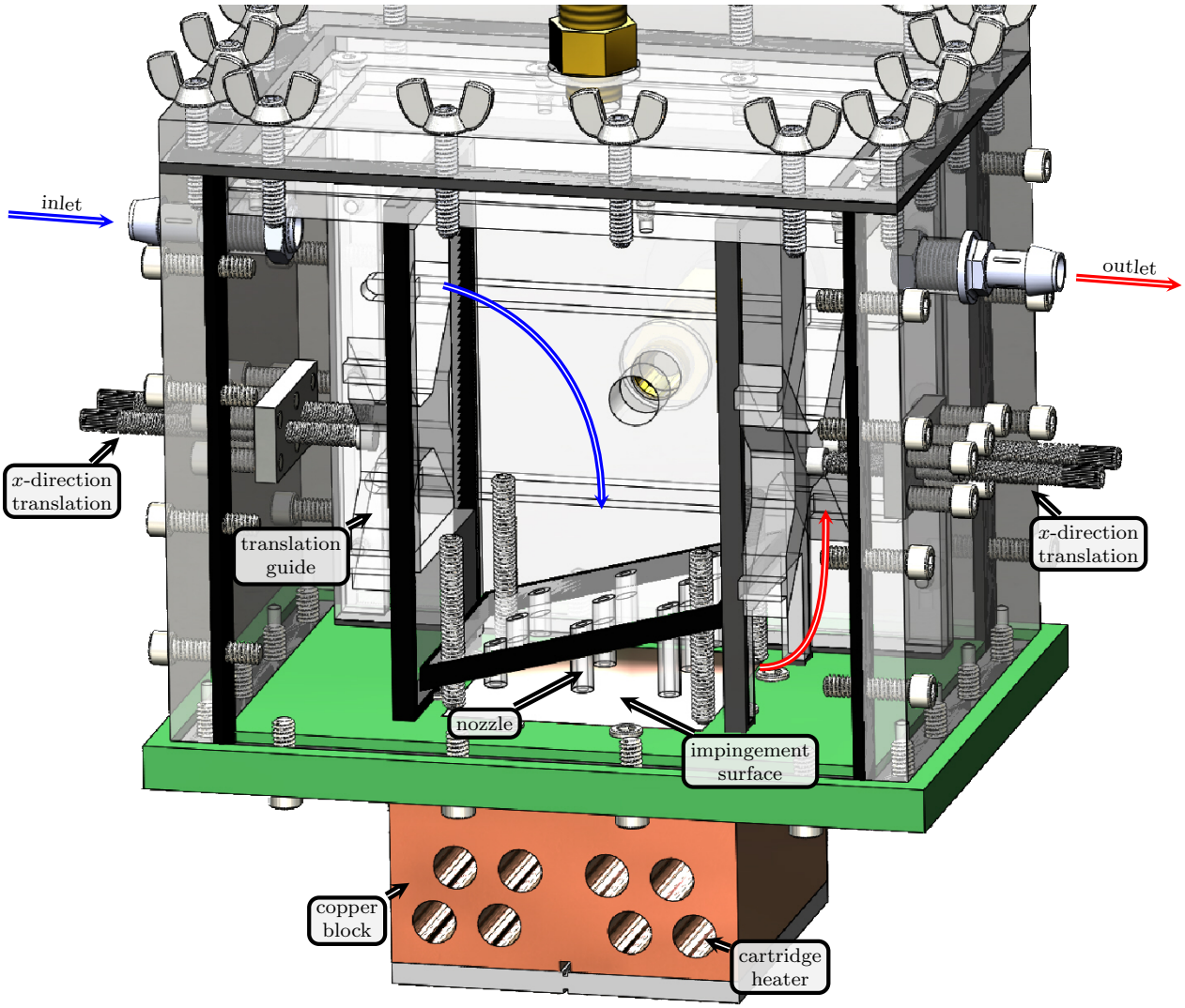

Figure 3.4: Internal features of jet impingement flow chamber

were used to adjust the height of the jet plate. The mechanical drawings used for machining the flow chamber components are available in Appendix A.

3.3 Flow Loop

A schematic of the flow loop used to supply single-phase liquid water to the impingement chamber is shown in Figure 3.5. While the final target application will use WEG, these preliminary tests were conducted using deionized water. The volumetric flow rate of the working fluid was monitored by an Omega FTB4700 turbine flow meter. The flow was driven by an Iwaki magnetic pump with a three phase induction motor that was controlled by a Lenze SMVector variable frequency drive (VFD). The three phase motor and VFD were chosen so that flow rate could be varied programmatically. An Arduino Uno was used to read the signal from the flow meter, which it used as the input to a software proportional-integral-derivative (PID) controller that adjusted the set-point of the VFD to maintain a desired flow rate. The temperatures at the inlet and outlet of the impingement chamber were monitored by k-type thermocouples. The pressure drop across the chamber was monitored by an Omega PX26 differential pressure sensor. A NESLAB RTE-220 chiller was used to supply chilled water to the heat exchanger which was used to maintain a working fluid temperature of approximately 30°C at the inlet of the impingement chamber. The flow rate was nondimensionalized as the average jet Reynolds number based on the nozzle diameter

$$Re_{D_n} = \frac{U_n D_n}{\nu} \tag{3.1}$$

where U_n is the mean inlet nozzle velocity. While the flow through the nozzles is not expected to be uniform with higher flow rates occurring in the downstream nozzles, as predicted by a computational fluid dynamics (CFD) study, the experimental tests were categorized by the average jet Reynolds number based on the total volumetric flow rate.

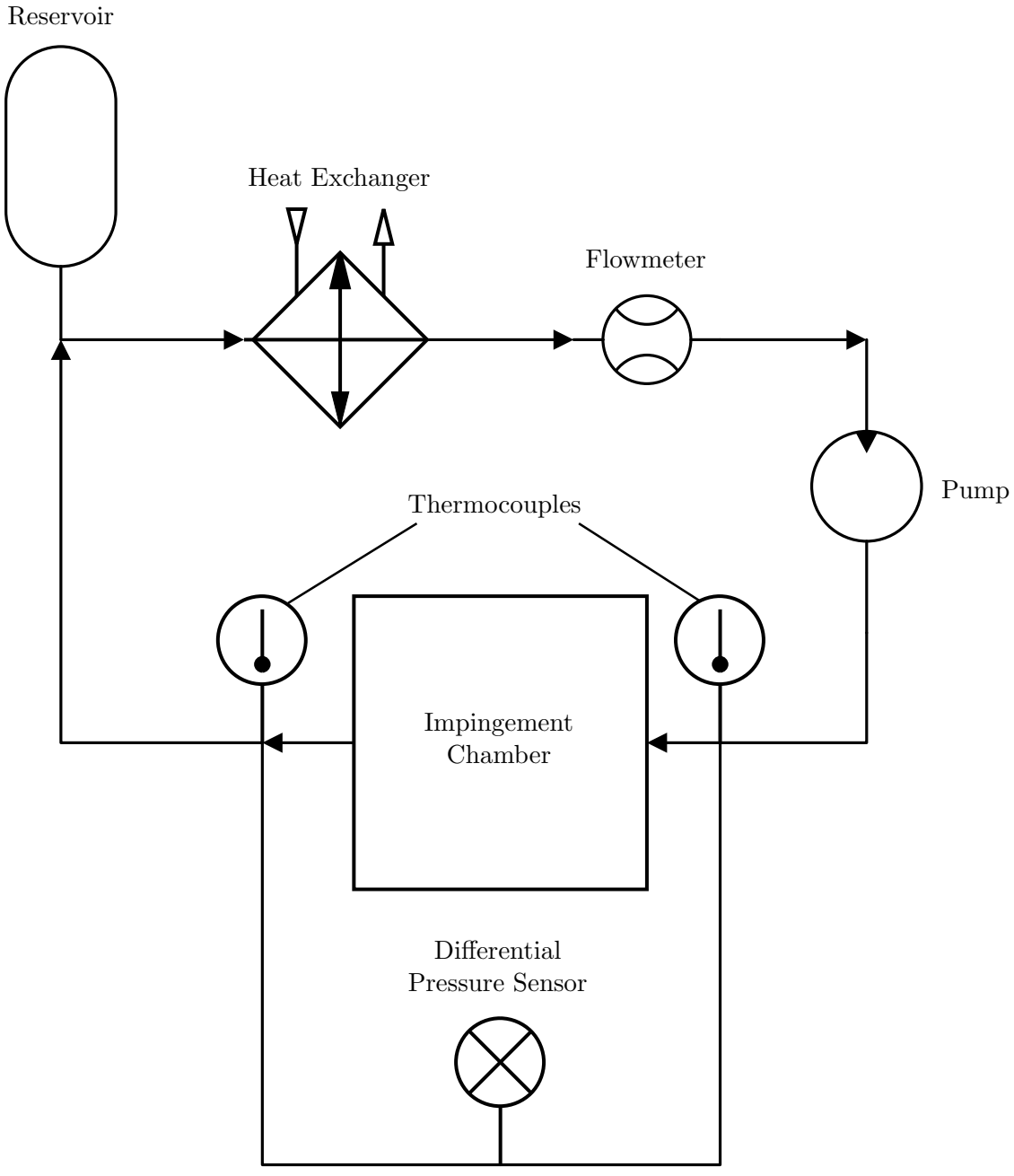

Figure 3.5: Jet impingement flow loop

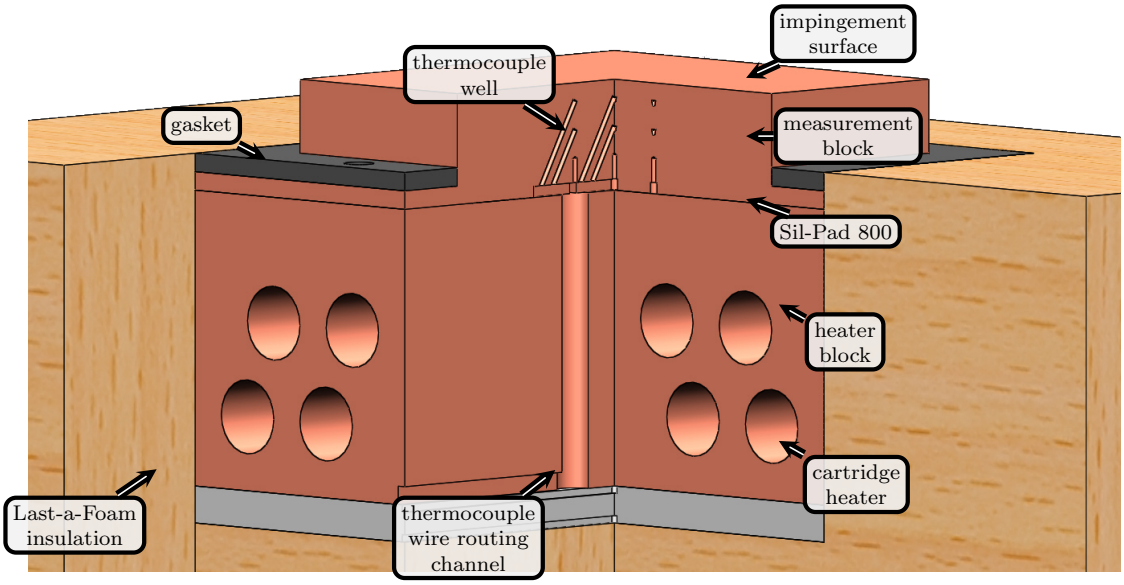

Figure 3.6: Sectioned view of insulation, heater block, TIM, and measurement block

3.4 Heat Generation

The copper impingement surface was heated by eight 1.27 cm × 10.16 cm (1/2" × 4") cylindrical cartridge heaters inserted in a 10.16 cm × 10.16 cm × 7.63 cm (4" × 4" × 3") copper block. The eight cartridge heaters were wired in parallel and were powered by a direct current (DC) power supply. The total power generated by the heaters during testing was limited by the chiller, which was capable of removing 500 W while maintaining a fluid inlet temperature of 30°C. Shown in Figure 3.6, the heater block was connected to a second copper block through a layer of Sil-Pad 800, and foam insulation was used to reduce heat losses.

3.5 Local and Average Surface Thermal Measurements

A copper measurement block was placed between the heater block and the impinging jets. Twelve k-type thermocouples were embedded in the measurement block at known locations, arranged in four groups of three. Each group of three thermocouples was aligned vertically at depths of 3 mm, 8 mm, and 13 mm from the surface, as shown in Figure 3.2. The

thermocouple wires were fed through a channel in the heater block and then coated in silver paste and inserted into 1 mm wells drilled in the measurement block as shown in Figure 3.6. A linear fit was applied to the temperature measurements from each thermocouple group to extrapolate the temperature at the surface, T_{surface}, which was combined with the fluid inlet temperature, $T_{\text{inlet}} \approx 30°\text{C}$, to calculate the temperature rise at the surface,

$$\Theta = T_{\text{surface}} - T_{\text{inlet}}. \tag{3.2}$$

Combining the known thermal conductivity of the copper block with the temperature gradient measured by the thermocouples allowed the copper measurement block to be used as a heat flux meter. This allowed for an estimate of the local heat flux above each thermocouple group to be calculated,

$$\dot{q}'' = -k_c \left.\frac{\partial T}{\partial z}\right|_{z=0}. \tag{3.3}$$

The surface temperature, fluid temperature, and surface heat flux were then used to estimate the local heat transfer coefficient above each thermocouple group,

$$h = \frac{\dot{q}''}{\Theta}. \tag{3.4}$$

Finally, the heat transfer coefficient was used in conjunction with the nozzle diameter and known thermal properties of water at the mean fluid temperature to calculate the local Nusselt number,

$$Nu_{D_n} = \frac{hD_n}{k_w}. \tag{3.5}$$

By using the copper measurement block as a heat flux meter, the uncertainties introduced by parasitic heat losses to the surroundings are minimized.

The apparatus was designed to analyze the central jet in the 3×3 array. Therefore, the four thermocouple groups were located relative to the central jet: one group directly underneath, one group three diameters upstream, one group three diameters downstream,

and one group three diameters transverse to the direction of flow. Only one group was placed in the transverse direction since the flow is assumed to be symmetric about $y = 0$.

By translating the jet array one diameter in the downstream direction, each thermocouple group moves one diameter in the upstream direction relative to the flow. Translating the jet array in both the inline, x^*, and transverse, y^*, directions allowed an experimental 2-D map of local surface measurements to be obtained for each configuration. This technique allowed for an increase in geometric measurement resolution without the need to insert additional thermocouples. A diagram showing the locations of the surface measurements obtained from each thermocouple group by translating in a 3×3 grid is shown in Figure 3.7. Additional details about the translation procedure are available in Appendix B.

The mean heat transfer coefficient and mean Nusselt Number, for each configuration, were obtained by integrating over the area of interest shown in Figure 3.7, half the area of the central jet,

$$\overline{h} = \frac{2}{(P^*)^2} \int_{-\frac{P^*}{2}}^{\frac{P^*}{2}} \int_{0}^{\frac{P^*}{2}} h \, dy^* dx^*. \tag{3.6}$$

Additional details about the data reduction process are available in Appendix C.

The experimental uncertainties for the local and average surface measurements were determined through the method of sequential perturbations to be: ±1.2% for Θ, ±7.7% for $\dot{q}''$, ±8.8% for h, ±2.5% for $\overline{h}$ when $P^* = 4$, and ±2% for $\overline{h}$ when $P^* = 6$. The details of the uncertainty calculations are available in Appendix D.

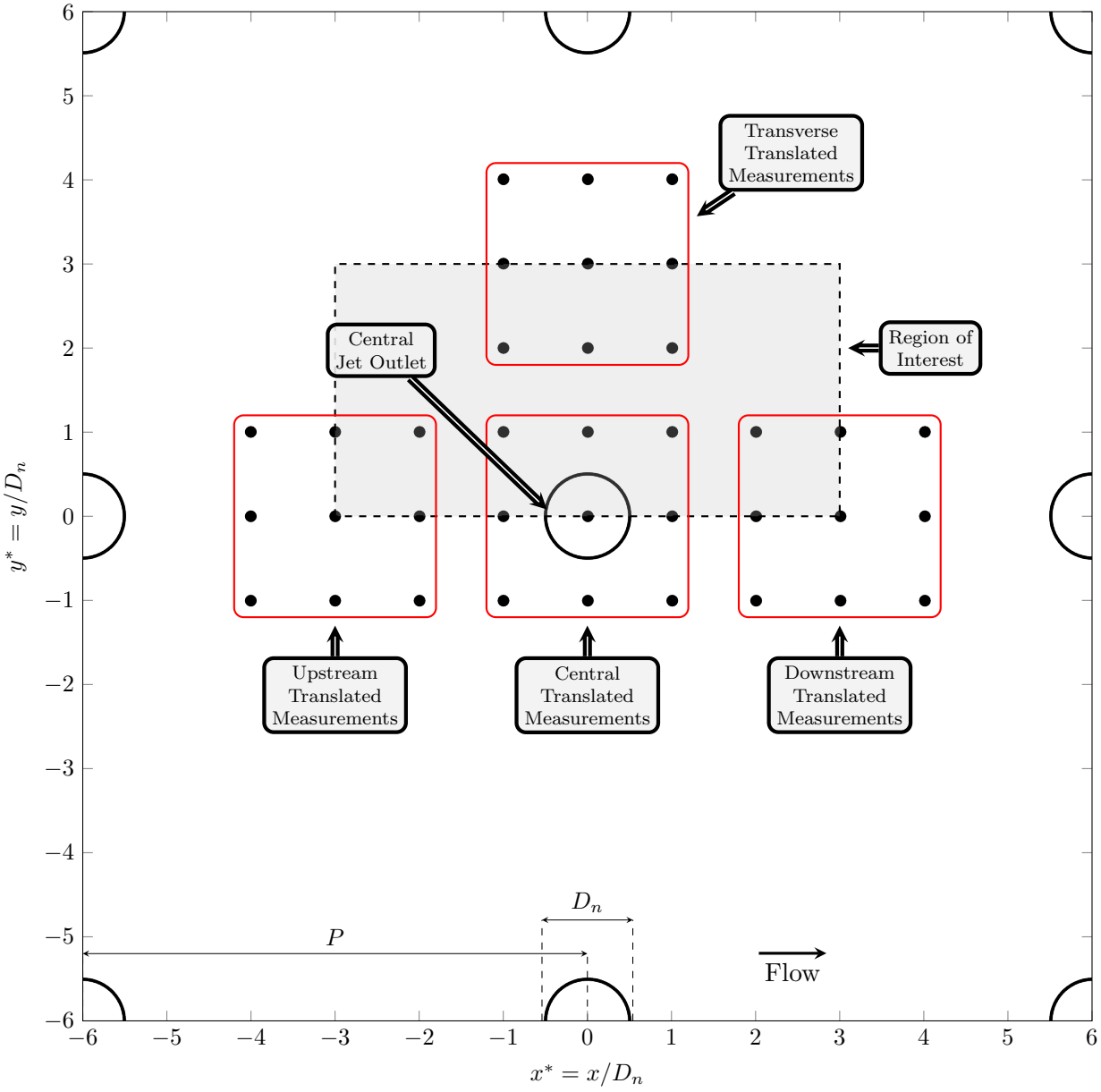

Figure 3.7: Extrapolated surface map layout

Chapter 4

Experimental Results

Testing was conducted to measure the effects of nozzle length, confining wall angle, jet height, jet pitch, and Reynolds number on the thermal performance of an impinging jet array. Three confining wall angles, 0°, 5°, and 10° were tested. Two configurations were tested for the 0° confining wall, an orifice place with $L_n^* = 0$ and a nozzle plate with $L_n^* = 2$. The jet height, H^*, and the initial confining wall height, H_0^*, were equal to each other for all of the 5° and 10° confining wall configurations, which led to a varying nozzle length driven by the angle of the confining wall. For each configuration tested, the jet array was translated to nine locations forming a 3×3 grid of surface measurements around each thermocouple group, resulting in a total of 36 surface measurements.

4.1 Parallel Confining Wall

An example of the variation with Reynolds number of the local thermal measurements inline with the flow, *upstream and downstream* of the central jet, is shown on the left side of Figure 4.1 for a parallel nozzle plate with $\gamma = 0°$, $P^* = 6$, $H^* = 1$, and $L_n^* = 2$ with the error bars signifying the experimental uncertainty. The minimum surface temperature and maximum heat transfer coefficient for each configuration occurring directly under the central jet, $x^* = 0$, is indicative of the high heat transfer in the stagnation region. The surface temperature at each location decreases with increasing Reynolds number, the heat flux at each location is approximately constant with increasing Reynolds number, and the heat transfer coefficient at each location increases with increasing Reynolds number. Since the total heat load was constant for each test, these trends are consistent with the expected trend

of the higher velocity fluid removing the same amount of heat with a smaller temperature rise.

The variation of local thermal measurements *transverse* to the direction of flow is shown on the right side of Figure 4.1. The same trends of local minimum surface temperature and maximum heat transfer coefficient occurring in the stagnation region, as were seen for the inline profiles, are present here as well. Similarly, the surface temperature decreases, the heat flux is approximately constant, and the heat transfer coefficient increases with increasing Reynolds number.

The local thermal measurements for each test were used to create 2-D surface maps of the surface thermal parameters. An example of the surface maps obtained by varying the flow rate while keeping all geometric parameters constant is shown in Figure 4.2, where the outlines of the nozzles are illustrated by black circles and the locations of the local measurements are illustrated by black dots. For each Reynolds number the lowest temperature, highest heat flux, and highest heat transfer coefficient occurred in the region near the nozzle outlet, indicative of the stagnation region. As illustrated in Figure 4.2, increasing the Reynolds number had a significant effect on the magnitudes of the thermal parameters, however it has little effect on the geometric patterns of the local minima and maxima.

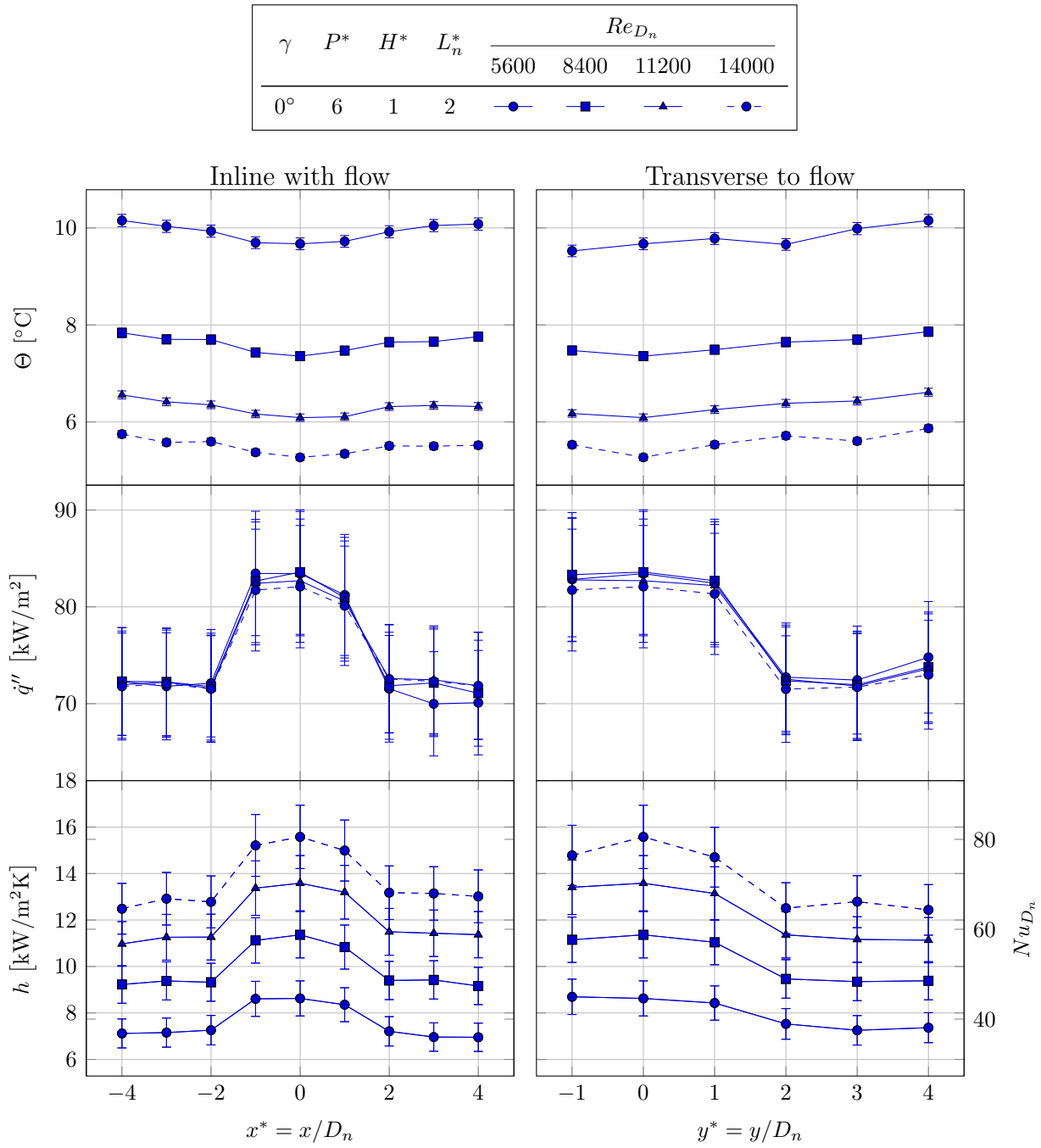

Figure 4.1: Measured local values inline with and transverse to the direction of flow from the central jet.

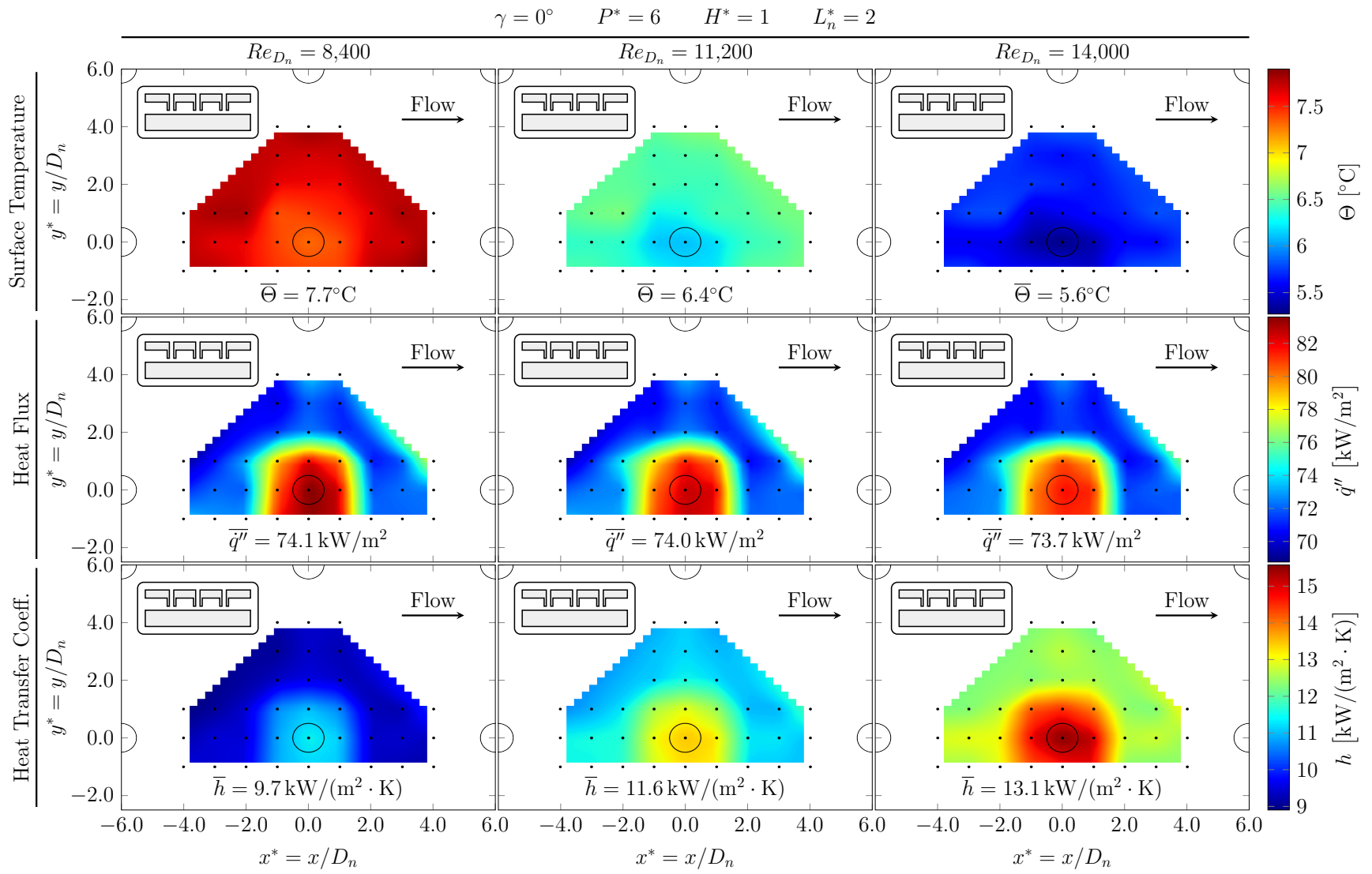

Figure 4.2: Increasing the Reynolds number, with all other parameters being constant, increases the intensity of the local heat transfer at all locations

The variation with Reynolds number of the average heat transfer coefficient and average Nusselt number (shown on the right axis) for the orifice plates and nozzle plates with a pitch of six jet diameters is shown in Figure 4.3. The general trend of increasing heat transfer with increasing Reynolds number occurred for each geometric configuration.

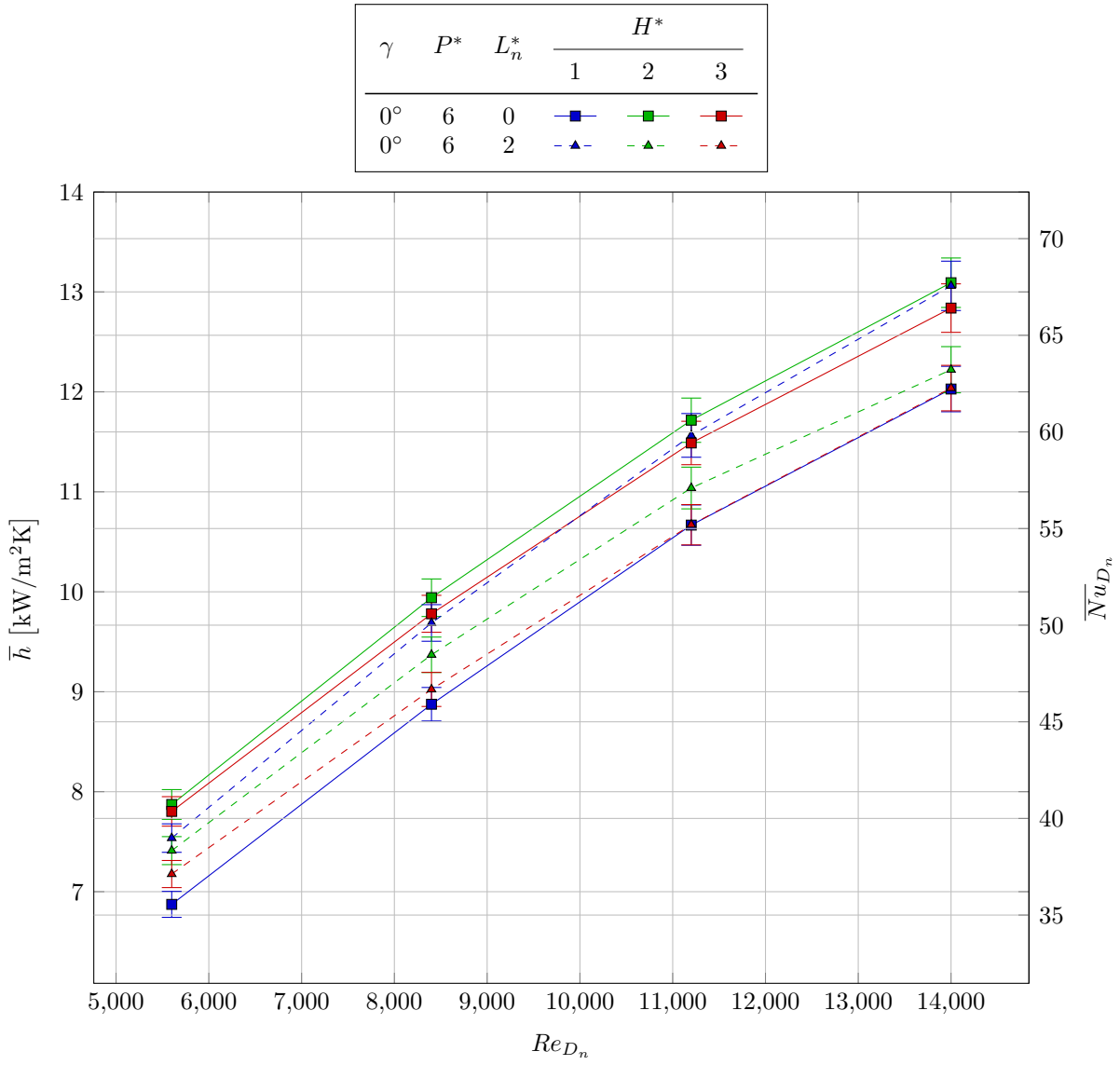

Figure 4.3: Variation in average heat transfer for orifice and nozzle plates with parallel confining walls at $P^* = 6$

The variation of the surface average heat transfer with Reynolds number for the best case orifice plate, $H^* = 2$ and $L_n^* = 0$, and the best case nozzle plate, $H^* = 1$ and $L_n^* = 2$, is shown in Figure 4.4. While these two geometries had the same average heat transfer at

the highest Reynolds number, their local heat transfer values were significantly different, as shown in Figure 4.5. In comparison to the orifice plate, the nozzle plate had higher heat transfer in the stagnation region and lower heat transfer in the wall jet region. The higher heat transfer in the stagnation region for the nozzle plate suggests that the nozzles provide enough room for the spent fluid to prevent it from interfering with the incoming jet. While at the same time, the lower heat transfer in the wall jet region for the nozzle plate suggests that the spent fluid is not being kept close enough to the surface to enhance the wall jet heat transfer. The ability to measure local heat transfer parameters enables this detailed analysis.

4.2 Angled Confining Wall

The competing effects of nozzle length on the heat transfer in the stagnation region and the wall jet region provide an opportunity for optimization. The optimum nozzle length would allow for the enhancement in the stagnation region of a smaller jet height, while still keeping the spent fluid close enough to the surface to enhance the heat transfer in the wall jet region. This optimum length nozzle is expected to be driven by the ratio of the incoming jet momentum to the spent fluid momentum. However, each row of nozzles injects more fluid into the spent flow, which would cause an increase in the momentum of the spent fluid for a constant channel height. In order to maintain a more consistent momentum for the spent fluid with downstream position, an angled confining wall was used to accommodate the increasing volumetric flow rate of the spent flow.

An example of the surface maps obtained by varying the confining wall angle, while holding all other parameters constant, is shown in Figure 4.6. Increasing the confining wall angle gives room for the spent fluid to be diverted around downstream jets, which increases both the heat flux and heat transfer coefficient in the stagnation region. However, it also decreases the spent fluid velocity, which decreases both the heat flux and heat transfer coefficient in the wall jet region. The combination of these effects causes the intermediate

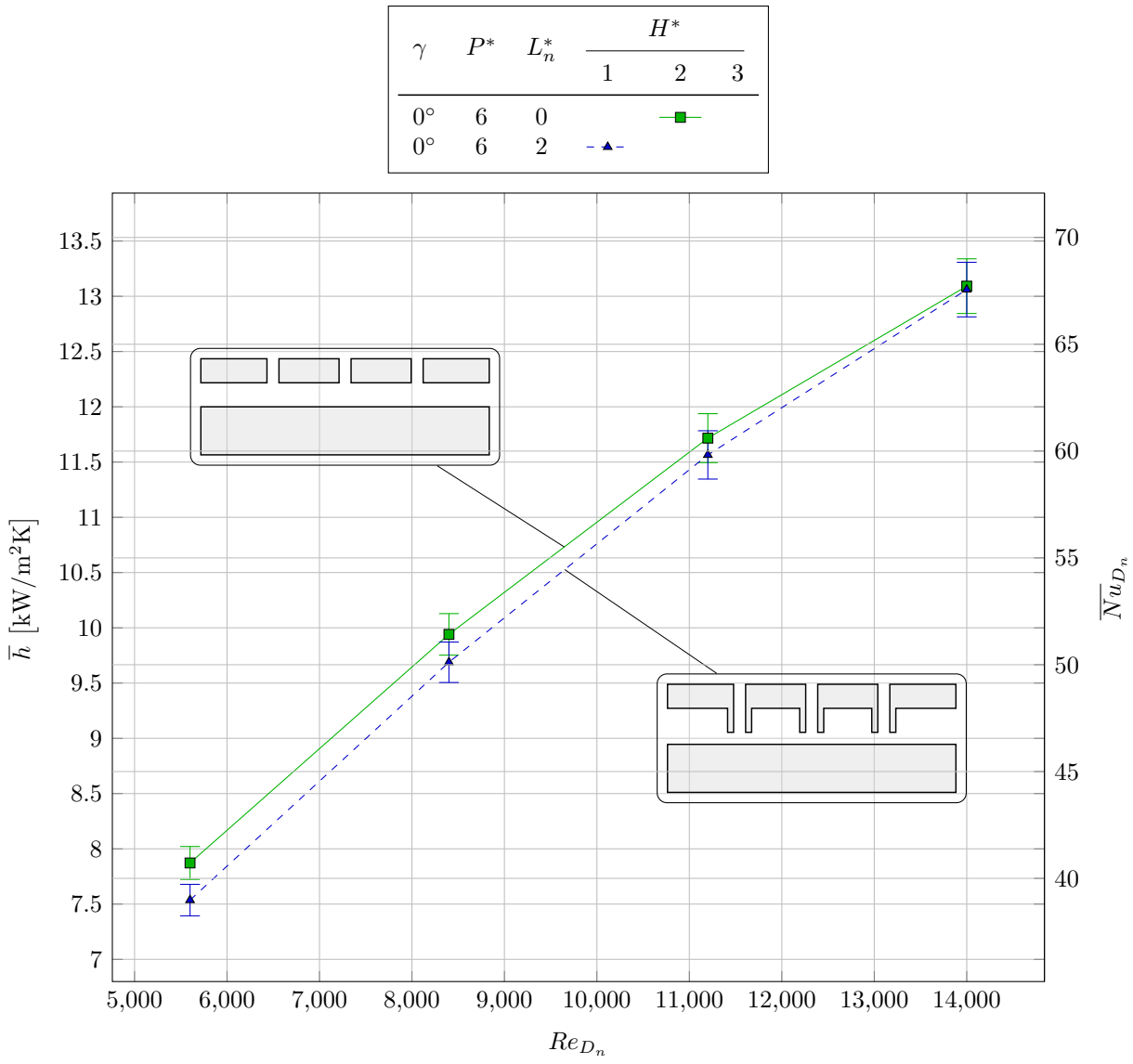

Figure 4.4: Comparison of best case average heat transfer for orifice and nozzle plates with parallel confining walls at $P^* = 6$

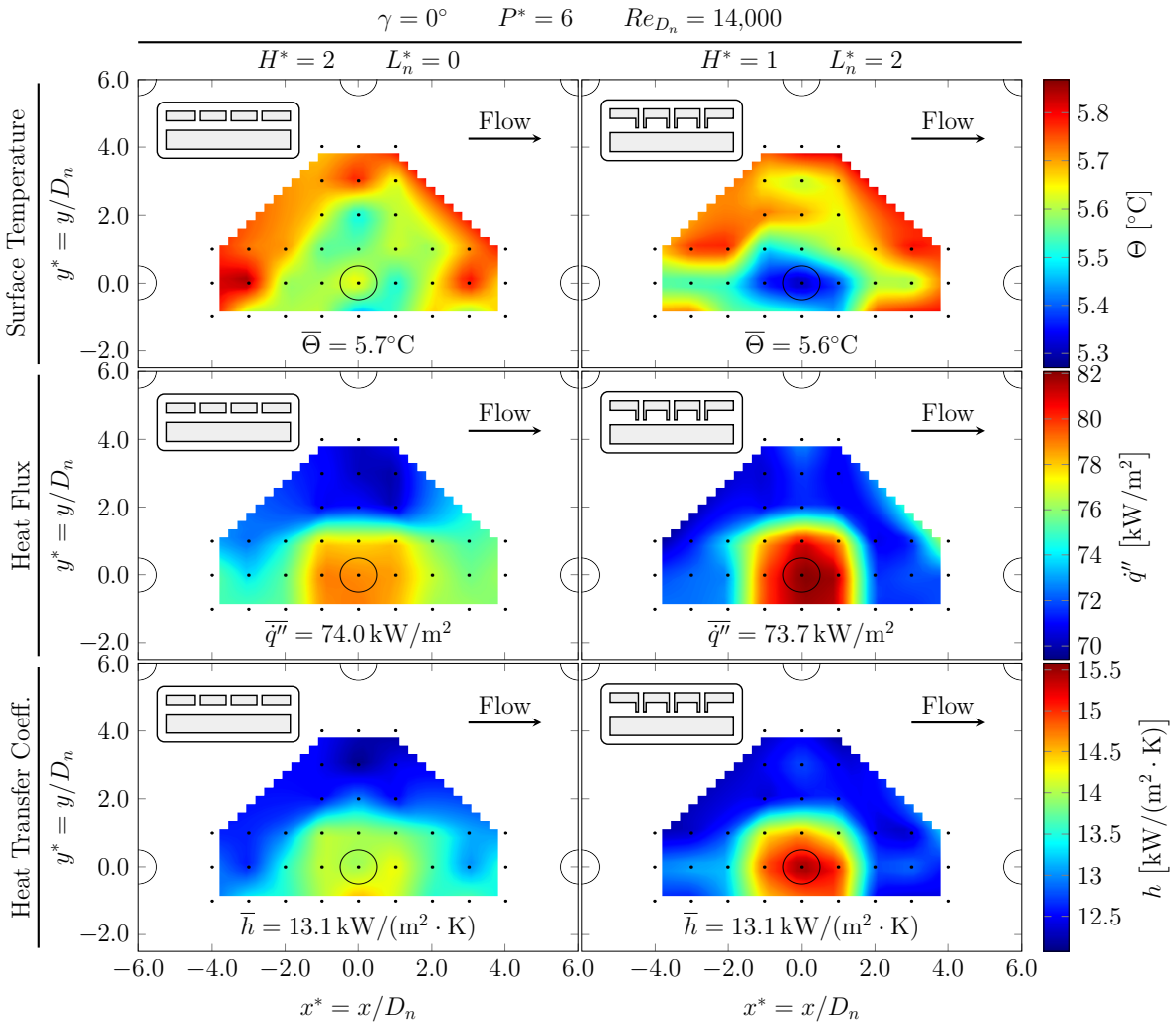

Figure 4.5: Comparison of best case local heat transfer for orifice and nozzle plates with parallel confining walls at $P^* = 6$, and $Re_{D_n} = 14,000$

confining wall angle of 5° to have a better thermal performance than either the 0° or the 10° confining walls.

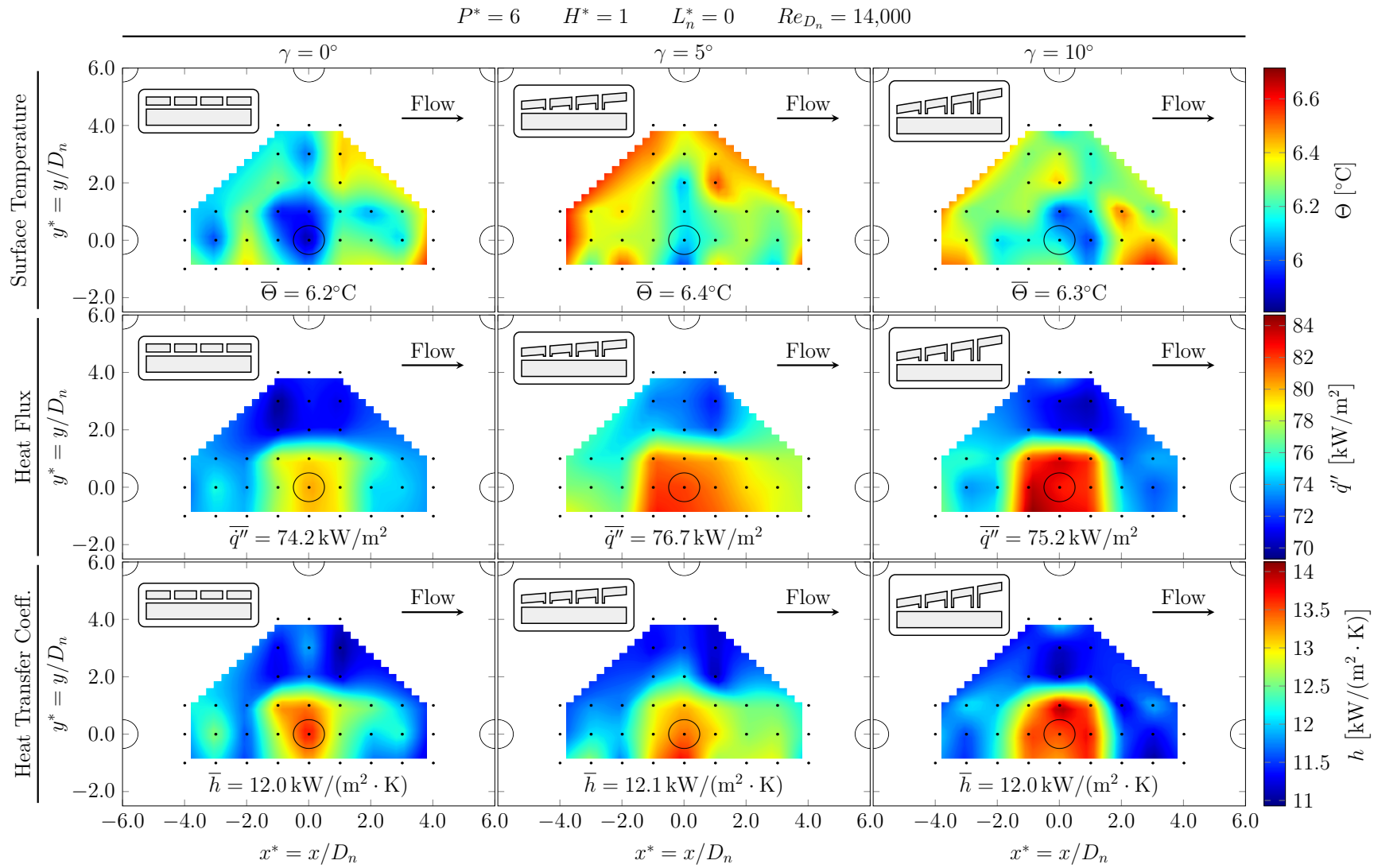

Figure 4.6: Increasing the confining wall angle, with all other parameters being constant, enhances the stagnation region heat transfer and degrades the wall jet region heat transfer

The variation with Reynolds number of the average heat transfer coefficient and average Nusselt number for the orifice plates, with $\gamma = 0°$, is shown in Figure 4.7. For each Reynolds number, the highest performance occurred at the intermediate jet height, $H^* = 2$. The highest measured heat transfer for the orifice plates was an average heat transfer coefficient of $\overline{h} = 13,100\,\mathrm{W/m^2K} \pm 2\%$ at an average jet Reynolds number of 14,000 with a Nusselt number of $\overline{Nu}_{D_n} = 67.7$.

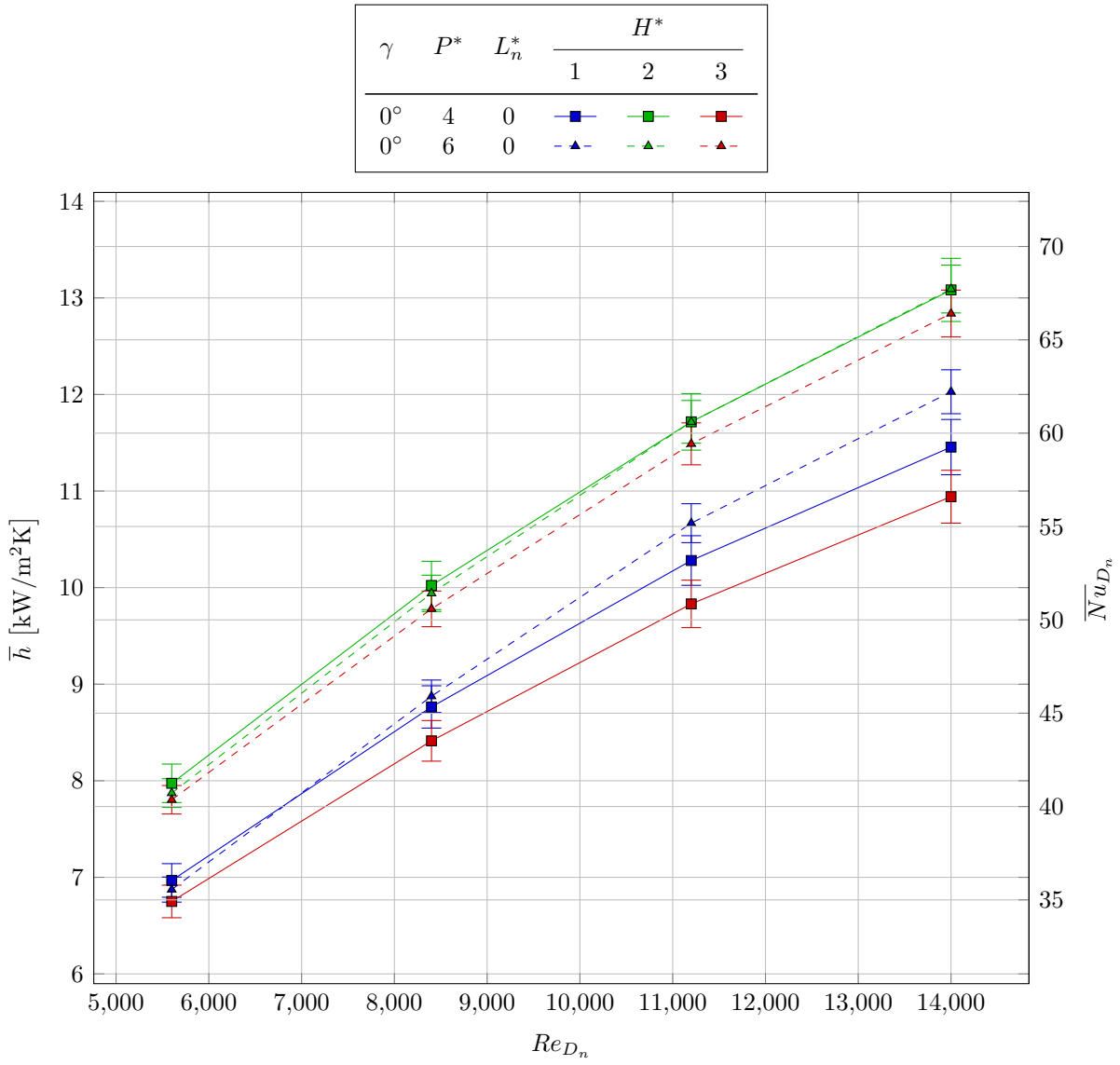

Figure 4.7: Variation in heat transfer with Reynolds number for orifice plates, $\gamma = 0°$ and $L_n^* = 0$

The variation with Reynolds number of the average heat transfer coefficient and average Nusselt number for the angled confining wall, with $\gamma = 5°$, is shown in Figure 4.8. For each Reynolds number, the highest performance occurred at the lowest jet height, $H^* = 1$, and the lowest pitch, $P^* = 4$. This suggests that the 5° confining wall provides enough relief to prevent the spent fluid from interfering with the incoming fluid prior to reaching the stagnation region. The highest measured heat transfer for the angled confining walls was an average heat transfer coefficient of $\overline{h} = 13,100\,\mathrm{W/m^2K} \pm 2.5\%$ at an average jet Reynolds number of 14,000 with an average Nusselt number of $\overline{Nu}_{D_n} = 67.5$.

The lowest jet height for the 5° confining wall was the only geometric configuration that showed an increase in heat transfer with decreasing pitch. Decreasing the pitch has multiple competing effects on the overall heat transfer. A decrease in pitch increases the number of stagnation regions with high local heat transfers. It also reduces the evacuation space available for the spent fluid, which increases the detrimental effect of the spent fluid interference on the incoming fluid. The average heat transfer increased for the 5° confining wall only for the lowest jet height, and the effect was strongest at the smallest pitch. These results suggest that the 5° angle provides enough relief for the spent flow to avoid the incoming fluid for the lowest jet height, but not for the larger jet heights.

The variation in heat transfer with jet height is shown in Figure 4.9. The 5° confining wall continues to exhibit an increase in heat transfer with decreasing jet height for the lowest height tested, while all other configurations appear to have optimum heights that are greater than one jet diameter. This suggests that it may be possible to improve the heat transfer of the angled wall even more by further decreasing the jet height and pitch.

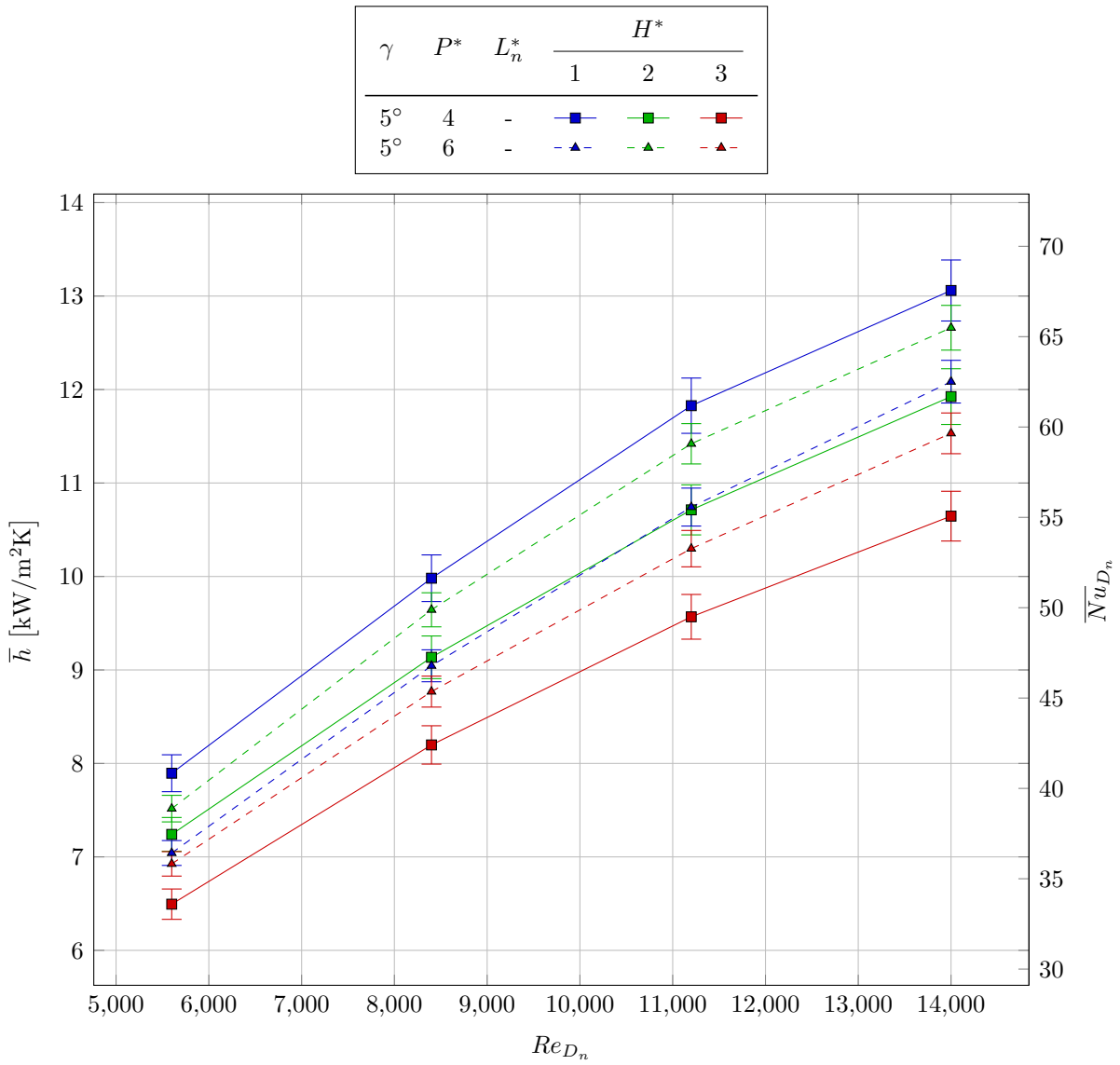

Figure 4.8: Variation in heat transfer with Reynolds number for angled confining wall, $\gamma = 5°$

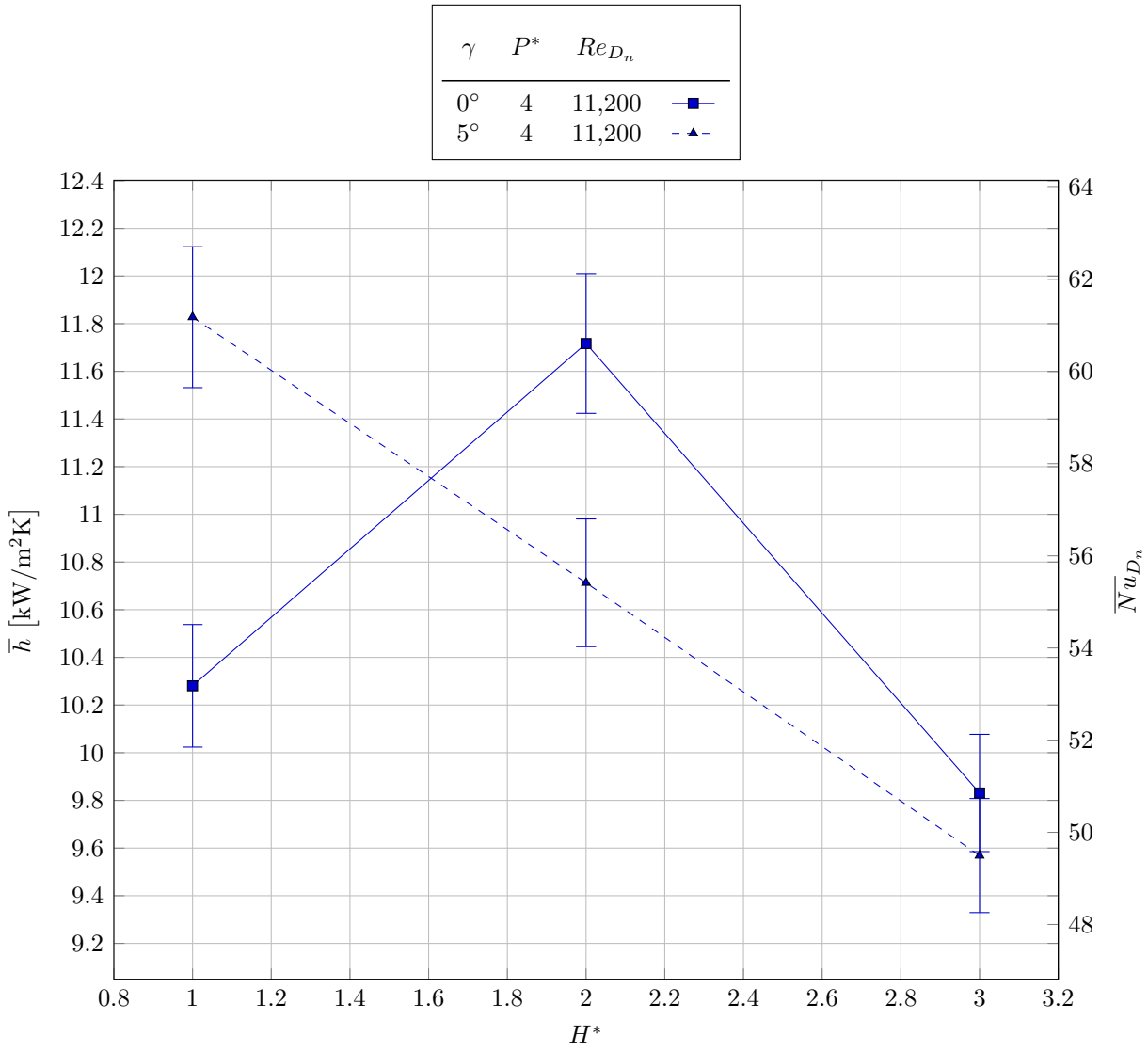

Figure 4.9: Variation in heat transfer with jet height

Chapter 5

Modeling

A model was developed to analyze the thermal performance of the jet impingement systems used in the experiment. The modeling was done using ANSYS® Fluent, Academic Research, Release 14.5.7. The SST and v^2f turbulence models were used during the analysis.

5.1 Workflow

5.1.1 Geometry

In order to reduce the computational load, the geometry was reduced to a half symmetry of a single row of three nozzles, as shown in Figure 5.1, after ensuring that the symmetry condition produced that same results as a full nozzle row with periodic boundary conditions. Initially a model was developed that extended only up to the nozzle inlet, and a uniform velocity was applied to each nozzle. However, it was found that this approach led to an offset velocity profile within the nozzles for the angled confining wall cases. In order to avoid this issue, a plenum was included above the inlet to the nozzles to allow the velocity profile in the nozzles to be resolved. This had the added benefit of more accurately capturing the flow distribution between the nozzles, rather than forcing an equal flow rate through each nozzle. A copper block was included below the fluid to account for conductive heat spreading within the solid, rather than forcing a uniform heat flux at the surface.

The geometry was drawn in the ANSYS® DesignModeler application through the use of the scripting application program interface (API). The DesignModeler scripting API allows the execution of extensions written in JScript, the Microsoft dialect of JavaScript. Using the scripting API decreases the effort required to reproduce multiple geometries for use in a parametric study.

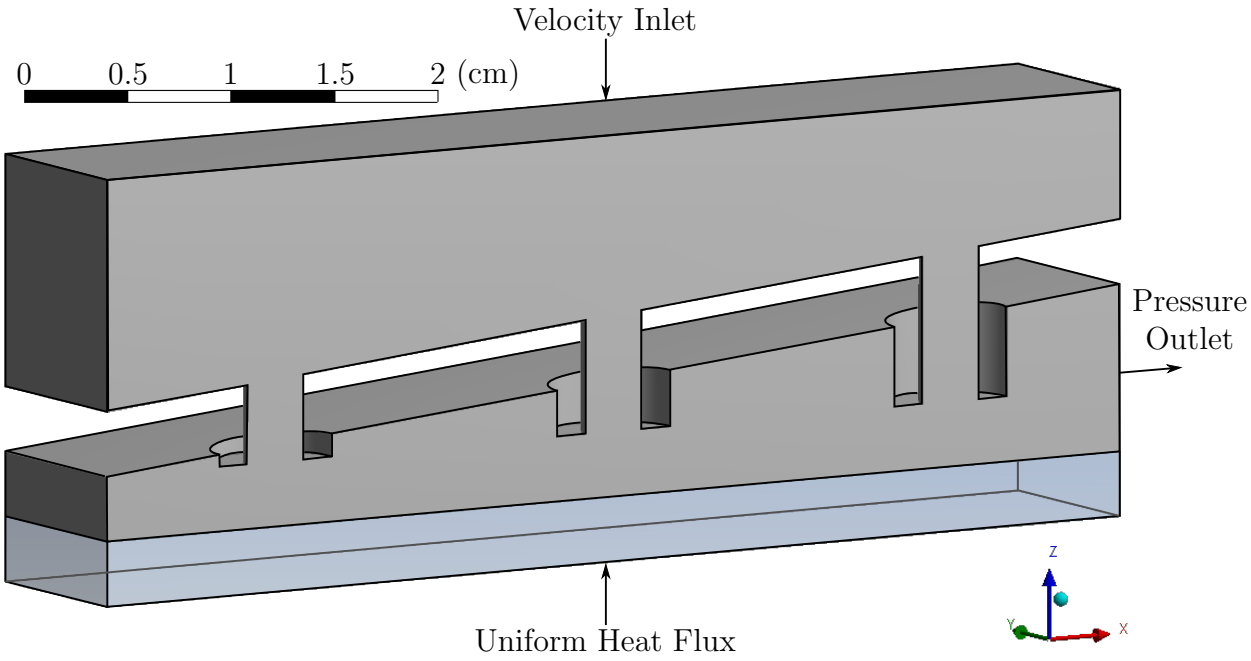

Figure 5.1: Half-symmetry geometry of a single row of nozzles used for modeling

Each geometry was placed into a separate project and managed by ANSYS® Workbench. Similar to the scripting API of DesignModeler, Workbench has a scripting API that allows the execution of Python code. Each project in the study was created using a Python Workbench script to initialize the DesignModeler module and pass the JScript code to DesignModeler to create the desired geometry.

5.1.2 Mesh

Each geometry was meshed using ANSYS® Workbench. The fluid and the copper block were meshed independently, with comparable length scales at the interface where the bodies come into contact. Both bodies were meshed using tetrahedral elements. Prismatic boundary layer cells, or inflation controls, were used to refine the mesh in the regions near the walls to resolve the physics in the boundary layers without having to use an extremely fine mesh throughout the entire volume. Each surface was selected and named through the meshing graphical user interface (GUI). After meshing, each model was exported in a format suitable for importing into ANSYS® Fluent.

The turbulence models that are recommended for jet impingement problems, SST and v^2f, require a fine mesh in the stagnation and wall jet regions. The near wall grid should be fine enough that the dimensionless wall distance of the first grid point is less than one,

$$y^+ = \frac{u_\tau y}{\nu} < 1, \tag{5.1}$$

where y is the distance to the nearest wall[1], ν is the kinematic viscosity, and u_τ is the shear velocity,

$$u_\tau = \sqrt{\frac{\tau}{\rho}}. \tag{5.2}$$

Because the value of y^+ is dependent on the cell Reynolds number, it is difficult to predict the necessary grid spacing to maintain $y^+ < 1$ for complex flows. A pragmatic approach to this problem is to include a check for $y^+ < 1$ during the successive grid refinement of a conventional grid independence analysis.

5.1.3 Fluent

ANSYS® Fluent was used to apply boundary conditions, set material properties, initialize the pressure and flow fields, select the turbulence model, and solve the resulting equations for the grid. Symmetry boundary conditions were applied to the outside surfaces normal to the y-axis, a uniform velocity inlet boundary condition was applied to the top surface of the plenum, a pressure outlet boundary condition was applied to the surface at the exit of the impingement region, a uniform heat flux boundary condition was applied to the bottom of the copper block, no-slip conjugate heat transfer condition was applied at the interface between the fluid and the copper block, and all other surfaces were treated as adiabatic walls.

Fluent can be incorporated into a project and launched through ANSYS® Workbench, launched as a standalone graphical application, or run as a batch job without a graphical

[1]In this context, y and y^+ are traditionally used to refer to the distance to the nearest wall. Therefore, y^+ does not necessarily have to be in the same direction as the y-axis of the coordinate system.

interface. Initial debugging was done through the graphical interface; however, the bulk of the computation for this study was done on the Samuel Ginn College of Engineering Virtual Symmetric Multiprocessing High Performance Computing Cluster (vSMP HPCC) which has no graphical interface and requires that Fluent be run in batch mode.

5.2 Turbulence Models

5.2.1 SST *k-ω*

The SST k-ω model is a hybrid turbulence model that uses the k-ω model near the wall and the k-ε model in the far field [96]. The ANSYS® Fluent implementation of the SST k-ω model is documented in the ANSYS® Academic Research, Release 15.0, Help System, Fluent Theory Guide [97] and summarized below.

Transport Equations

The transport equations for k and ω are:

$$\frac{\partial(\rho k)}{\partial t} + \frac{\partial(\rho k u_i)}{\partial x_i} = \frac{\partial}{\partial x_i}\left(\Gamma_k \frac{\partial k}{\partial x_j}\right) + \tilde{G}_k - Y_k + S_k, \tag{5.3}$$

$$\frac{\partial(\rho \omega)}{\partial t} + \frac{\partial(\rho \omega u_j)}{\partial x_j} = \frac{\partial}{\partial x_j}\left(\Gamma_\omega \frac{\partial \omega}{\partial x_j}\right) + G_\omega - Y_\omega + S_\omega, \tag{5.4}$$

where S_k and S_ω are user-defined source terms.

Effective Diffusivity

The effective diffusivities for k and ω are given by:

$$\Gamma_k = \mu + \frac{\mu_t}{\sigma_k}, \tag{5.5}$$

$$\Gamma_\omega = \mu + \frac{\mu_t}{\sigma_\omega}, \tag{5.6}$$

$$\mu_t = \frac{\rho k}{\omega} \frac{1}{\max\left(\frac{1}{\alpha^*}, \frac{SF_2}{a_1 \omega}\right)}, \tag{5.7}$$

where S is the strain rate magnitude,

$$\alpha^* = \alpha^*_\infty \left(\frac{\alpha^*_0 + Re_t/R_k}{1 + Re_t/R_k} \right), \tag{5.8}$$

$$Re_t = \frac{\rho k}{\mu \omega}, \tag{5.9}$$

$$\alpha^*_0 = \frac{\beta_i}{3}, \tag{5.10}$$

$$\beta_i = F_1 \beta_{i,1} + (1 - F_1)\beta_{i,2}, \tag{5.11}$$

$$\sigma_k = \left(\frac{F_1}{\sigma_{k,1}} + \frac{1 - F_1}{\sigma_{k,2}} \right)^{-1}, \tag{5.12}$$

$$\sigma_\omega = \left(\frac{F_1}{\sigma_{\omega,1}} + \frac{1 - F_1}{\sigma_{\omega,2}} \right)^{-1}, \tag{5.13}$$

$$F_1 = \tanh\left(\phi_1^4\right), \tag{5.14}$$

$$\phi_1 = \min\left[\max\left(\frac{\sqrt{k}}{0.09\omega y}, \frac{500\mu}{\rho y^2 \omega} \right), \frac{4\rho k}{\sigma_{\omega,2} D^+_\omega y^2} \right], \tag{5.15}$$

$$D^+_\omega = \max\left(2\rho \frac{1}{\sigma_{\omega,2}} \frac{1}{\omega} \frac{\partial k}{\partial x_j} \frac{\partial \omega}{\partial x_j}, 10^{-10} \right), \tag{5.16}$$

$$F_2 = \tanh\left(\phi_2^2\right), \tag{5.17}$$

$$\phi_2 = \max\left[2\frac{\sqrt{k}}{0.09\omega y^2}, \frac{500\mu}{\rho y^2 \omega} \right], \tag{5.18}$$

where y is the distance to the nearest wall.

Turbulence Production

The generation of k, $\tilde{G}_k$, and the generation of ω, G_ω, are given by:

$$\tilde{G}_k = \min\left(G_k, 10\rho\beta^* k\omega\right), \tag{5.19}$$

$$G_k = \mu_t S^2, \tag{5.20}$$

$$\beta^* = \beta^*_\infty \left(\frac{4/15 + (Re_t/R_\beta)^4}{1 + (Re_t/R_\beta)^4}\right), \tag{5.21}$$

$$G_\omega = \frac{\alpha}{\nu_t}\tilde{G}_k, \tag{5.22}$$

$$\alpha = \frac{\alpha_\infty}{\alpha^*}\left(\frac{\alpha_0 + Re_t/Re_\omega}{1 + Re_t/Re_\omega}\right), \tag{5.23}$$

$$\alpha_\infty = F_1\alpha_{\infty,1} + (1 - F_1)\,\alpha_{\infty,2}, \tag{5.24}$$

$$\alpha_{\infty,1} = \frac{\beta_{i,1}}{\beta^*_\infty} - \frac{\kappa^2}{\sigma_{\omega,1}\sqrt{\beta^*_\infty}}, \tag{5.25}$$

$$\alpha_{\infty,2} = \frac{\beta_{i,2}}{\beta^*_\infty} - \frac{\kappa^2}{\sigma_{\omega,2}\sqrt{\beta^*_\infty}}. \tag{5.26}$$

Turbulence Dissipation

The dissipation of k, Y_k, and the dissipation of ω, Y_ω, are given by:

$$Y_k = \rho\beta^* k\omega, \tag{5.27}$$

$$Y_\omega = \tau\beta\omega^2. \tag{5.28}$$

Cross-Diffusion Modification

The blending of the k-ε and k-ω models results in a cross-diffusion term defined as:

$$D_\omega = 2(1 - F_1)\rho\frac{1}{\omega\sigma_{\omega,2}}\frac{\partial k}{\partial x_j}\frac{\partial \omega}{\partial x_j}. \tag{5.29}$$

Constants

The constants used in the SST k-ω model are:

$$\alpha^*_\infty = 1, \tag{5.30}$$

$$\alpha_1 = 0.31, \tag{5.31}$$

$$\beta^*_\infty = 0.09, \tag{5.32}$$

$$\beta_{i,1} = 0.072, \tag{5.33}$$

$$\beta_{i,2} = 0.0828, \tag{5.34}$$

$$\kappa = 0.41, \tag{5.35}$$

$$R_k = 6, \tag{5.36}$$

$$R_\beta = 8, \tag{5.37}$$

$$R_\omega = 2.95, \tag{5.38}$$

$$\sigma_{k,1} = 1.176, \tag{5.39}$$

$$\sigma_{\omega,1} = 2.0, \tag{5.40}$$

$$\sigma_{k,2} = 1.0, \tag{5.41}$$

$$\sigma_{\omega,2} = 1.168\ . \tag{5.42}$$

5.2.2 Transition SST

The transition SST model in ANSYS® Fluent extends the traditional SST k-ω transport equations by tracking two additional variables for intermittency and transition onset using empirical correlations developed by Menter et al. [98]. The ANSYS® Fluent implementation of Menter's transition SST is documented in the ANSYS® Academic Research, Release 15.0, Help System, Fluent Theory Guide [97] and summarized below.

Transport Equations

The transport equations for the intermittency, γ, and the transition momentum thickness Reynolds number, $\tilde{Re}_{\theta t}$, are defined as:

$$\frac{\partial\left(\rho\gamma\right)}{\partial t}+\frac{\partial\left(\rho U_j\gamma\right)}{\partial x_j}=P_{\gamma 1}-E_{\gamma 1}+P_{\gamma 2}-E_{\gamma 2}+\frac{\partial}{\partial x_j}\left[\left(\mu+\frac{\mu_t}{\sigma_\gamma}\right)\frac{\partial\gamma}{\partial x_j}\right], \tag{5.43}$$

$$\frac{\partial\left(\rho\tilde{Re}_{\theta t}\right)}{\partial t}+\frac{\partial\left(\rho U_j\tilde{Re}_{\Theta t}\right)}{\partial x_j}=P_{\Theta t}+\frac{\partial}{\partial x_j}\left[\sigma_{\theta t}(\mu+\mu_t)\frac{\partial\tilde{Re}_{\theta t}}{\partial x_j}\right]. \tag{5.44}$$

The transition model is combined with the SST model by modifying the k transport equation:

$$\frac{\partial\left(\rho k\right)}{\partial t}+\frac{\partial\left(\rho k u_i\right)}{\partial x_i}=\frac{\partial}{\partial x_j}\left(\Gamma_k\frac{\partial k}{\partial x_j}\right)+G_k^*-Y_k^*+S_k, \tag{5.45}$$

where S_k is a user defined source term.

Source Terms

The transition and destruction/laminarization source terms are given by:

$$P_{\gamma 1}=C_{a1}F_{\text{length}}\rho S\left[\gamma F_{\text{onset}}\right]^{C_{\gamma 3}}, \tag{5.46}$$

$$E_{\gamma 1}=C_{e1}P_{\gamma 1}\gamma, \tag{5.47}$$

$$P_{\gamma 2}=C_{a2}\rho\Omega\gamma F_{\text{turb}}, \tag{5.48}$$

$$E_{\gamma 2}=C_{e2}P_{\gamma 2}\gamma, \tag{5.49}$$

where F_{length} is an empirical correlation that controls the transition length and Ω is the vorticity magnitude.

The momentum thickness Reynolds number, $\tilde{Re}_{\theta t}$, source term is given by:

$$P_{\theta t} = c_{\theta t}\frac{\rho}{t}\left(Re_{\theta t} - \tilde{Re}_{\theta t}\right)(1.0 - F_{\theta t}), \tag{5.50}$$

$$t = \frac{500\mu}{\rho U^2}, \tag{5.51}$$

$$F_{\theta t} = \min\left(\max\left(F_{\text{wake}}e^{(-y/\delta)^4}, 1.0 - \left(\frac{\gamma - 1/50}{1.0 - 1/50}\right)^2\right), 1.0\right), \tag{5.52}$$

$$\theta_{BL} = \frac{\tilde{Re}_{\theta t}\mu}{\rho U}, \tag{5.53}$$

$$\delta_{BL} = \frac{15}{2}\theta_{BL}, \tag{5.54}$$

$$\delta = \frac{50\Omega y}{U}\delta_{BL}, \tag{5.55}$$

$$Re_{\omega} = \frac{\rho\omega y^2}{\mu}, \tag{5.56}$$

$$F_{\text{wake}} = e^{-\left(Re_{\omega}/10^5\right)^2}. \tag{5.57}$$

The production and destruction terms for the modified k transport equation are:

$$G_k^* = \gamma_{\text{eff}}\tilde{G}_k, \tag{5.58}$$

$$Y_k^* = \min\left(\max\left(\gamma_{\text{eff}}, 0.1\right), 1, 0\right)Y_k. \tag{5.59}$$

Transition Onset

The transition onset is governed by the following parameters:

$$Re_\nu = \frac{\rho y^2 S}{\mu}, \tag{5.60}$$

$$Re_T = \frac{\rho k}{\mu \omega}, \tag{5.61}$$

$$F_{\text{onset1}} = \frac{Re_\nu}{2.193 Re_{\Theta c}}, \tag{5.62}$$

$$F_{\text{onset2}} = \min\left(\max\left(F_{\text{onset1}}, F_{\text{onset1}}^4\right), 2.0\right), \tag{5.63}$$

$$F_{\text{onset3}} = \max\left(1 - \left(\frac{R_T}{2.5}\right)^3, 0\right), \tag{5.64}$$

$$F_{\text{onset}} = \max\left(F_{\text{onset2}} - F_{\text{onset3}}, 0\right), \tag{5.65}$$

$$F_{\text{turb}} = e^{-\left(\frac{R_T}{4}\right)^4}. \tag{5.66}$$

Separation Induced Transition Correction

The correction for separation induced transition is:

$$\gamma_{\text{sep}} = \min\left(C_{s1} \max\left[\left(\frac{Re_\nu}{3.235 Re_{\theta c}}\right) - 1, 0\right] F_{\text{reattach}}, 2\right) F_{\theta t}, \tag{5.67}$$

$$F_{\text{reattach}} = e^{-(R_T/20)^4]}, \tag{5.68}$$

$$\gamma_{\text{eff}} = \max\left(\gamma, \gamma_{\text{sep}}\right). \tag{5.69}$$

Empirical Correlations

There are three proprietary empirical correlations embedded within the model that are not documented in the manual. The transition onset, $Re_{\theta t}$, the length of the transition zone, F_{length}, and the point where the model is activated, $Re_{\theta c}$, are functions of the following

parameters:

$$Re_{\theta t} = f(Tu, \lambda_\theta), \tag{5.70}$$

$$F_{\text{length}} = f(\tilde{R}e_{\theta t}), \tag{5.71}$$

$$Re_{\theta c} = f(\tilde{R}e_{\theta t}), \tag{5.72}$$

$$\lambda_\theta = \frac{\theta^2}{\nu}\frac{dU}{ds}, \tag{5.73}$$

where Tu is the turbulence intensity and dU/ds is the acceleration in the streamwise direction.

Constants

The constants used in the transition SST model are:

$$C_{a1} = 2, \tag{5.74}$$

$$C_{a2} = 0.06, \tag{5.75}$$

$$C_{e1} = 1, \tag{5.76}$$

$$C_{e2} = 50, \tag{5.77}$$

$$C_{\gamma} = 1.0, \tag{5.78}$$

$$C_{\gamma 3} = 0.5, \tag{5.79}$$

$$C_{s1} = 2, \tag{5.80}$$

$$c_{\theta t} = 0.03, \tag{5.81}$$

$$\sigma_{\theta t} = 2.0. \tag{5.82}$$

5.2.3 v^2f

Durbin's v^2f model modifies the k-ε model by adding two additional equations for the velocity variance, $\overline{v^2}$, and an elliptic relaxation function, f. It uses the velocity scale, $\overline{v^2}$,

rather than the turbulent kinetic energy, k, to calculate the eddy viscosity, which has a damping effect near the wall that reduces the overestimation of the near wall transport. The ANSYS® Fluent implementation of the v^2f model is documented in the ANSYS® Academic Research, Release 15.0, Help System, Fluent Theory Guide [97] and summarized below.

Transport Equations

The transport equation for the turbulent kinetic energy, k, turbulent dissipation, ε, velocity fluctuation normal to the streamlines, v^2f, and the elliptical relaxation function, f, are:

$$\frac{\partial\left(\rho k\right)}{\partial t}+\frac{\partial\left(\rho k u_i\right)}{\partial x_i}=P-\rho\varepsilon+\frac{\partial}{\partial x_j}\left[\left(\mu+\frac{\mu_t}{\sigma_k}\right)\frac{\partial k}{\partial x_j}\right]+S_k, \tag{5.83}$$

$$\frac{\partial\left(\rho\varepsilon\right)}{\partial t}+\frac{\partial\left(\rho\varepsilon u_i\right)}{\partial x_i}=\frac{C'_{\varepsilon1}P-C_{\varepsilon2}\rho\varepsilon}{T}+\frac{\partial}{\partial x_j}\left[\left(\mu+\frac{\mu_t}{\sigma_\varepsilon}\right)\frac{\partial\varepsilon}{\partial x_j}\right]+S_\varepsilon, \tag{5.84}$$

$$\frac{\partial\left(\rho\overline{v^2}\right)}{\partial t}+\frac{\partial\left(\rho\overline{v^2}u_i\right)}{\partial x_i}=\rho k f-6\rho\overline{v^2}\frac{\varepsilon}{k}+\frac{\partial}{\partial x_j}\left[\left(\mu+\frac{\mu_t}{\sigma_k}\right)\frac{\partial\overline{v^2}}{\partial x_j}\right]+S_{\overline{v^2}}, \tag{5.85}$$

$$f-L^2\frac{\partial^2 f}{\partial {x_j}^2}=(C_1-1)\frac{\frac{2}{3}-\frac{\overline{v^2}}{k}}{T}+C_2\frac{P}{\rho k}+\frac{5\frac{\overline{v^2}}{k}}{T}+S_f, \tag{5.86}$$

$$P=2\mu_t S^2, \tag{5.87}$$

$$C'_{\varepsilon1}=C_{\varepsilon1}\left(1+0.045\sqrt{\frac{k}{\overline{v^2}}}\right), \tag{5.88}$$

where S is the strain rate magnitude and S_k, S_ε, $S_{\overline{v^2}}$, and S_f are user defined source terms.

Time scale

The turbulent time scale is defined as:

$$T'=\max\left(\frac{k}{\varepsilon},6\sqrt{\frac{\nu}{\varepsilon}}\right), \tag{5.89}$$

$$T=\min\left(T',\frac{\alpha}{\sqrt{3}}\frac{k}{\overline{v^2}C_\mu}\sqrt{2S^2}\right). \tag{5.90}$$

Length Scale

The turbulent length scale is defined as:

$$L' = \min\left(\frac{k^{3/2}}{\varepsilon}, \frac{1}{\sqrt{3}}\frac{k^{3/2}}{\overline{v^2}C_\mu\sqrt{2S^2}}\right), \tag{5.91}$$

$$L = C_L \max\left(L', C_\eta\left(\frac{\nu^3}{\epsilon}\right)^{1/4}\right). \tag{5.92}$$

Turbulent Viscosity

The turbulent viscosity, μ_t, is calculated using:

$$\mu_t = \rho C_\mu \overline{v^2} T. \tag{5.93}$$

Constants

The constants used in the model are:

$$\alpha = 0.6, \tag{5.94}$$

$$C_1 = 1.4, \tag{5.95}$$

$$C_2 = 0.3, \tag{5.96}$$

$$C_{\varepsilon 1} = 1.4, \tag{5.97}$$

$$C_{\varepsilon 2} = 1.9, \tag{5.98}$$

$$C_\eta = 70, \tag{5.99}$$

$$C_\mu = 0.22, \tag{5.100}$$

$$C_L = 0.23, \tag{5.101}$$

$$\sigma_k = 1, \tag{5.102}$$

$$\sigma_\varepsilon = 1.3. \tag{5.103}$$

5.2.4 Inadequacy of the Basic *k*-ε Turbulence Model

The k-ε model is one of the most widely used turbulence models due to its low computational costs. However, it is widely accepted as doing a poor job for impinging jets [14]. A direct comparison between the k-ε model and the more advanced transition SST and v^2f turbulence models is difficult to perform because the different grid spacing requirements of the models lead to significantly different mesh sizes. The k-ε model is only valid for dimensionless wall spacing of $y^+ > 30$ while the transition SST and v^2f models require $y^+ < 1$. As a result, an appropriate mesh for the k-ε model will be coarser than an appropriate mesh for the transition SST and v^2f models. Most modern CFD codes with automatically include wall functions for cells where $y^+ < 30$ when using the k-ε model. An example of the variation in the solution obtained by changing the turbulence model is show in Figure 5.2. The k-ε model (—) drastically overestimates the turbulent kinetic energy near the wall, resulting in an artificially high heat transfer coefficient, which leads to an artificially low surface temperature. While the SST and v^2f models also overpredict the heat transfer coefficient at the surface, as will be shown below, they do a much better job than the traditional k-ε model.

5.3 Grid Independence

A grid independence study was conducted for a single geometry with an angle of 5°, a pitch of six jet diameters, a height of one jet diameter, and an average jet Reynolds number of 5,000. A coarse mesh was generated and the model was solved. The mesh was then refined and the model was solved again. This process of successively refining the mesh and solving the model was continued until grid independence for the solution was reached. Because of the nature of the two turbulence models being used, an additional constraint of $y^+ < 1$ for the first set of grid points from the surface was included in the grid independence check.

The meshing parameters for three of the meshes in the grid independence study are given in Table 5.1. For each of these meshes, all the parameters were identical except for the sizing of the elements at the impingement surface. Since impinging jet models are the most

Model	γ	P^*	H^*	L_n^*	Re_{D_n}	Profile
k-ε	5°	4	1	-	5,000	
SST	5°	4	1	-	5,000	
v^2f	5°	4	1	-	5,000	

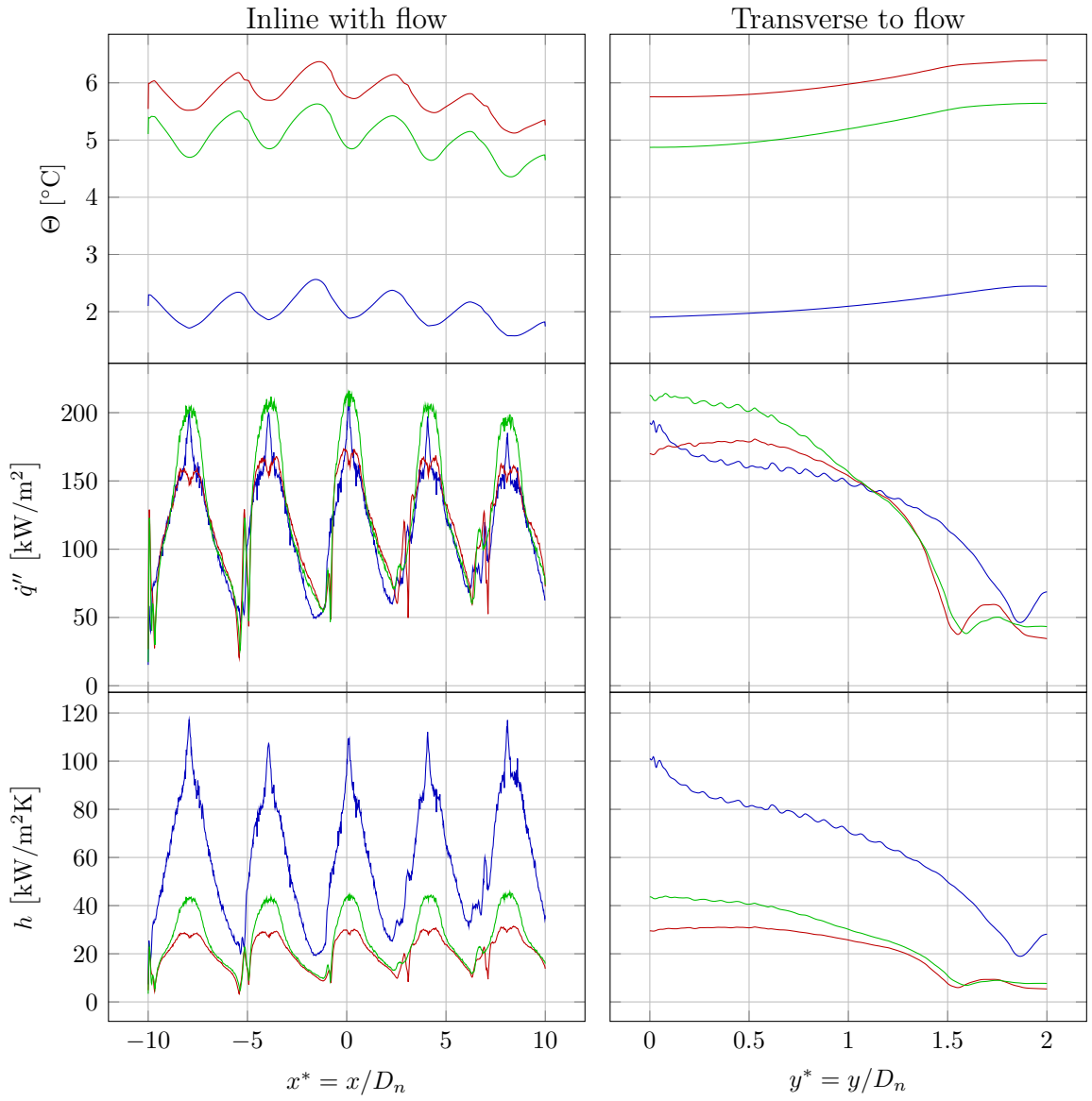

Figure 5.2: Turbulence model comparison

sensitive to grid sizing in the near wall region, the spacing between elements at the surface and the growth rate in grid spacing moving away from the wall were used to drive the mesh refinement process.

Table 5.1: Meshing parameters used for grid independence study

	Mesh ID		
	D	E	F
Physics Preference	CFD	CFD	CFD
Solver Preference	Fluent	Fluent	Fluent
Relevance	99	99	99
Relevance center	Fine	Fine	Fine
Smoothing	Medium	Medium	Medium
Transition	Slow	Slow	Slow
Span Angle Center	Fine	Fine	Fine
Minimum Edge Length (m)	1×10^{-6}	1×10^{-6}	1×10^{-6}
Maximum inflation layers	5	5	5
Inflation growth rate	1.2	1.2	1.2
Surface Element Sizing (m)	7.5×10^{-5}	5.0×10^{-5}	3.75×10^{-5}
Resulting Nodes	2.3×10^{6}	5.0×10^{6}	9.0×10^{6}

The solutions obtained using the transition SST and the v^2f turbulence models with the meshes listed in Table 5.1 are shown in Figure 5.3. The left column shows the surface profiles inline with the direction of flow along the center of the nozzles, and the right column shows the surface profiles transverse to the direction of flow starting directly underneath the central nozzle. The red lines (·····,- - -,——) represent the solutions for the transition SST model and the blue lines (·····,- - -,——) represent the solutions for the v^2f model. The dotted lines (·····,·····) represent the coarse grid, the dashed lines (- - -,- - -) represent the intermediate grid, and the solid lines (——,——) represent the fine grid.

The bottom row of axes in Figure 5.3 shows the values of y^+ for the grid points closest to the surface, where it can be seen that the coarse mesh results in $y^+ > 1$ in the regions around the stagnation points where the shear stress is the highest. As a result, the coarse grid does not meet the minimum requirements for resolving the behavior in the boundary layers and will not be used. However, both the intermediate and fine meshes maintain $y^+ < 1$ for the

$\gamma(^\circ)$	P^*	H^*	L_n^*	Re_{D_n}	Turbulence Model	Mesh ID	Number of Nodes	$\overline{h}$ (W/(m^2 · K))	Profile
5	6	1	-	5,000	SST	D	2.3×10^6	13,126	
5	6	1	-	5,000	SST	E	5.0×10^6	12,829	
5	6	1	-	5,000	SST	F	9.0×10^6	12,674	
5	6	1	-	5,000	v^2f	D	2.3×10^6	14,219	
5	6	1	-	5,000	v^2f	E	5.0×10^6	15,603	
5	6	1	-	5,000	v^2f	F	9.0×10^6	13,302	

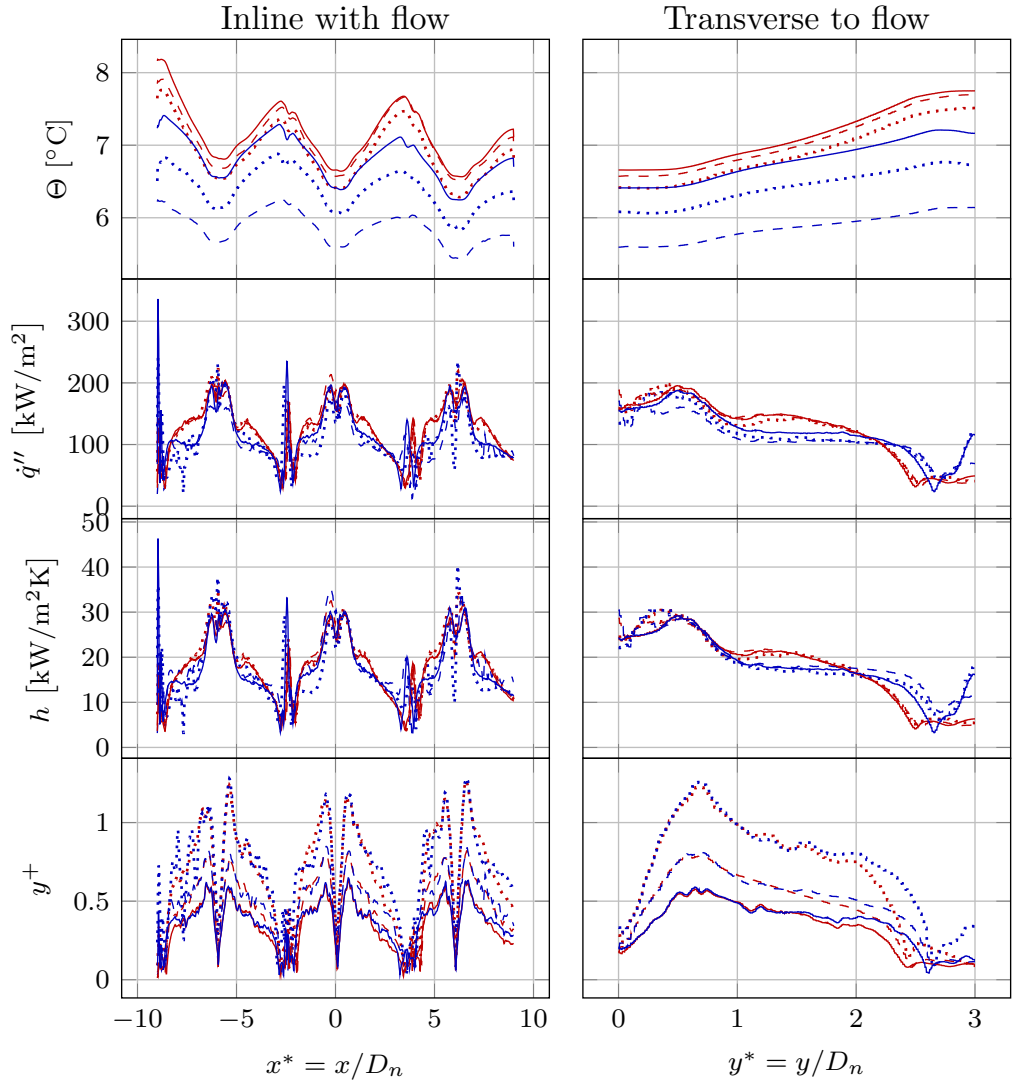

Figure 5.3: Variation in surface profiles with grid refinement

entire domain and are expected to capture the behavior of the boundary layers. Therefore, both the intermediate and the fine grids are acceptable for use on a y^+ basis. Additionally, the similarities between the y^+ profiles of the two turbulence models for each mesh confirm that the two models are producing comparable solutions for the shear stress near the surface.

The solutions for the intermediate grid with the SST turbulence model (- - -) and the fine grid with the SST turbulence model (——) have similar surface profiles for Θ, $\dot{q}''$, and h; and the resulting change in average heat transfer coefficient of approximately 1% is considered small enough to accept the solution from the intermediate grid with the SST turbulence model (- - -). Therefore, the parameters used to generate the intermediate mesh (- - -) were used to generate comparable meshes for the other geometries in the study for use with the SST turbulence model at a Reynolds number of 5,000.

The solutions for the intermediate grid with the v^2f turbulence model (- - -) and the fine grid with the v^2f turbulence model (——) have significantly different surface profiles for Θ, $\dot{q}''$, and $\overline{h}$; and the resulting change in average heat transfer coefficient of approximately 17% is too large to accept the solution from the intermediate grid (- - -) for the v^2f turbulence model. As a result, further refinement of the grid would be required to ensure grid independence for the v^2f model.

The v^2f model is significantly more computationally expensive than the SST model when using the same mesh size because the v^2f model required more under relaxation to maintain stability than did the SST model. Additionally, it is recommended that a previously converged solution from a more primitive model be used as the initial condition for the v^2f model [97]. The apparent benefits of using the v^2f model were relatively small, as the v^2f solution for the fine grid (——) was within 4% of the SST solution for the intermediate grid (- - -). For these reasons, it was determined that the possible benefits of using the v^2f model were outweighed by its costs, and the SST turbulence model was chosen instead.

5.4 Results

The meshing parameters from the grid independence study were used to generate meshes with: confining wall angles or 0°, 5°, and 10°; pitches of 6 jet diameters; and jet heights of 1, 2, and 3 jet diameters. Each geometry was solved for an average jet Reynolds number of 5,000.

5.4.1 Flow Field

Pressure Contours

The pressure contours for the 0°, 5°, and 10° confining walls are shown in Figure 5.4. For each geometry, the majority of the pressure drop occurs at the sharp edged inlet to the nozzle from the plenum. For each case, there is also an adverse pressure gradient in the stagnation region. The pressure drop experienced by the spent fluid as it moves toward the outlet decreases with increasing confining wall angle.

Pathlines

The pathlines for the 0°, 5°, and 10° confining walls are shown in Figure 5.5 colored by the magnitude of the fluid velocity. Since the solution was calculated for steady flow, the pathlines, streamlines, and streaklines coincide. For each geometry, the highest velocities occur in the upstream nozzle and in the wall jet region closest to the stagnation region where the boundary layer is thinnest. The stagnation region directly beneath each nozzle has a lower velocity magnitude than the surrounding fluid.

The fountain region where the neighboring wall jets meet and the fluid leaves the surface is clearly visible on the upstream side of the nozzles in Figure 5.5. For the more confined flows, the spent fluid causes the fountain region to shift downstream toward the outlet, with this effect increasing with decreasing confining wall angle. For the 0° confining wall, the momentum of the spent fluid increases with each downstream nozzle, causing the fountain

(a) 0° confining wall

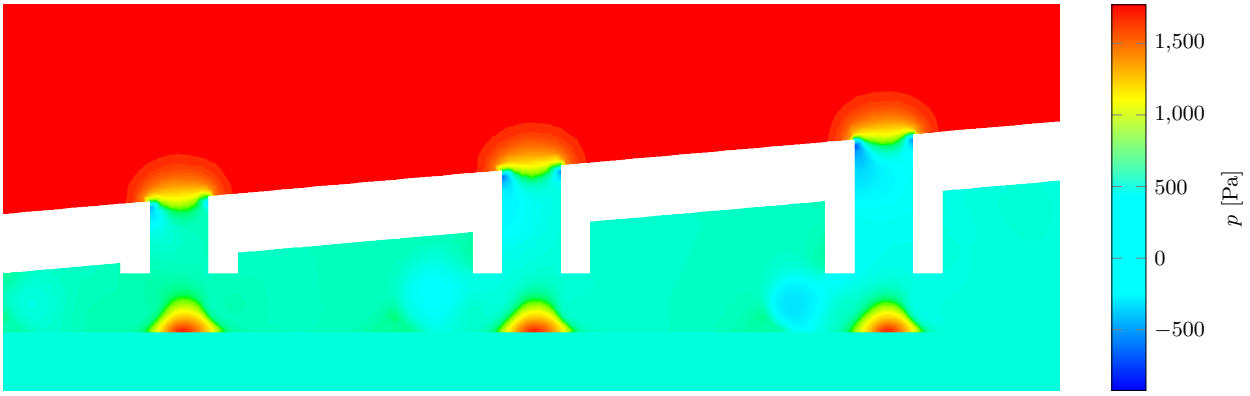

(b) 5° confining wall

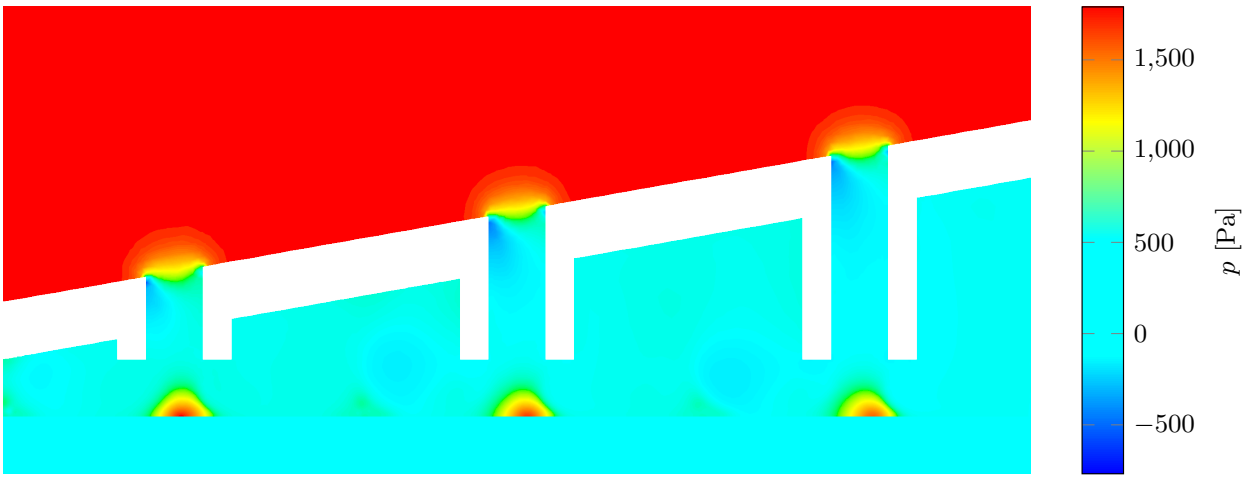

(c) 10° confining wall

Figure 5.4: Pressure contours along the symmetry plane inline with the flow for $Re_{D_n} = 5000$

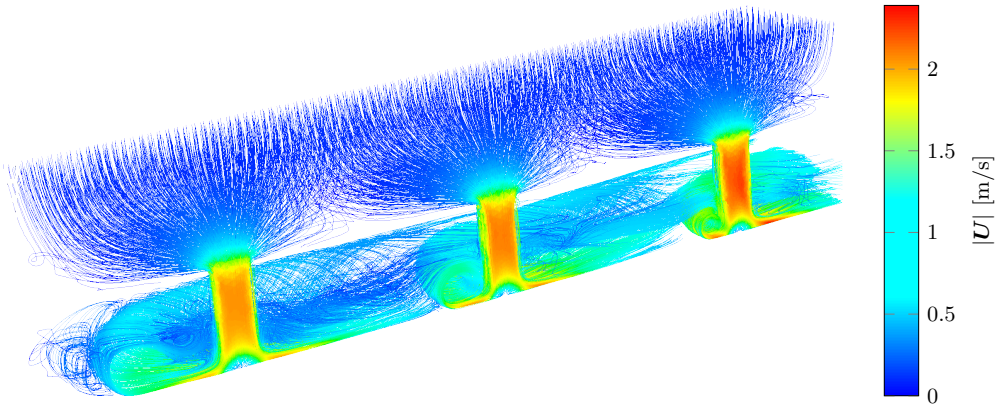

(a) 0° confining wall

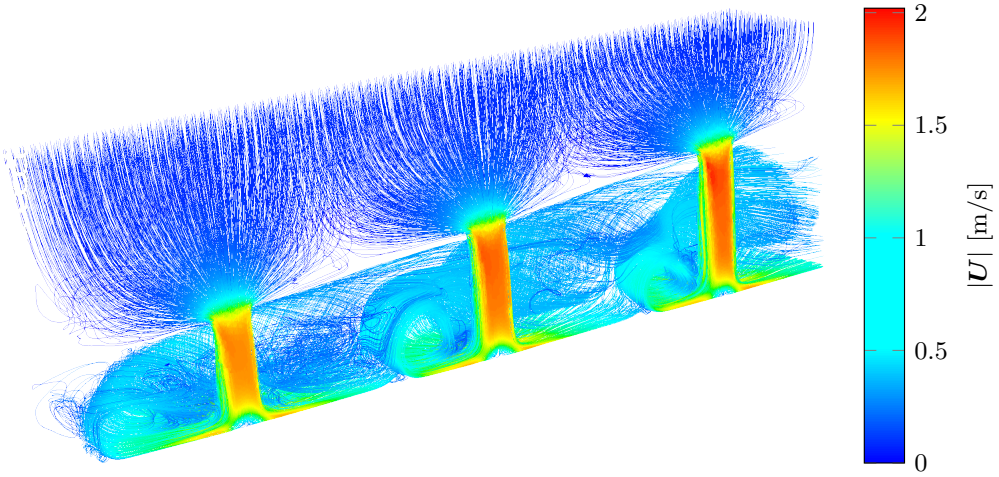

(b) 5° confining wall

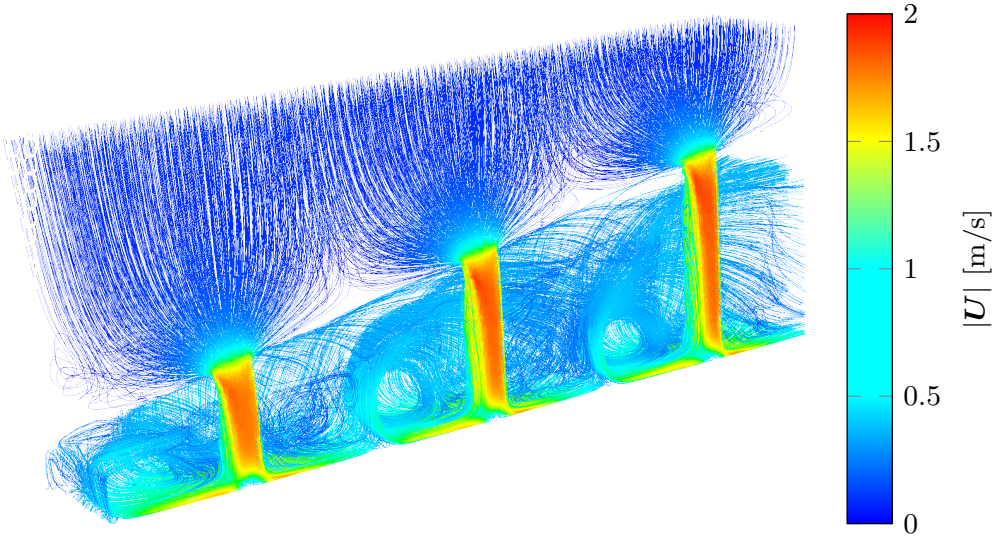

(c) 10° confining wall

Figure 5.5: Pathlines of the flow field colored by the velocity magnitude for $Re_{D_n} = 5000$

region to shift successively further downstream for each nozzle. However, the fountain region for the 10° confining does not shift downstream as the volumetric fluid of the spent fluid increases, because the relief provided by the increasing channel area prevents the momentum of the spent fluid from increasing.

Temperature Contours

The temperature contours for the 0°, 5°, and 10° confining walls are shown in Figure 5.6. Using a conjugate heat transfer model with conduction in the copper block and convection at the surface allows the effects of varying local heat flux at the surface to be captured. The conductive spreading in the copper block is evident from the regions of lower temperature in the copper block beneath each of the nozzles. Since the heat flux is higher in the stagnation region than in the wall jet region, the surface temperature beneath the stagnation region tends to be lower than the surface temperature away from the stagnation region. This causes additional heat to be conducted into the portion of the block beneath the jet.

The fountain region shows up clearly in the temperature contours in Figure 5.6. As the fluid flows along the surface in the wall jet region, it absorbs energy from the surface and a thermal boundary layer forms. When the neighboring wall jets collide, the warm fluid in the boundary layer separates and flows away from the surface, causing the rise in fluid temperature seen Figure 5.6. As the warm fluid in the fountain moves into the bulk spent fluid, it mixes with the cooler fluid and drops to the bulk temperature.

5.4.2 Surface Properties

Temperature Contours

The surface temperature rise contours for the 0°, 5°, and 10° confining walls are shown in Figure 5.7. The lowest surface temperatures for each case occur beneath the stagnation region below each nozzle. For each case shown in Figure 5.7, the spent fluid outlet is on the right. The shape of the temperature contours are more circular around the first nozzle in

(a) 0° confining wall

(b) 5° confining wall

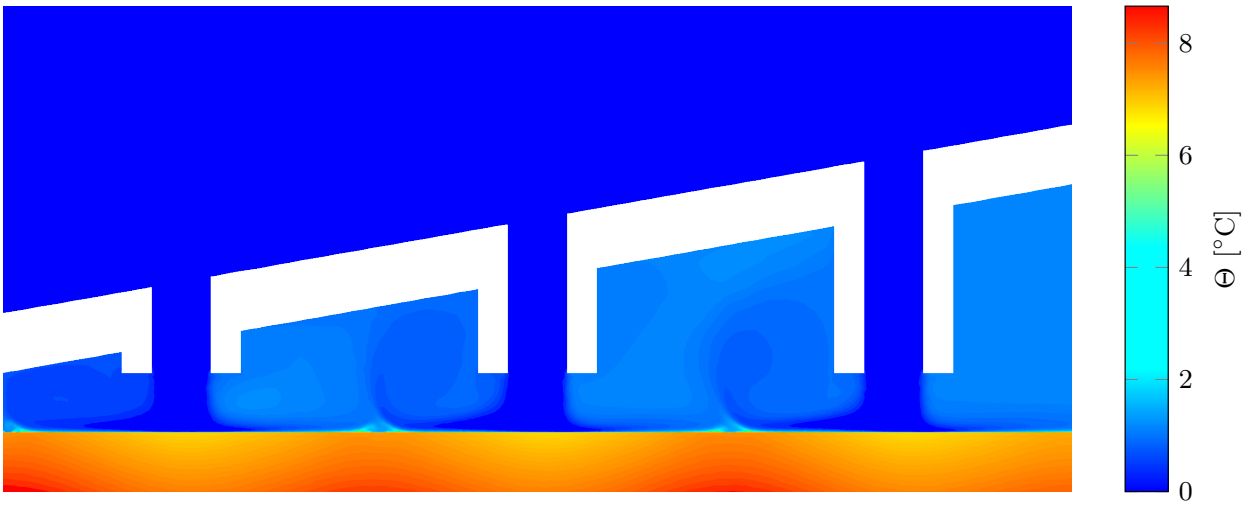

(c) 10° confining wall

Figure 5.6: Temperature contours along the symmetry plane inline with the flow for $Re_{D_n} = 5000$

each case than are the temperature contours around the downstream nozzles. The distortion of the circular shape increases with decreasing confining wall angle, due to the additional confinement at the lower angles. For the highly confined cases, the higher momentum of the spent fluid causes the fountain regions and wall jets to shift downstream toward the exit, which in turn causes the temperature profile to shift toward the exit.

(a) 0° confining wall

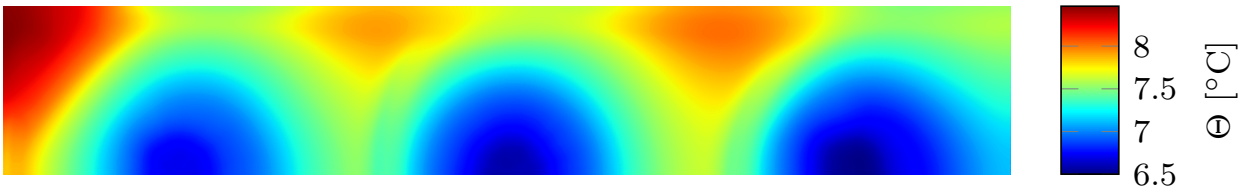

(b) 5° confining wall

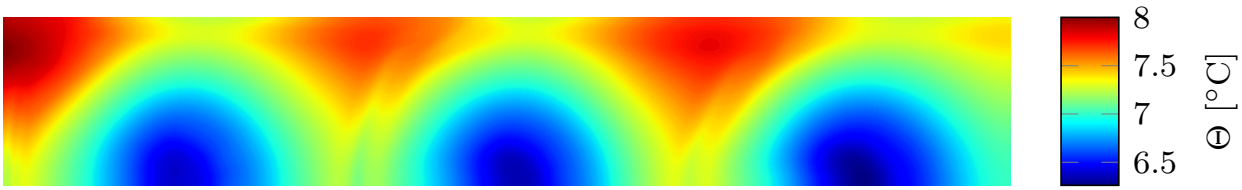

(c) 10° confining wall

Figure 5.7: Surface temperature contours for $Re_{D_n} = 5000$

An important feature of Figure 5.7 is that the region of low temperature around each nozzle decreases in size for the 0° confining wall; however, it remains approximately the same size for the 5° and 10° confining walls. This is indicative of the thermal performance decreasing for the 0° confining wall and staying approximately constant for the 5° and 10° confining walls with downstream position.

Heat Flux Contours

The heat flux contours for the 0°, 5°, and 10° confining walls are shown in Figure 5.8. The heat flux is highest in the stagnation regions for each case with secondary peaks occurring in the fountain regions. The secondary peaks help to illustrate the shifting of the fountains in the downstream direction. Similar to trends seen in the temperature contours in Figure 5.7, the heat flux decreases with each downstream nozzle for the 0° confining wall, whereas it remains approximately constant in the downstream direction for the 5° and 10° confining walls.

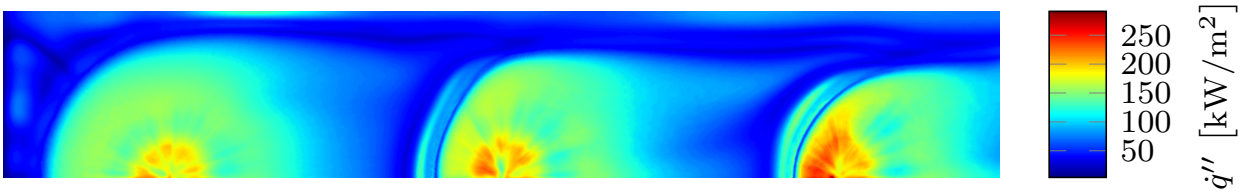

(a) 0° confining wall

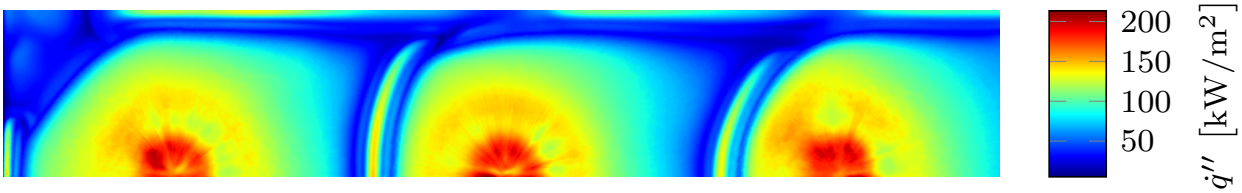

(b) 5° confining wall

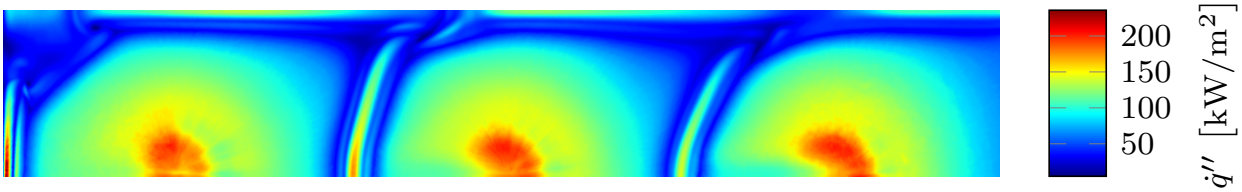

(c) 10° confining wall

Figure 5.8: Heat flux contours for $Re_{D_n} = 5000$

Heat Transfer Coefficient Contours

The heat transfer coefficient contours for the 0°, 5°, and 10° confining walls are shown in Figure 5.9. The heat transfer coefficient is a combination of the temperature rise at the

surface, shown in Figure 5.7, and the local heat flux, shown in Figure 5.8. Therefore, the same trends that were seen for the surface temperature and surface heat flux are seen here as well.

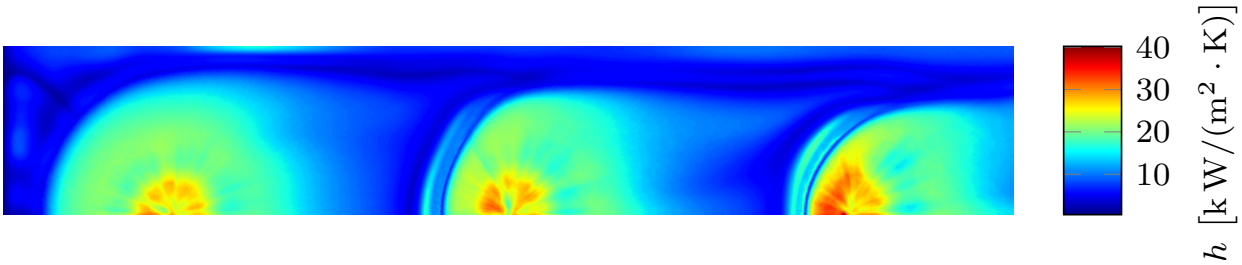

(a) 0° confining wall

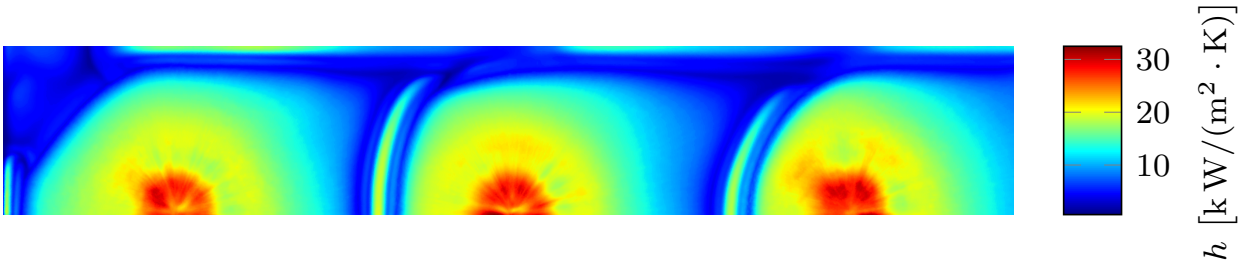

(b) 5° confining wall

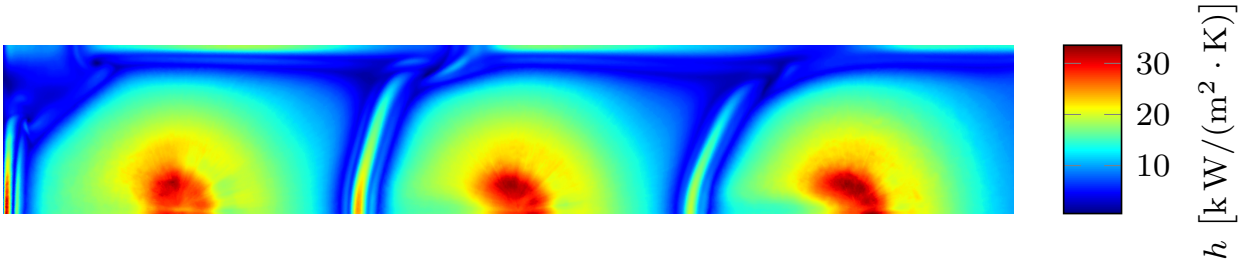

(c) 10° confining wall

Figure 5.9: Heat transfer coefficient contours for $Re_{D_n} = 5000$

5.4.3 Comparison to Experiment

While the transition SST turbulence model is recognized as doing a better job of predicting the performance of impinging jet systems than many of the other turbulence models, it is known to overpredict the rates of heat transfer by 20-30% [14]. A comparison of the experimentally measured local values and numerically calculated local values along the surface

in the inline and transverse directions are show in Figure 5.10. The solid lines (—,—,—) represent the values from the model and the dashed lines (- - -,- - -,- - -) represent the experimental values. The experimental and numerical surface average heat transfer coefficients are compared in Table 5.2, where is it seen that differences between the model and the experiment are on the order of 50–65%.

Table 5.2: Comparison of surface average heat transfer coefficients between the model and the experiment

γ	P^*	H^*	L_n^*	$\overline{h}\,(\mathrm{kW/(m^2 \cdot K)})$		
				Exp.	CFD	$\%_{\mathrm{diff}}$
0°	6	1	0	6.87	11.79	52.7
5°	6	1	0	7.04	12.83	58.3
10°	6	1	0	6.97	13.27	62.3

There are a few main caveats to the comparison between the model and the experiment in Figure 5.10 and Table 5.2 beyond the expected overprediction of the SST turbulence model. First, the model employs two symmetry boundary conditions which implies an infinite array of nozzle in the transverse direction, while the experiment has only one additional set of nozzles followed by wall in the transverse direction. Second, the linear fit used in the experiment to extrapolate the surface values is expected to underestimate the regions of high local heat flux and overestimate the regions of low local heat flux. Third, the average jet Reynolds numbers of the two cases are similar but not identical. Fourth, the resolution of the local measurements is much lower than the resolution of the model, with the locations of the local maximum and minimum heat flux as predicted by the model falling between the measured locations of the experiment.

5.4.4 Additional Downstream Nozzles

While the target application is expected to have more than three rows of nozzles, the majority of the modeling was done using a small scale model with three nozzles in the downstream direction to both decrease the computational costs and to enable direct comparison

Source	γ	P^*	H^*	L_n^*	Re_{D_n}	Profile
CFD	0°	6	1	0	5,000	
Exp.	0°	6	1	0	5,600	
CFD	5°	6	1	-	5,000	
Exp.	5°	6	1	-	5,600	
CFD	10°	6	1	-	5,000	
Exp.	10°	6	1	-	5,600	

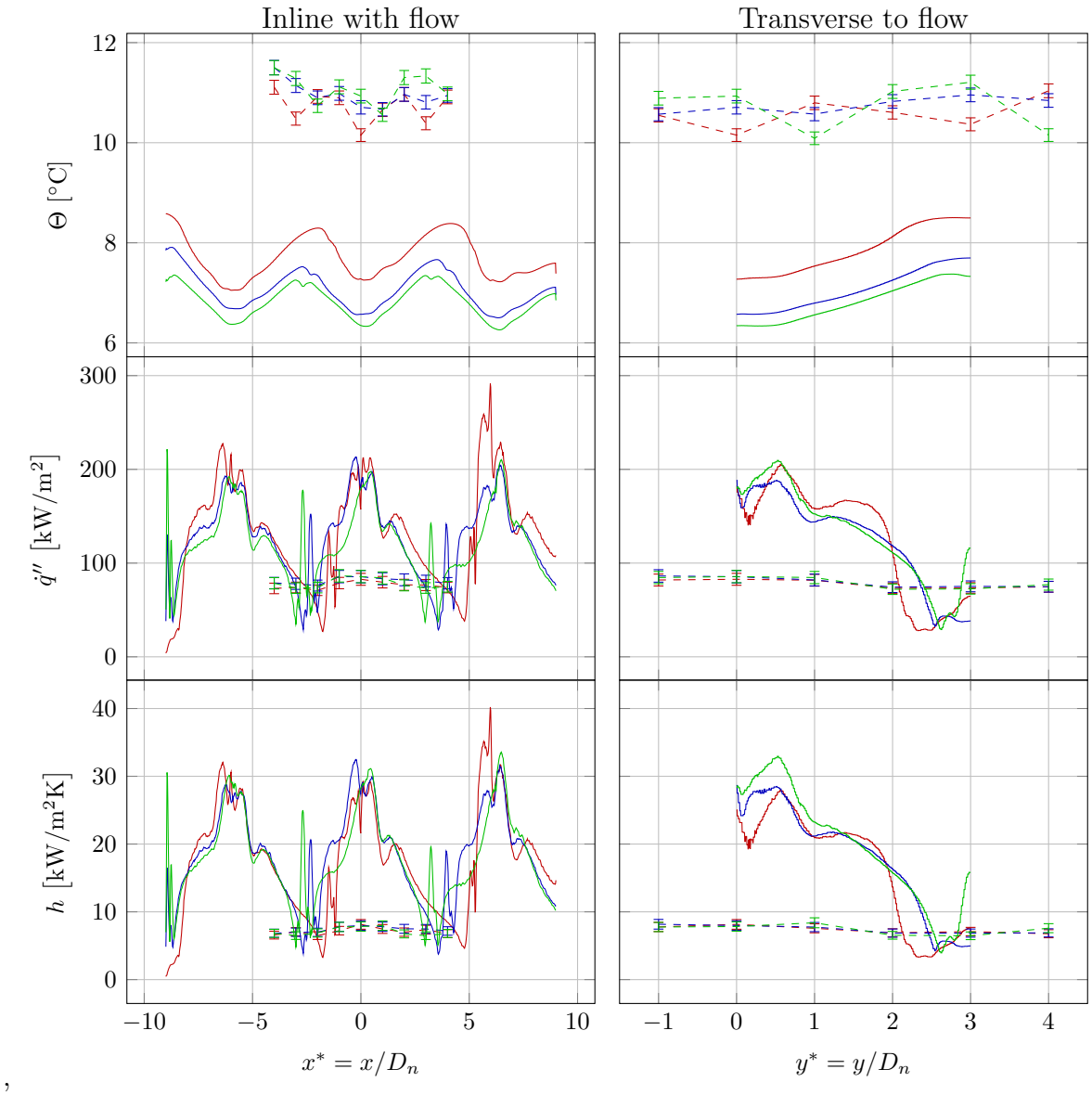

,

Figure 5.10: Comparison of experimental results and modeling results

to the experimental data. It is expected that the behaviors and trends seen in the three nozzle models will continue to be present when the nozzle array is extended to additional rows. In order to verify this, select cases were extended to include five nozzles.

Pressure Contours

The pressure contours for the 0° and 5° confining walls with five nozzles are shown in Figure 5.11. As was seen for three nozzles, the majority of the pressure drop occurs at the sharp edged inlet to the nozzle from the plenum. Also, the pressure drop experienced by the spent fluid as it moves toward the outlet is higher for the 0° confining wall than it is for the 5° confining wall.

(a) 0° confining wall

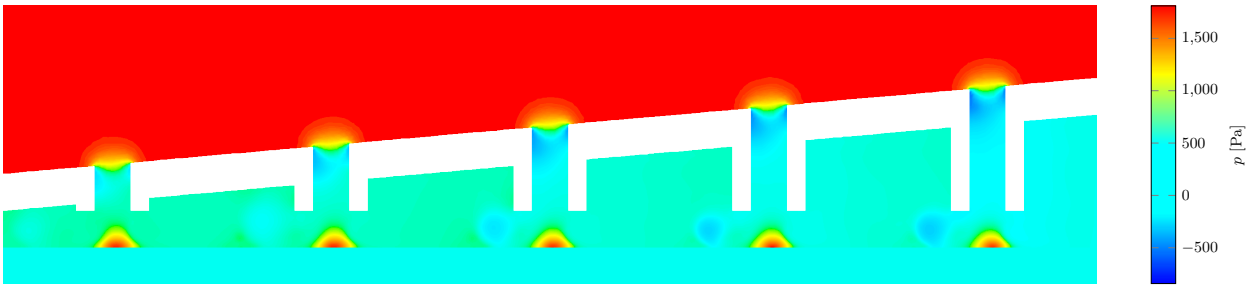

(b) 5° confining wall

Figure 5.11: Pressure contours along the symmetry plane inline with the flow for five nozzles with $Re_{D_n} = 5000$

Pathlines

The pathlines for the 0° and 5° confining walls with five nozzles are shown in Figure 5.12 colored by the magnitude of the fluid velocity. As was seen for three nozzles, the fountains shift further downstream for each successive nozzle, with this behavior being more

pronounced in the highly confined flow of the 0° confining wall. Additionally, due to the large pressure drop experienced by the spent fluid for the 0° confining wall, the flow distribution from the plenum is less uniform for the 0° confining wall than for the 5° confining wall, with the downstream nozzles having higher flow rates than the upstream nozzles. The nonuniform flow distribution was present for cases when the fluid entered the plenum from the top and when it entered the plenum parallel to the surface from the upstream side.

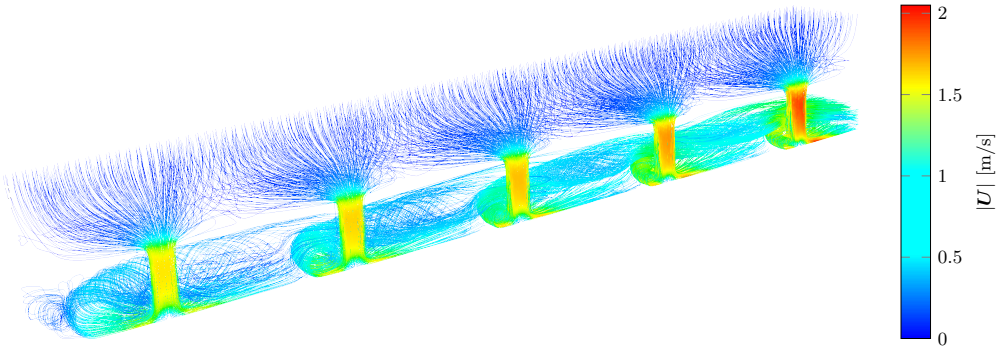

(a) 0° confining wall

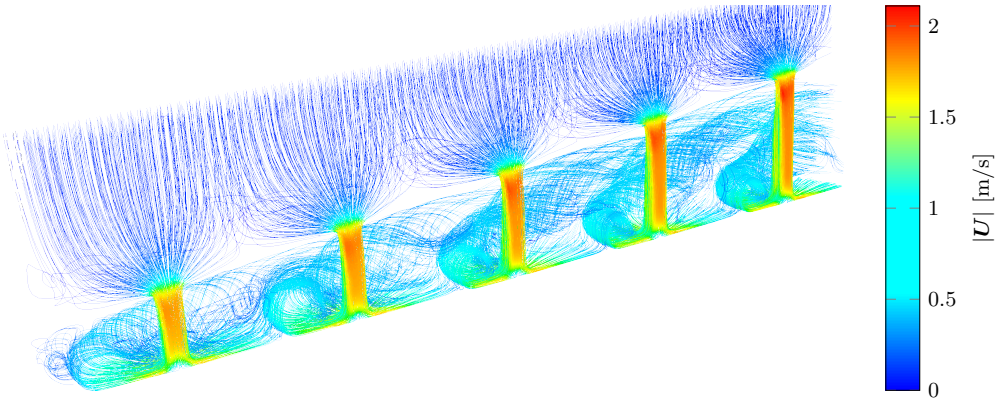

(b) 5° confining wall

Figure 5.12: Pathlines of the flow field colored by the velocity magnitude for five nozzles with $Re_{D_n} = 5000$

Surface Temperature Contours

The surface temperature rise contours for the 0° and 5° confining walls with five nozzles are shown in Figure 5.13. The same trend of decreasing thermal performance with downstream position for the 0° confining wall as was seen for three nozzles is present for five

nozzles as well. In both the three nozzle and five nozzle cases, the last nozzle in the array exhibits a rise in thermal performance, which could be attributed to the increased flow rate in the last nozzle when compared to the upstream nozzles. The 5° confining wall maintains a more uniform thermal performance with downstream position, which is desirable because it will lead to less severe temperatures gradients within the device being cooled.

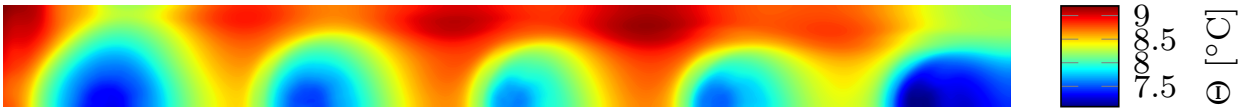

(a) 0° confining wall

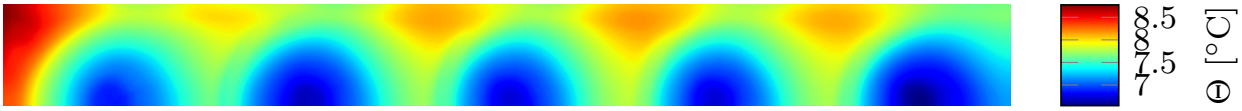

(b) 5° confining wall

Figure 5.13: Surface temperature contours for five nozzles with $Re_{D_n} = 5000$

Heat Transfer Coefficient Contours

The heat transfer coefficient contours for the 0° and 5° confining walls with five nozzles are shown in Figure 5.14. Similar to the results seen in the temperature contours in Figure 5.13, the thermal performance of the 0° confining wall decreases with downstream position. The accumulation of spent fluid momentum in the 0° confining wall causes the area of elevated heat transfer in the stagnation and wall jet regions to get successively smaller with each downstream nozzle. However, the 5° confining wall maintains a consistent momentum for the spent fluid, and the area of elevated heat transfer for each nozzle stays constant with downstream position, thus providing more uniform cooling of the surface.

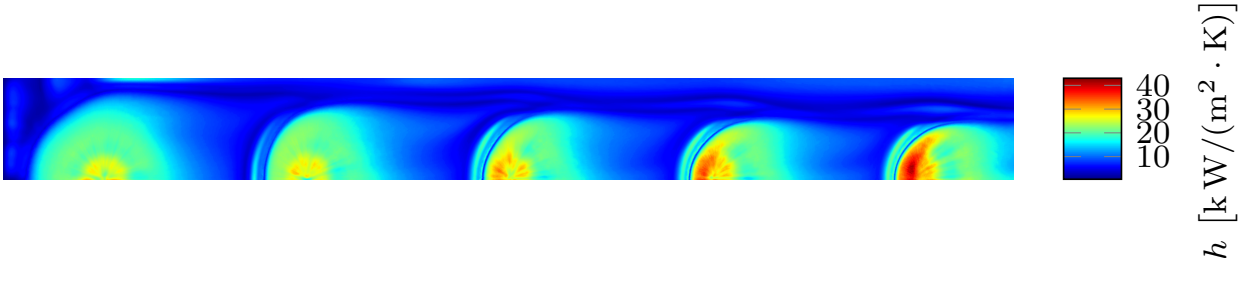

(a) 0° confining wall

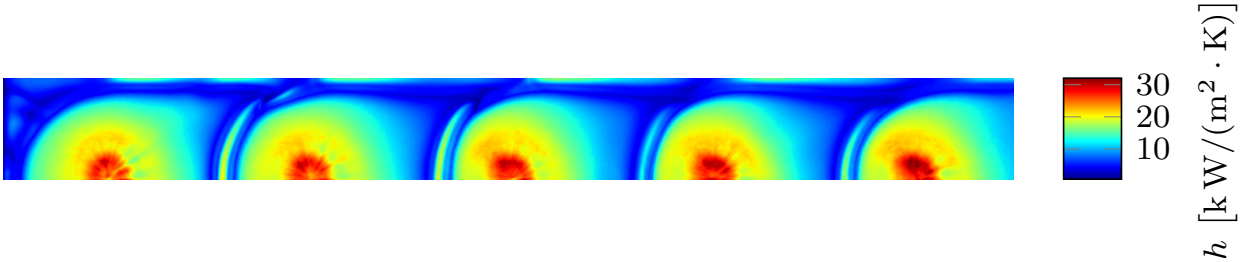

(b) 5° confining wall

Figure 5.14: Heat transfer coefficient contours for five nozzles with $Re_{D_n} = 5000$

Chapter 6

Conclusion

Cooling systems that use arrays of impinging liquid jets are well suited for automotive power electronic applications due to their relatively high volumetric flow rates and low pressure drops when compared to competing technologies. Impinging liquid jets are capable of producing the highest local heat transfer coefficient in the stagnation region of currently available single-phase liquid cooling techniques. However, when arrays of impinging jets are used to cool large surface areas, the spent fluid from upstream jets can interfere with and degrade the performance of downstream jets. In order to reduce the detrimental effects of the spent fluid, systems have been developed to locally remove the spent fluid from each jet. However, this work proposes a simpler method of managing the spent flow by introducing an angled confining wall to maintain a constant momentum ratio between the spent fluid crossflow and the downstream incoming jets.

In order to characterize the effects of changing the confining wall angle, an experimental apparatus was developed that is capable of measuring the temperature, local heat flux, and local heat transfer coefficient at the surface of a copper block. The spatial resolution of the surface measurements was increased by translating the jet array relative to the sensors, allowing the generation of 2-D maps of the local thermal surface properties.

The effects of confining wall angle, jet pitch, jet height, and Reynolds number on the heat transfer of a 3×3 array of circular, normal, single-phase, liquid jets with a common outlet were investigated. The highest heat transfer for the orifice plates occurred at a pitch of six jet diameters and a height of two jet diameters, while the highest heat transfer for the angled confining wall occurred at a pitch of four jet diameters and a height of one jet diameter, both of which had an average heat transfer coefficient of $13{,}100\,\mathrm{W/(m^2 \cdot K)}$ at

an average jet Reynolds number of 14,000. Although these two configurations have the same thermal performance, the measured trends suggest that decreasing the pitch and jet height could further improve the performance of the angled confining wall, while no such improvement would be possible for the orifice plate.

Strong interactions between the effects of varying the wall angle, jet pitch, and jet height were observed. The heat transfer increased with increasing Reynolds number for every configuration tested. However, the interaction between the geometric parameters did not have a strong dependence on Reynolds number. The benefits of the angled confining wall were more pronounced for lower pitches and jet heights. This suggests that the angled wall provides enough relief for the spent fluid to not interfere with the incoming jets, making it an effective and efficient method for spent flow management of jet impingement cooling of power electronics.

The experimental results were for the central jet in a 3×3 array. As the array is extended to include additional rows of downstream jets, it is expected that the parallel confining wall will cause a degradation in performance as the momentum of the spent fluid increases with increasing volumetric flow rate. However, the systems with an angled confining wall are expected to maintain their performance with additional downstream jets because the increasing channel height will allow for a more consistent momentum ratio between the spent fluid and the incoming jets. In order to confirm this expected behavior, a CFD model was developed using ANSYS® Fluent to analyze the effect of altering the geometric parameters to values not included in the experimental matrix.

Menter's transition SST model [98] and Durbin's v^2f model [92] were both considered for modeling the turbulence. The transition SST model was selected for this study because it was determined that the added computational cost of the v^2f model outweighed its potential benefits. A mesh refinement study was performed to ensure grid independence of the solution and to ensure $y^+ < 1$ for the first set of grid points from the surface. The resulting meshes

were on the order of 5 million nodes when using an average jet Reynolds number of 5,000 for three nozzles.

Models were generated for direct comparison to the experimental data, with the difference between the model and experimental values being on the order of 50–65%. Because the SST turbulence model is known to overpredict the surface transfer rate, the CFD model was used to analyze trends and to predict the relative effects of altering geometric parameters rather than to predict the absolute performance.

The expected trends of decreasing thermal performance in the downstream direction for the 0° confining wall and constant thermal performance in the downstream direction for the 5° confining wall were confirmed with the CFD model. This further supports the claim that the 5° confining wall is an effective method for spent flow management, with its beneficial effects continuing to increase as the array is extended to include more rows in the downstream direction.

6.1 Recommendations for Future Work

The target application for the system described in this work is the cooling of automotive power electronics. It is desirable to incorporate the liquid cooling into the WEG flow loop already present on the vehicle to cut down on manufacturing and operational costs. While the thermal performance is expected to scale with the Reynolds and Prandtl numbers when changing the fluid, it would be worthwhile to verify this by conducting a set of experiments for select geometric configurations.

The jet-to-jet interaction is driven in part by the distance between the jets, which results in a minimum distance between the jets that must be maintained for optimal performance. By placing the nozzles in evenly spaced rows and columns, a region of low heat transfer is created that is equidistant from each of the four neighboring jets. However, by staggering the nozzles, more jets can be placed per unit area while still maintaining the same distance

between neighboring jets. This is expected to produce a more uniform cooling of the surface; however, the implications of this on the transverse fountain region would need to be investigated.

The impingement surface used in this study was a flat piece of copper. It is expected that the heat transfer could be further improved by combining the proposed spent flow management with surface modifications. While the effects of the surface modifications on the spent flow field will need to be investigated, a few possible modifications are to:

- increase or decrease the surface roughness,
- add micro/mini fins,
- add concave structures beneath the jets based on the locations of the fountain regions.

When modifying the surface to include fins with comparable length scales to the jet diameter, care must be taken to avoid degrading the thermal performance by impeding the heat transfer in the stagnation region.

This study used simple straight tubes for the nozzles. However, the nozzle inlet and outlet geometries can have significant impacts on both the thermal performance and the pressure drop of the system. The largest pressure drop in the system was observed at the nozzle inlet in the CFD study. This could be improved by using a rounded inlet rather than a sharp edged inlet.

A flat confining wall was used for every case in this study. However, the ideal shape of the confining wall may be curved rather than a constant flat angle. Additionally, the nozzles were normal to the surface in each case. New jet plates could be fabricated using a 3-D printer to test various wall curvatures and impingement angles.

Each nozzle in this study had the same internal diameter. The results of the CFD study suggest that the flow is not evenly distributed among the nozzles, with the flow rate per nozzle increasing in the downstream direction. In order to maintain a more uniform flow distribution, the nozzle diameter could be varied based on the downstream location.

The velocity profile of the fluid when it leaves the nozzle can have significant impacts on the heat transfer at the surface. Sophisticated nozzles could be produced to alter the flow properties of the fluid leaving the nozzle by:

- disrupting the developed velocity profile with a sharp edged orifice at the nozzle exit,
- introducing an obstruction to increase turbulence,
- using a helical structure along the inside wall of the nozzle to induce swirl in fluid.

Bibliography

[1] K. Sheng, B. W. Williams, and S. J. Finney. A review of IGBT models. *Power Electronics, IEEE Transactions on*, 15(6):1250–1266, 2000.

[2] Z. Liang. Status and trend of automotive power packaging. In *the 24th International Symposium on Power Semiconductor Devices and ICs (ISPSD)*, pages 325–331. IEEE, 2012.

[3] J. Schulz-Harder. Review on highly integrated solutions for power electronic devices. In *the 5th International Conference on Integrated Power Systems (CIPS)*, pages 1–7. IEEE, 2008.

[4] S. S. Kang. Advanced cooling for power electronics. In *the 7th International Conference on Integrated Power Electronics Systems (CIPS)*, pages 1–8. IEEE, 2012.

[5] P. Wang, P. McCluskey, and A. Bar-Cohen. Two-phase liquid cooling for thermal management of IGBT power electronic module. *Journal of Electronic Packaging*, 135 (2):021001, 2013.

[6] J. F. Maddox, R. W. Knight, and S. H. Bhavnani. TIM selection for an IGBT cold plate using experimental and numerical modeling. In *the 12th International Technical Conference and Exhibition on Packaging and Integration of Electronic and Photonic Microsystems (InterPACK)*, page V002T08A045. ASME, 2013.

[7] D.-Y. Lee and K. Vafai. Comparative analysis of jet impingement and microchannel cooling for high heat flux applications. *International Journal of Heat and Mass Transfer*, 42(9):1555–1568, 1999.

[8] A. J. Robinson. A thermal–hydraulic comparison of liquid microchannel and impinging liquid jet array heat sinks for high-power electronics cooling. *Components and Packaging Technologies, IEEE Transactions on*, 32(2):347–357, 2009.

[9] C. D. Donaldson and R. S. Snedeker. A study of free jet impingement. part 1. mean properties of free and impinging jets. *J. Fluid Mech*, 45(2):281–319, 1971.

[10] H. Martin. Heat and mass transfer between impinging gas jets and solid surfaces. *Advances in Heat Transfer*, 13:1–60, 1977.

[11] K. Jambunathan, E. Lai, M. Moss, and B. Button. A review of heat transfer data for single circular jet impingement. *International Journal of Heat and Fluid Flow*, 13(2): 106–115, 1992.

[12] R. Viskanta. Heat transfer to impinging isothermal gas and flame jets. *Experimental Thermal and Fluid Science*, 6(2):111–134, 1993.

[13] B. Webb and C. Ma. Single-phase liquid jet impingement heat transfer. *Advances in Heat Transfer*, 26(2):105–217, 1995.

[14] N. Zuckerman and N. Lior. Jet impingement heat transfer: Physics, correlations, and numerical modeling. *Advances in Heat Transfer*, 39(06):565–631, 2006.

[15] J. Lee and S.-J. Lee. The effect of nozzle configuration on stagnation region heat transfer enhancement of axisymmetric jet impingement. *International Journal of Heat and Mass Transfer*, 43(18):3497–3509, 2000.

[16] C. McDaniel and B. Webb. Slot jet impingement heat transfer from circular cylinders. *International Journal of Heat and Mass Transfer*, 43(11):1975–1985, 2000.

[17] B. P. Whelan and A. J. Robinson. Nozzle geometry effects in liquid jet array impingement. *Applied Thermal Engineering*, 29(11):2211–2221, 2009.

[18] S. Maurel and C. Solliec. A turbulent plane jet impinging nearby and far from a flat plate. *Experiments in Fluids*, 31(6):687–696, 2001.

[19] S. Slayzak, R. Viskanta, and F. Incropera. Effects of interaction between adjacent free surface planar jets on local heat transfer from the impingement surface. *International Journal of Heat and Mass Transfer*, 37(2):269–282, 1994.

[20] L. Aldabbagh and I. Sezai. Numerical simulation of three-dimensional laminar multiple impinging square jets. *International Journal of Heat and Fluid Flow*, 23(4):509–518, 2002.

[21] A. M. Huber and R. Viskanta. Effect of jet-jet spacing on convective heat transfer to confined, impinging arrays of axisymmetric air jets. *International Journal of Heat and Mass Transfer*, 37(18):2859–2869, 1994.

[22] A. C. Chambers, D. R. Gillespie, P. T. Ireland, and G. M. Dailey. Cooling performance of a narrow impingement channel including the introduction of cross flow upstream of the first hole. In *ASME 2003 International Mechanical Engineering Congress and Exposition*, pages 131–142. American Society of Mechanical Engineers, 2003.

[23] L. W. Florschuetz, R. Berry, and D. Metzger. Periodic streamwise variations of heat transfer coefficients for inline and staggered arrays of circular jets with crossflow of spent air. *Journal of Heat Transfer*, 102(1):132–137, 1980.

[24] L. Florschuetz, C. Truman, and D. Metzger. Streamwise flow and heat transfer distributions for jet array impingement with crossflow. *Journal of Heat transfer*, 103(2): 337–342, 1981.

[25] L. Florschuetz, D. Metzger, and C. Su. Heat transfer characteristics for jet array impingement with initial crossflow. *Journal of Heat transfer*, 106(1):34–41, 1984.

[26] S. Gao and P. R. Voke. Large-eddy simulation of turbulent heat transport in enclosed impinging jets. *International Journal of Heat and Fluid Flow*, 16(5):349–356, 1995.

[27] C. Hoogendoorn. The effect of turbulence on heat transfer at a stagnation point. *International Journal of Heat and Mass Transfer*, 20(12):1333–1338, 1977.

[28] K. Abe and K. Suga. Large eddy simulation of passive scalar in complex turbulence with flow impingement and flow separation. *Heat Transfer–Asian Research*, 30(5):402–418, 2001.

[29] D. Cooper, D. Jackson, B. E. Launder, and G. Liao. Impinging jet studies for turbulence model assessmenti. flow-field experiments. *International Journal of Heat and Mass Transfer*, 36(10):2675–2684, 1993.

[30] R. Gardon and J. C. Akfirat. The role of turbulence in determining the heat-transfer characteristics of impinging jets. *International Journal of Heat and Mass Transfer*, 8 (10):1261–1272, 1965.

[31] Y. M. Chung and K. H. Luo. Unsteady heat transfer analysis of an impinging jet. *Journal of Heat Transfer*, 124(6):1039–1048, 2002.

[32] M. Behnia, S. Parneix, Y. Shabany, and P. Durbin. Numerical study of turbulent heat transfer in confined and unconfined impinging jets. *International Journal of Heat and Fluid Flow*, 20(1):1–9, 1999.

[33] V. Narayanan, J. Seyed-Yagoobi, and R. Page. An experimental study of fluid mechanics and heat transfer in an impinging slot jet flow. *International Journal of Heat and Mass Transfer*, 47(8):1827–1845, 2004.

[34] N. Zuckerman and N. Lior. Impingement heat transfer: correlations and numerical modeling. *Journal of Heat Transfer*, 127(5):544–552, 2005.

[35] J.-C. Han, S. Dutta, and S. Ekkad. *Gas turbine heat transfer and cooling technology*. CRC Press, 2012.

[36] H. Taniguchi, S. Miyamae, N. Arai, and N. Lior. Power generation analysis for high-temperature gas turbine in thermodynamic process. *Journal of Propulsion and Power*, 16(4):557–561, 2000.

[37] C. Gau and C. Chung. Surface curvature effect on slot-air-jet impingement cooling flow and heat transfer process. *Journal of Heat Transfer*, 113(4):858–864, 1991.

[38] A. Fleischer, K. Kramer, and R. Goldstein. Dynamics of the vortex structure of a jet impinging on a convex surface. *Experimental Thermal and Fluid Science*, 24(3):169–175, 2001.

[39] F. Gori and L. Bossi. Optimal slot height in the jet cooling of a circular cylinder. *Applied Thermal Engineering*, 23(7):859–870, 2003.

[40] C. Cornaro, A. Fleischer, and R. Goldstein. Flow visualization of a round jet impinging on cylindrical surfaces. *Experimental Thermal and Fluid Science*, 20(2):66–78, 1999.

[41] N. Kayansayan and S. Küçüka. Impingement cooling of a semi-cylindrical concave channel by confined slot-air-jet. *Experimental Thermal and Fluid Science*, 25(6):383–396, 2001.

[42] K. Bilen, K. Bakirci, S. Yapici, and T. Yavuz. Heat transfer from a plate impinging swirl jet. *International Journal of Energy Research*, 26(4):305–320, 2002.

[43] D. H. Lee, S. Y. Won, Y. T. Kim, and Y. S. Chung. Turbulent heat transfer from a flat surface to a swirling round impinging jet. *International Journal of Heat and Mass Transfer*, 45(1):223–227, 2002.

[44] A. Nozaki, Y. Igarashi, and K. Hishida. Heat transfer mechanism of a swirling impinging jet in a stagnation region. *Heat Transfer–Asian Research*, 32(8):663–673, 2003.

[45] S. Hwang, C. Lee, and H. Cho. Heat transfer and flow structures in axisymmetric impinging jet controlled by vortex pairing. *International Journal of Heat and Fluid Flow*, 22(3):293–300, 2001.

[46] K. Ichimiya. Heat transfer characteristics of an annular turbulent impinging jet with a confined wall measured by thermosensitive liquid crystal. *Heat and Mass Transfer*, 39 (7):545–551, 2003.

[47] X. Yan and N. Saniei. Heat transfer from an obliquely impinging circular, air jet to a flat plate. *International Journal of Heat and Fluid Flow*, 18(6):591–599, 1997.

[48] E. Sparrow and B. Lovell. Heat transfer characteristics of an obliquely impinging circular jet. *Journal of Heat Transfer*, 102(2):202–209, 1980.

[49] C. Ma, Q. Zheng, H. Sun, K. Wu, and K. Horii. Local convective heat transfer from a vertical flat surface to oblique submerged impinging jets of large Prandtl number liquid. *Experimental Thermal and Fluid Science*, 17(3):238–247, July 1998.

[50] A. H. Beitelmal, M. A. Saad, and C. D. Patel. The effect of inclination on the heat transfer between a flat surface and an impinging two-dimensional air jet. *International Journal of Heat and Fluid Flow*, 21(2):156–163, 2000.

[51] A. A. Tawfek. Heat transfer studies of the oblique impingement of round jets upon a curved surface. *Heat and Mass Transfer*, 38(6):467–475, June 2002.

[52] M.-Y. Wen. Flow structures and heat transfer of swirling jet impinging on a flat surface with micro-vibrations. *International Journal of Heat and Mass Transfer*, 48(3):545–560, 2005.

[53] G. Bart, A. Van Ijzerloo, L. Geers, L. Hoek, and K. Hanjalić. Heat transfer of phase-locked modulated impinging-jet arrays. *Experimental Thermal and Fluid Science*, 26 (2):299–304, 2002.

[54] M. Taslim, L. Setayeshgar, and S. Spring. An experimental evaluation of advanced leading edge impingement cooling concepts. *Journal of Turbomachinery*, 123(1):147–153, 2001.

[55] C. Gau and C. Lee. Impingement cooling flow structure and heat transfer along rib-roughened walls. *International Journal of Heat and Mass Transfer*, 35(11):3009–3020, 1992.

[56] H. A. El-Sheikh and S. Garimella. Enhancement of air jet impingement heat transfer using pin-fin heat sinks. *Components and Packaging Technologies, IEEE Transactions on*, 23(2):300–308, 2000.

[57] J. S. Issa and A. Ortega. Experimental measurements of the flow and heat transfer of a square jet impinging on an array of square pin fins. *Journal of Electronic Packaging*, 128(1):61–70, 2006.

[58] Y.-H. Liu, S.-J. Song, and Y.-H. Lo. Jet impingement heat transfer on target surfaces with longitudinal and transverse grooves. *International Journal of Heat and Mass Transfer*, 58(1-2):292–299, March 2013.

[59] S. Ndao, H. J. Lee, Y. Peles, and M. K. Jensen. Heat transfer enhancement from micro pin fins subjected to an impinging jet. *International Journal of Heat and Mass Transfer*, 55(1-3):413–421, January 2012.

[60] S. Narumanchi, M. Mihalic, G. Moreno, and K. Bennion. Design of light-weight, single-phase liquid-cooled heat exchanger for power electronics. In *the 13th Intersociety Conference on Thermal and Thermomechanical Phenomena in Electric Systems (ITHERM)*, pages 693–699. IEEE, 2012.

[61] D.-H. Rhee, P.-H. Yoon, and H. H. Cho. Local heat/mass transfer and flow characteristics of array impinging jets with effusion holes ejecting spent air. *International Journal of Heat and Mass Transfer*, 46(6):1049–1061, 2003.

[62] T. Brunschwiler, H. Rothuizen, M. Fabbri, U. Kloter, B. Michel, R. Bezama, and G. Natarajan. Direct liquid jet-impingment cooling with micron-sized nozzle array and distributed return architecture. In *the 10th Intersociety Conference on Thermal and Thermomechanical Phenomena in Electronics Systems (ITHERM)*, pages 196–203. IEEE, 2006.

[63] A. J. Onstad, C. J. Elkins, R. J. Moffat, and J. K. Eaton. Full-field flow measurements and heat transfer of a compact jet impingement array with local extraction of spent fluid. *Journal of Heat Transfer*, 131(8):082201, 2009.

[64] Y. Zhuang, C. Ma, and M. Qin. Experimental study on local heat transfer with liquid impingement flow in two-dimensional micro-channels. *International Journal of Heat and Mass Transfer*, 40(17):4055–4059, 1997.

[65] M. B. Dogruoz, A. Ortega, and R. V. Westphal. Measurements of skin friction and heat transfer beneath an impinging slot jet. *Experimental Thermal and Fluid Science*, 60: 213–222, 2015.

[66] S. Ashforth-Frost, K. Jambunathan, and C. Whitney. Velocity and turbulence characteristics of a semiconfined orthogonally impinging slot jet. *Experimental Thermal and Fluid Science*, 14(1):60–67, 1997.

[67] T. Chan, C. Leung, K. Jambunathan, S. Ashforth-Frost, Y. Zhou, and M. Liu. Heat transfer characteristics of a slot jet impinging on a semi-circular convex surface. *International Journal of Heat and Mass Transfer*, 45(5):993–1006, 2002.

[68] D. Colucci and R. Viskanta. Effect of nozzle geometry on local convective heat transfer to a confined impinging air jet. *Experimental Thermal and Fluid Science*, 13(1):71–80, 1996.

[69] R. Wiberg and N. Lior. Errors in thermochromic liquid crystal thermometry. *Review of Scientific Instruments*, 75(9):2985–2994, 2004.

[70] S. Kang and R. Greif. Flow and heat transfer to a circular cylinder with a hot impinging air jet. *International Journal of Heat and Mass Transfer*, 35(9):2173–2183, 1992.

[71] S. Polat, B. Huang, A. S. Mujumdar, and W. Douglas. Numerical flow and heat transfer under impinging jets: a review. *Annual Review of Heat Transfer*, 2(2), 1989.

[72] F. Beaubert and S. Viazzo. Large eddy simulation of a plane impinging jet. *Comptes Rendus Mécanique*, 330(12):803–810, 2002.

[73] T. Hävist and L. Fuchs. Numerical study of swirling impinging jets with heat transfer. In *ASME 2004 Heat Transfer/Fluids Engineering Summer Conference*, pages 965–975. American Society of Mechanical Engineers, 2004.

[74] M. Olsson and L. Fuchs. Large eddy simulations of a forced semiconfined circular impinging jet. *Physics of Fluids*, 10(2):476–486, 1998.

[75] T. Cziesla, G. Biswas, H. Chattopadhyay, and N. Mitra. Large-eddy simulation of flow and heat transfer in an impinging slot jet. *International Journal of Heat and Fluid Flow*, 22(5):500–508, 2001.

[76] T. Craft, L. Graham, and B. E. Launder. Impinging jet studies for turbulence model assessmentii. an examination of the performance of four turbulence models. *International Journal of Heat and Mass Transfer*, 36(10):2685–2697, 1993.

[77] M. Bouainouche, N. Bourabaa, and B. Desmet. Numerical study of the wall shear stress produced by the impingement of a plane turbulent jet on a plate. *International Journal of Numerical Methods for Heat & Fluid Flow*, 7(6):548–564, 1997.

[78] T. Esch and F. Menter. Heat transfer predictions based on two-equation turbulence models with advanced wall treatment. *Turbulence, Heat and Mass Transfer*, 4:633–640, 2003.

[79] K. Heyerichs and A. Pollard. Heat transfer in separated and impinging turbulent flows. *International Journal of Heat and Mass Transfer*, 39(12):2385–2400, 1996.

[80] T. Craft, B. Launder, and K. Suga. Development and application of a cubic eddy-viscosity model of turbulence. *International Journal of Heat and Fluid Flow*, 17(2): 108–115, 1996.

[81] E. Turgeon and D. Pelletier. Verification and validation of adaptive finite element method for impingement heat transfer. *Journal of Thermophysics and Heat Transfer*, 15(3):284–292, 2001.

[82] B. Merci, J. Vierendeels, C. De Langhe, and E. Dick. Numerical simulation of heat transfer of turbulent impinging jets with two-equation turbulence models. *International Journal of Numerical Methods for Heat & Fluid Flow*, 13(1):110–132, 2003.

[83] N. Souris, H. Liakos, M. Founti, and N. Markatos. Study of impinging turbulent jet flows using the isotropic low-reynolds number and the algebraic stress methods. *Computational Mechanics*, 28(5):381–389, 2002.

[84] P. Tzeng, C. Soong, and C. Hsieh. Numerical investigation of heat transfer under confined impinging turbulent slot jets. *Numerical Heat Transfer: Part A: Applications*, 35(8):903–924, 1999.

[85] U. Heck, U. Fritsching, and K. Bauckhage. Fluid flow and heat transfer in gas jet quenching of a cylinder. *International Journal of Numerical Methods for Heat & Fluid Flow*, 11(1):36–49, 2001.

[86] T. Park, H. Choi, J. Yoo, and S. Kim. Streamline upwind numerical simulation of two-dimensional confined impinging slot jets. *International Journal of Heat and Mass Transfer*, 46(2):251–262, 2003.

[87] T.-H. Shih, W. W. Liou, A. Shabbir, Z. Yang, and J. Zhu. A new k-ϵ eddy viscosity model for high reynolds number turbulent flows. *Computers & Fluids*, 24(3):227–238, 1995.

[88] A. Abdon and B. Sundén. Numerical investigation of impingement heat transfer using linear and nonlinear two-equation turbulence models. *Numerical Heat Transfer: Part A: Applications*, 40(6):563–578, 2001.

[89] T. S. Park and H. J. Sung. Development of a near-wall turbulence model and application to jet impingement heat transfer. *International Journal of Heat and Fluid Flow*, 22(1): 10–18, 2001.

[90] K. Funazaki and K. Hachiya. Systematic numerical studies on heat transfer and aerodynamic characteristics of impingement cooling devices combined with pins. In *ASME Turbo Expo*, pages 16–19, 2003.

[91] Y. Shi, M. Ray, and A. Mujumdar. Computational study of impingement heat transfer under a turbulent slot jet. *Industrial & Engineering Chemistry Research*, 41(18):4643–4651, 2002.

[92] P. A. Durbin. Separated flow computations with the k-ε-v^2 model. *AIAA Journal*, 33 (4):659–664, 1995.

[93] M. Behnia, S. Parneix, and P. A. Durbin. Prediction of heat transfer in an axisymmetric turbulent jet impinging on a flat plate. *International Journal of Heat and Mass Transfer*, 41(12):1845–1855, 1998.

[94] L. Thielen, H. Jonker, and K. Hanjalić. Symmetry breaking of flow and heat transfer in multiple impinging jets. *International Journal of Heat and Fluid Flow*, 24(4):444–453, 2003.

[95] *ANSYS Fluent V2F Turbulence Model Manual.* ANSYS, Inc., Canonsburg, PA, 15.0 edition, 2013.

[96] F. R. Menter. Zonal two equation k-ω turbulence models for aerodynamic flows. In *the 24th Fluid Dynamics Conference*, volume 93-2906, 1993.

[97] *ANSYS® Academic Research, Release 14.5.7, Help System.* ANSYS, Inc., Canonsburg, PA.

[98] F. R. Menter, R. B. Langtry, S. R. Likki, Y. B. Suzen, P. G. Huang, and S. Völker. A correlation-based transition model using local variable—part I: model formulation. *Journal of Turbomachinery*, 128(3):413–422, 2006.

[99] R. J. Moffat. Describing the uncertainties in experimental results. *Experimental Thermal and Fluid Science*, 1(1):3–17, 1988.

Appendices

Appendix A

Mechanical Drawings

The mechanical drawing used to fabricate the flow chamber, the heater block, and the measurement block are presented on the following pages.

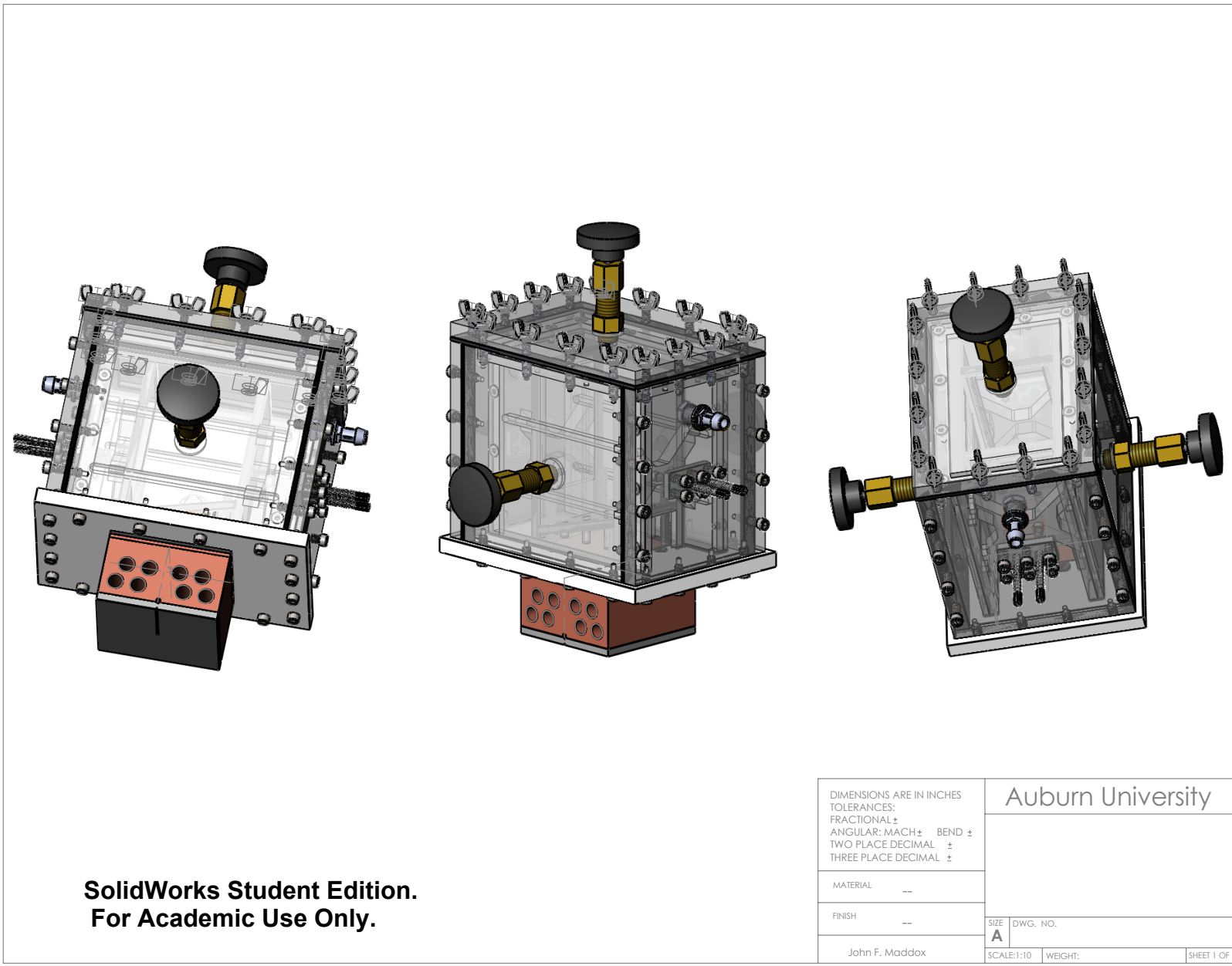

Figure A.1: Assembled flow chamber

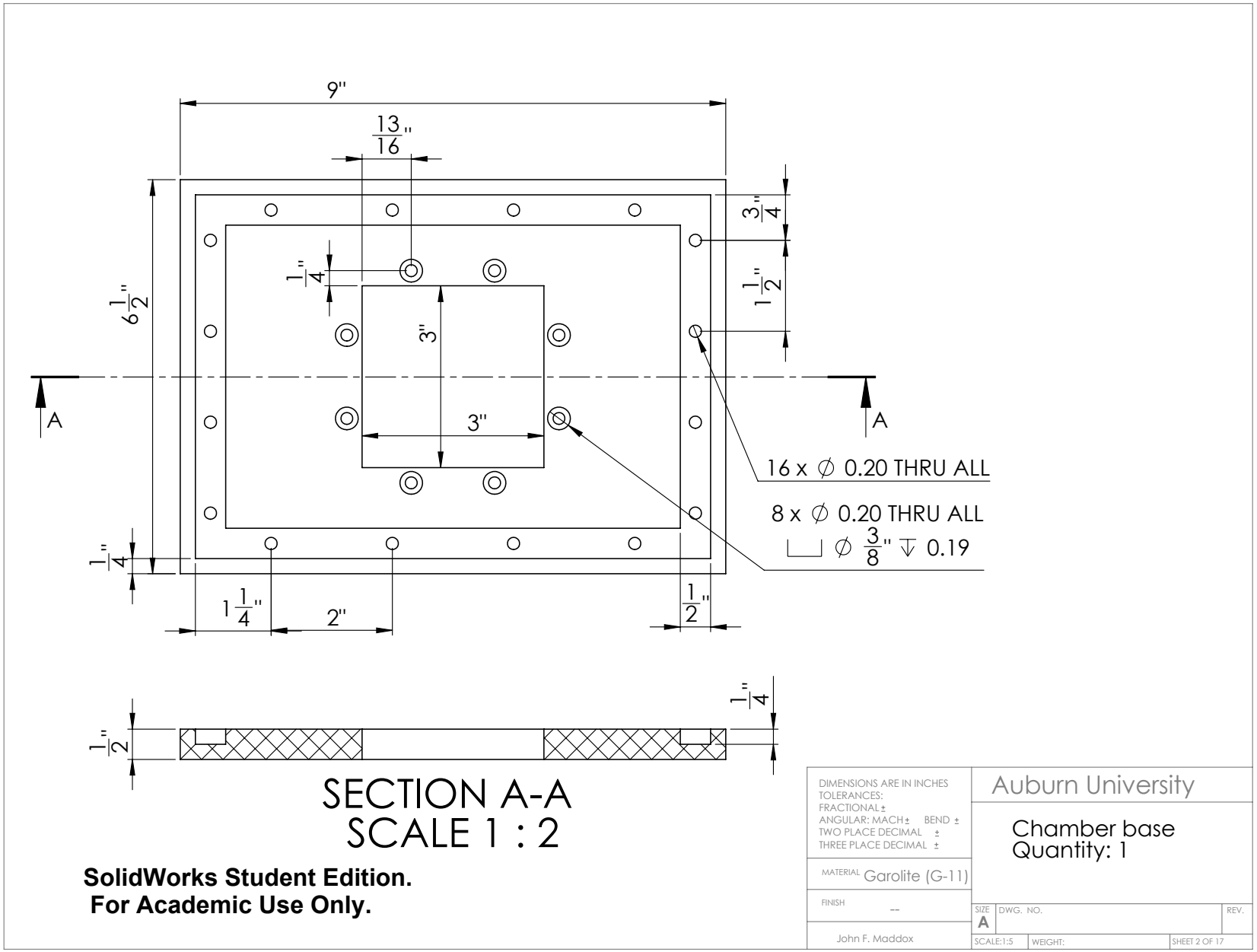

Figure A.2: Garolite flow chamber base plate

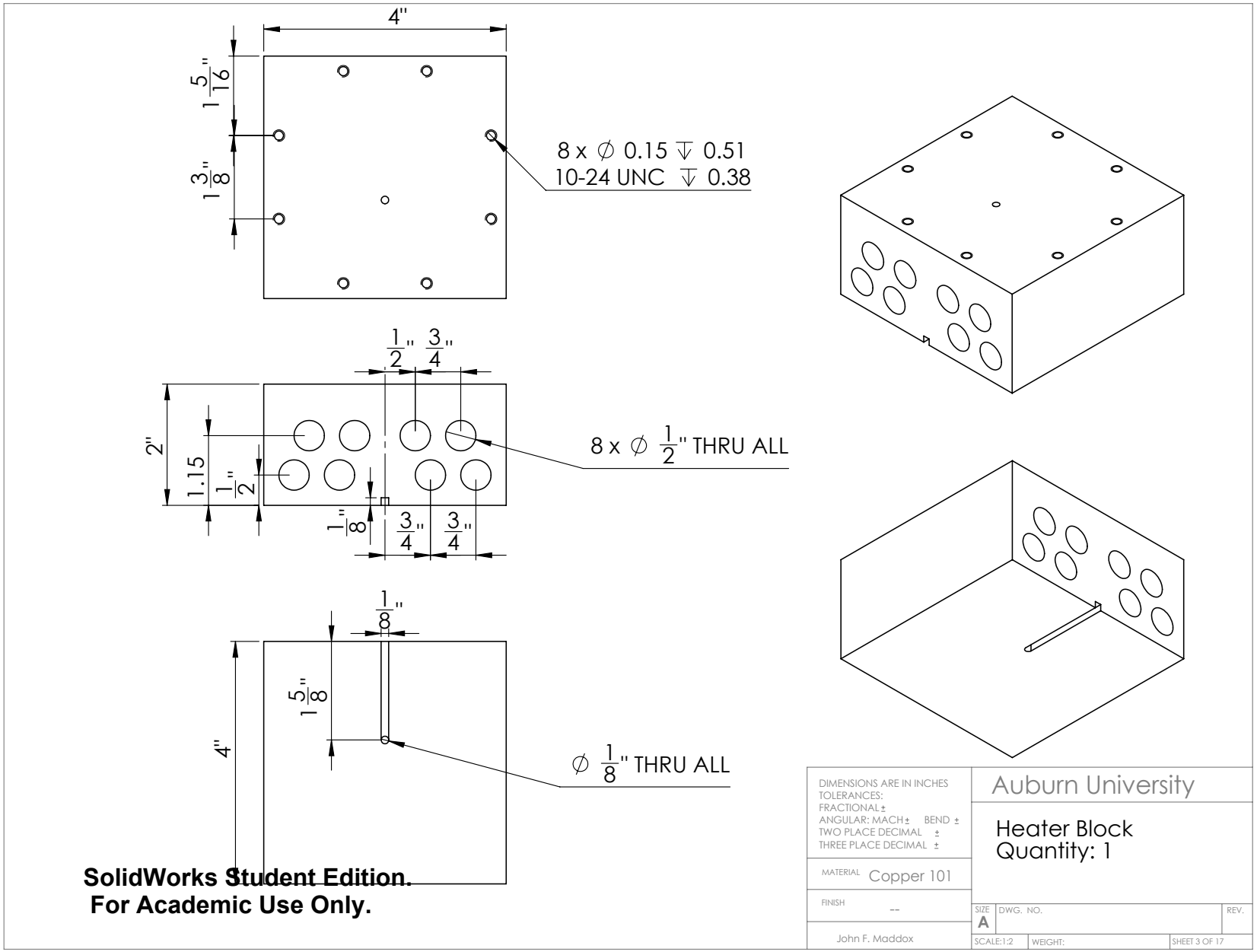

Figure A.3: Copper heater block

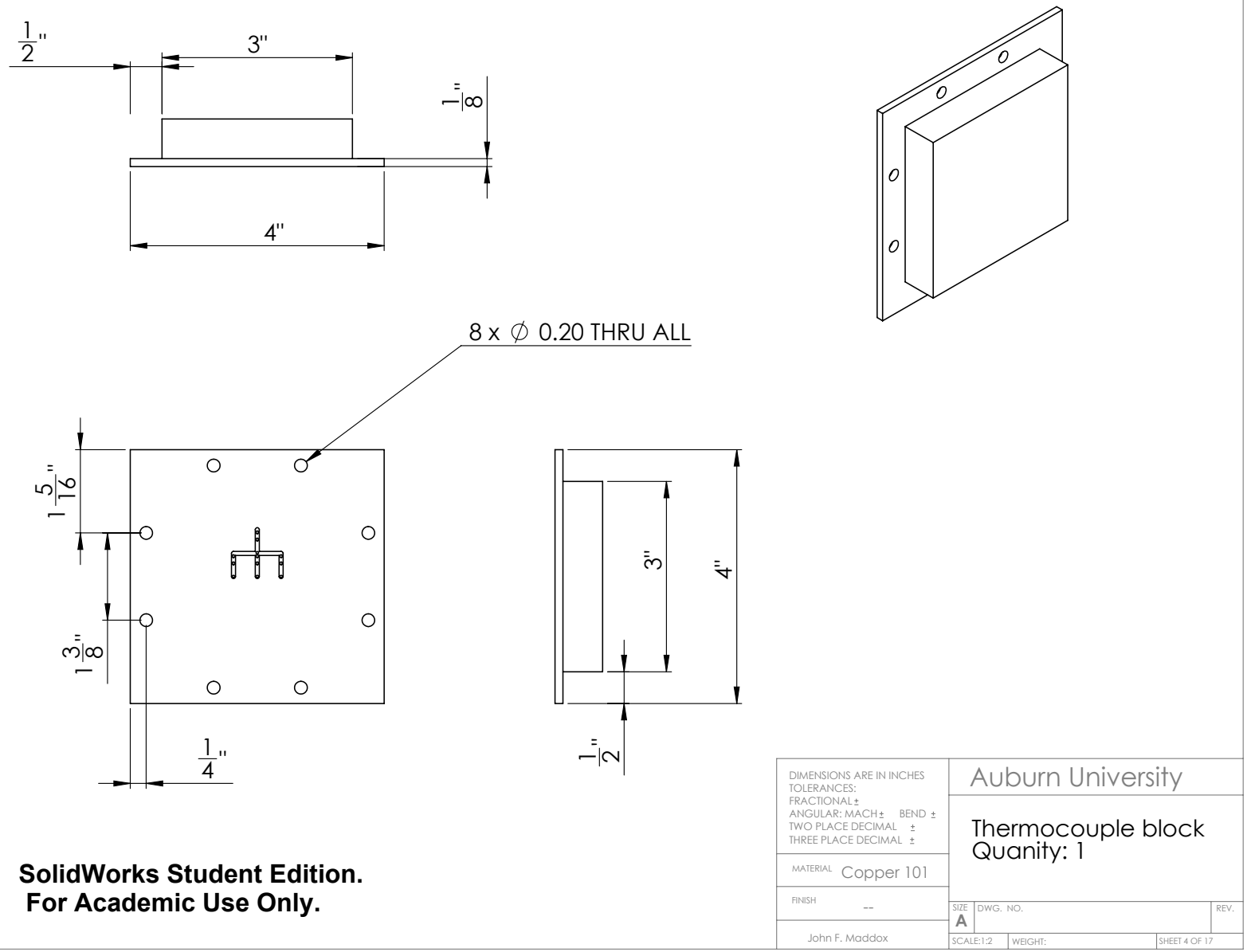

Figure A.4: Copper measurement block

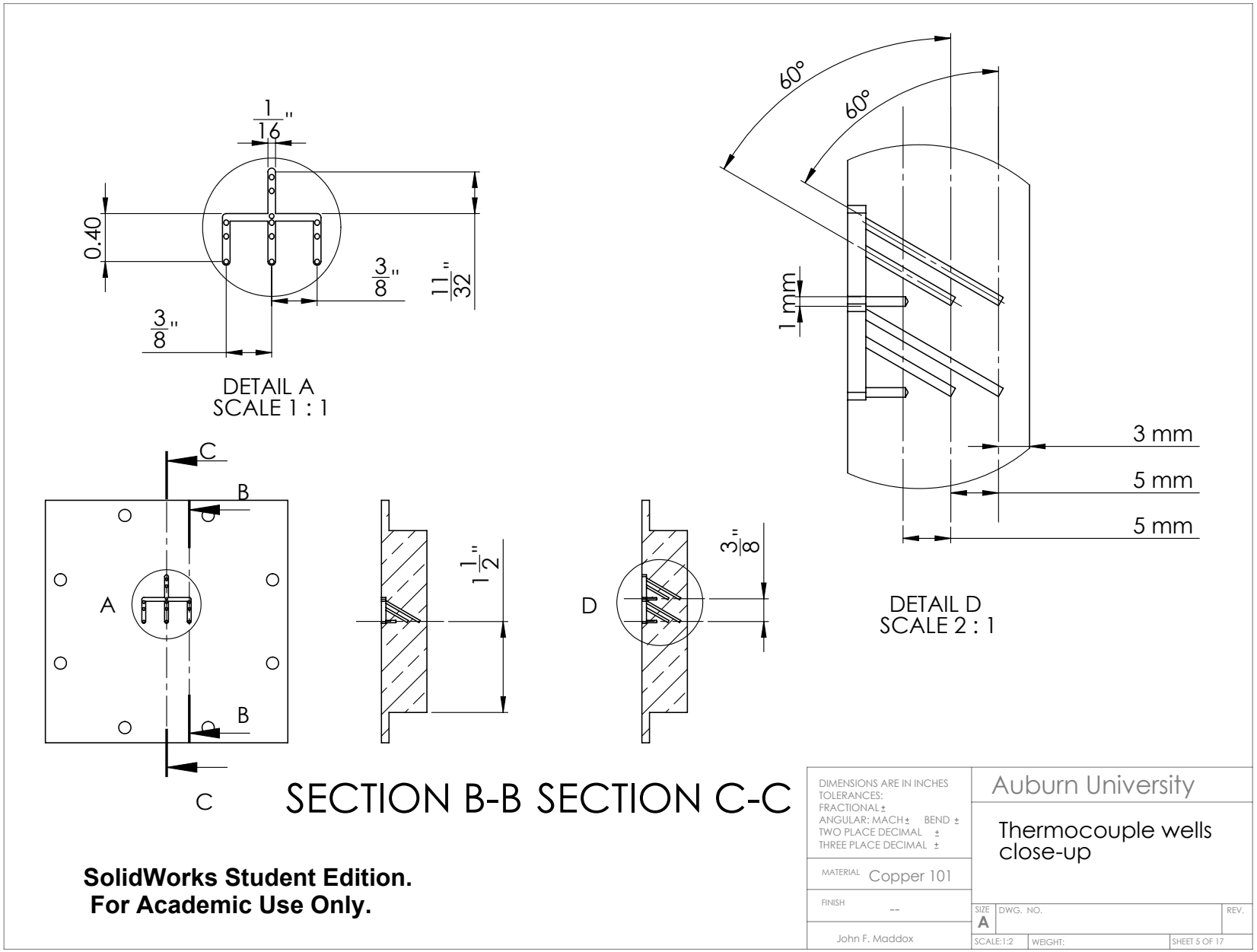

Figure A.5: Detailed view of thermocouple wells in copper measurement block

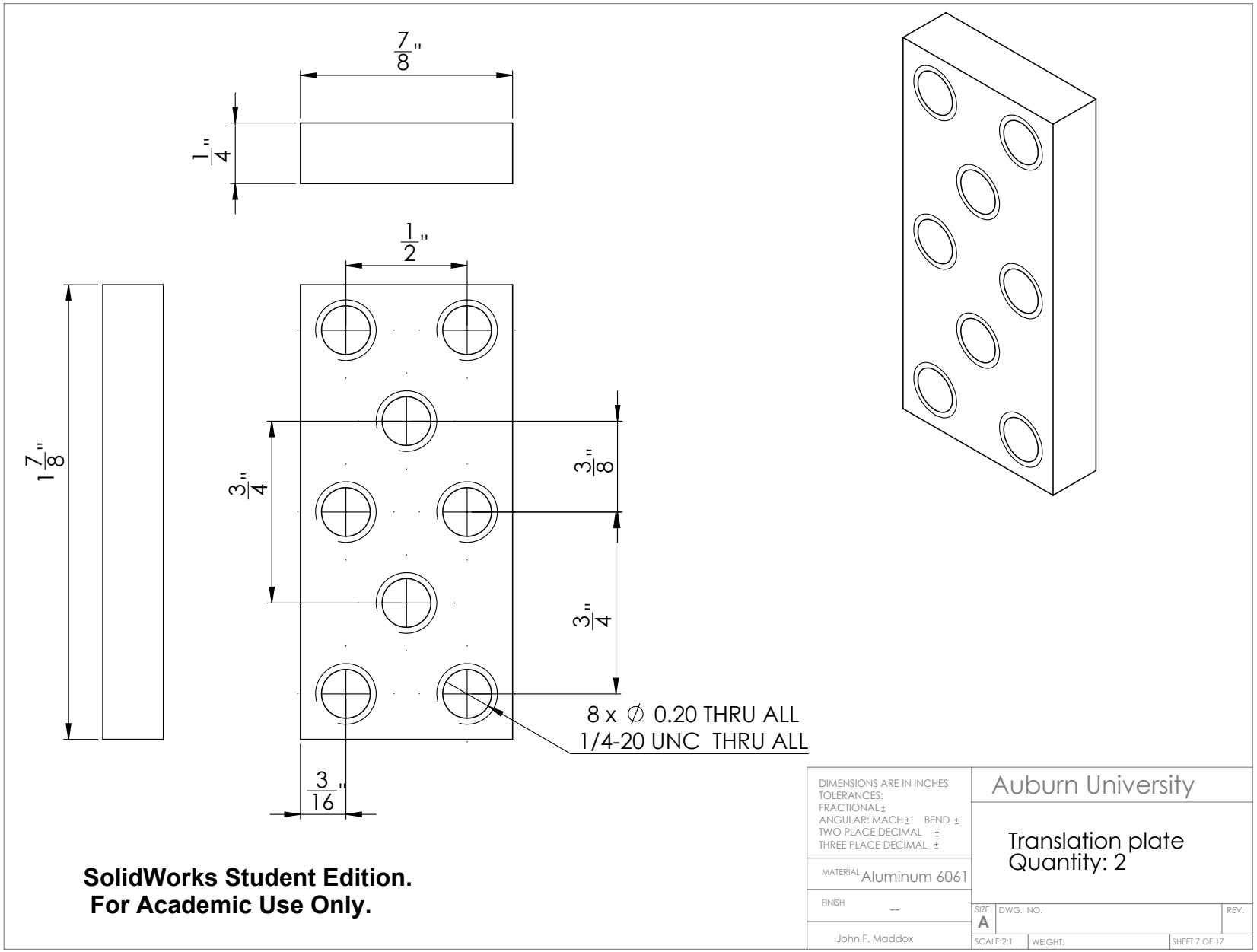

Figure A.6: Aluminum translation plate

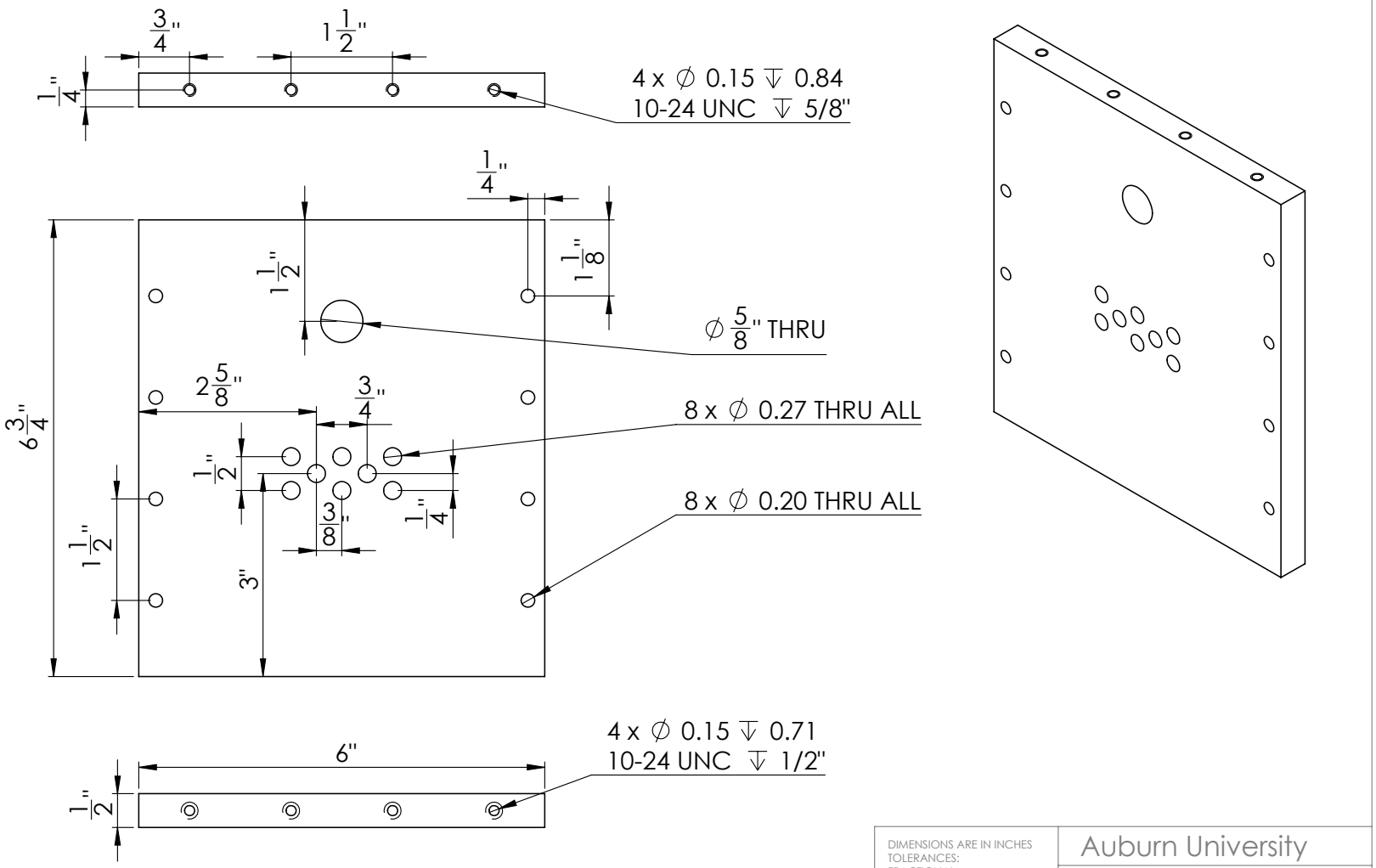

Figure A.7: Lexan flow chamber end wall

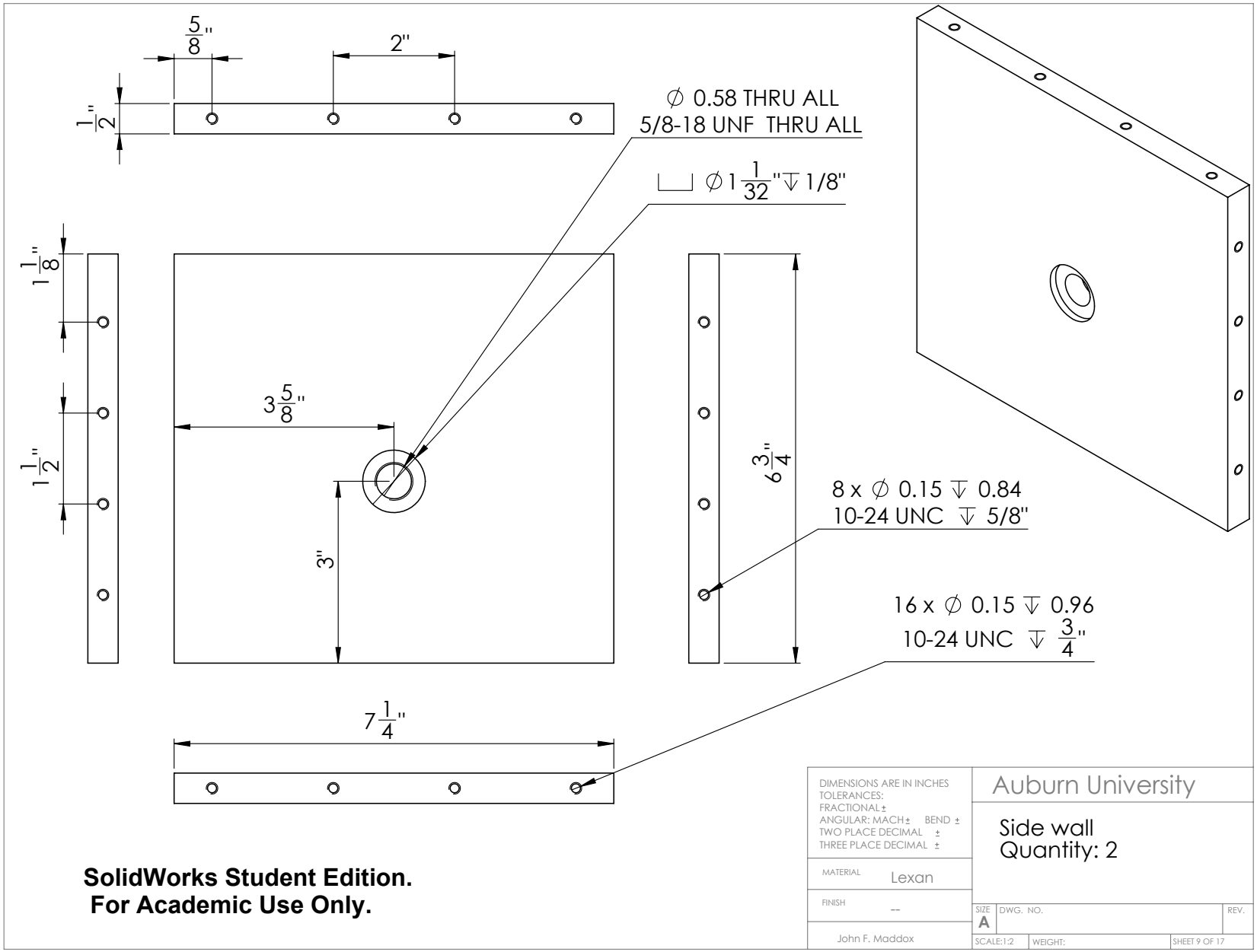

Figure A.8: Lexan flow chamber exterior side wall

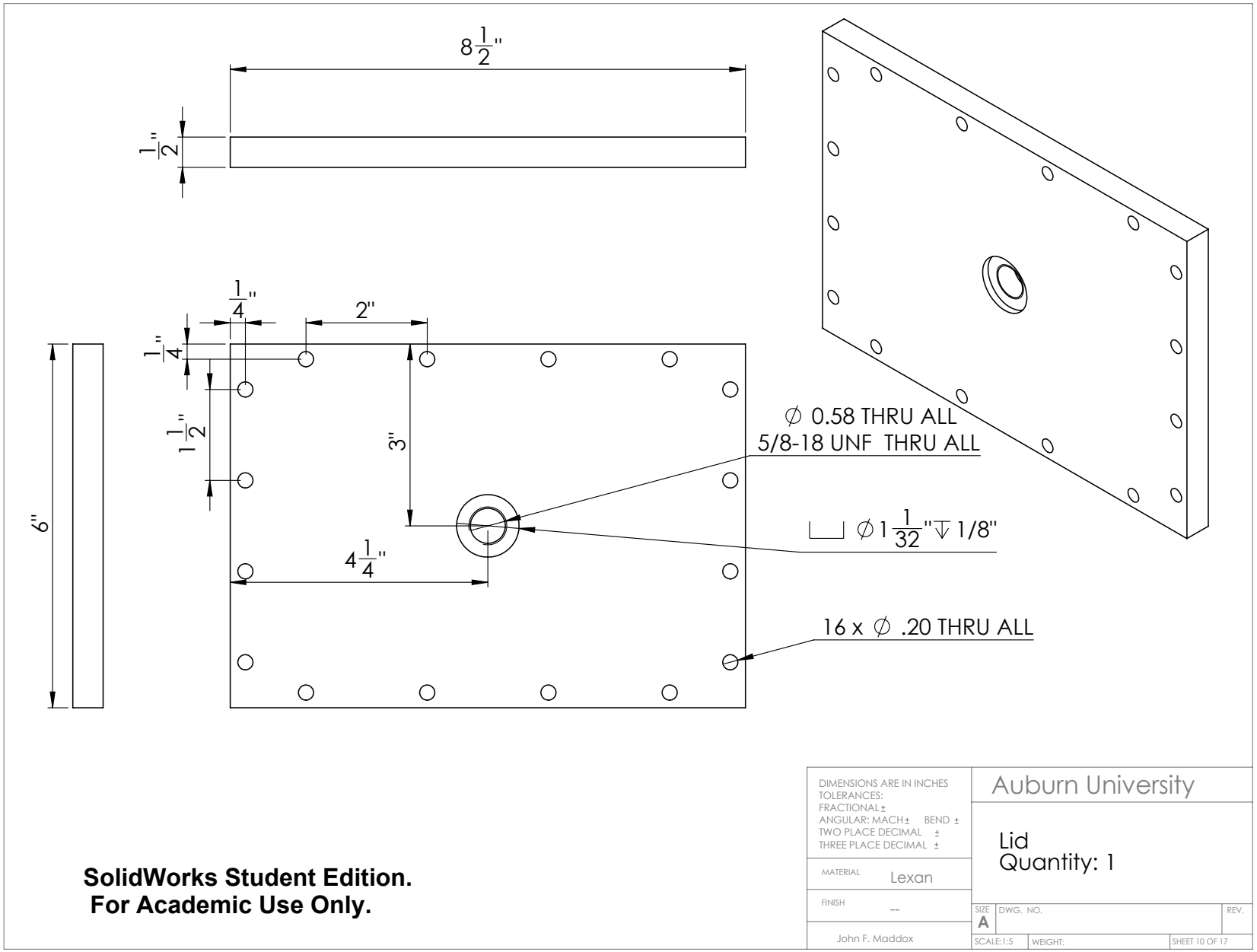

Figure A.9: Lexan flow chamber lid

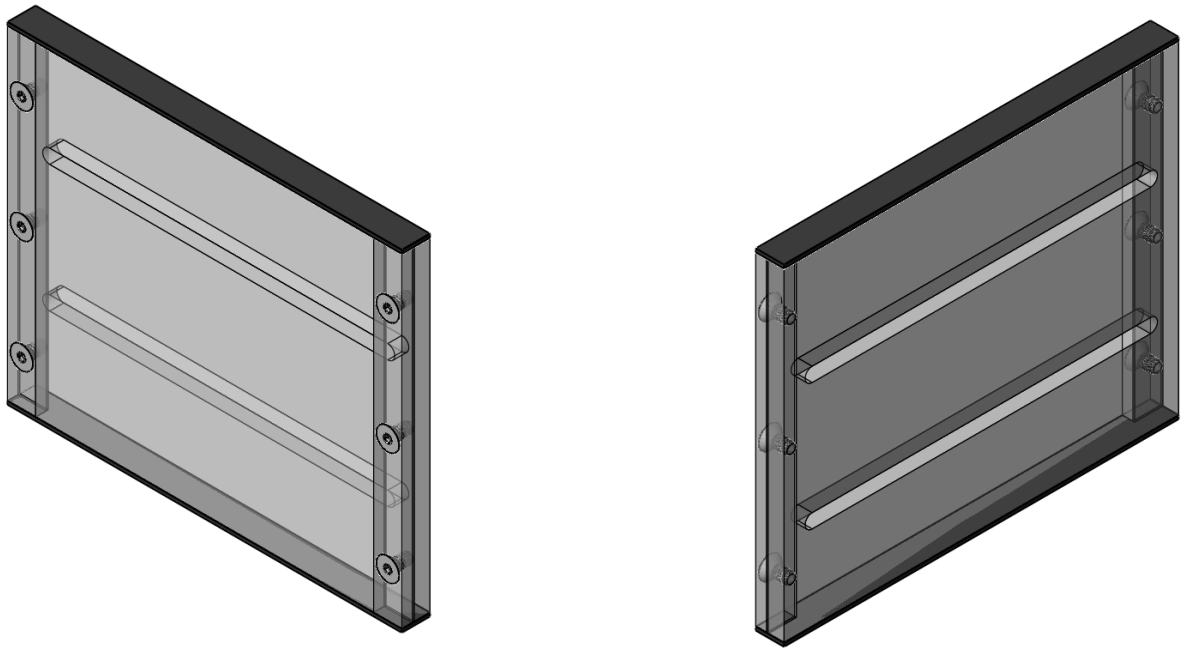

SolidWorks Student Edition.
For Academic Use Only.

DIMENSIONS ARE IN INCHES TOLERANCES: FRACTIONAL ± ANGULAR: MACH ± BEND ± TWO PLACE DECIMAL ± THREE PLACE DECIMAL ±	Auburn University
MATERIAL --	
FINISH --	SIZE A / DWG. NO. / REV.
John F. Maddox	SCALE:1:2 / WEIGHT: / SHEET 11 OF 17

Figure A.10: Assembled interior side wall

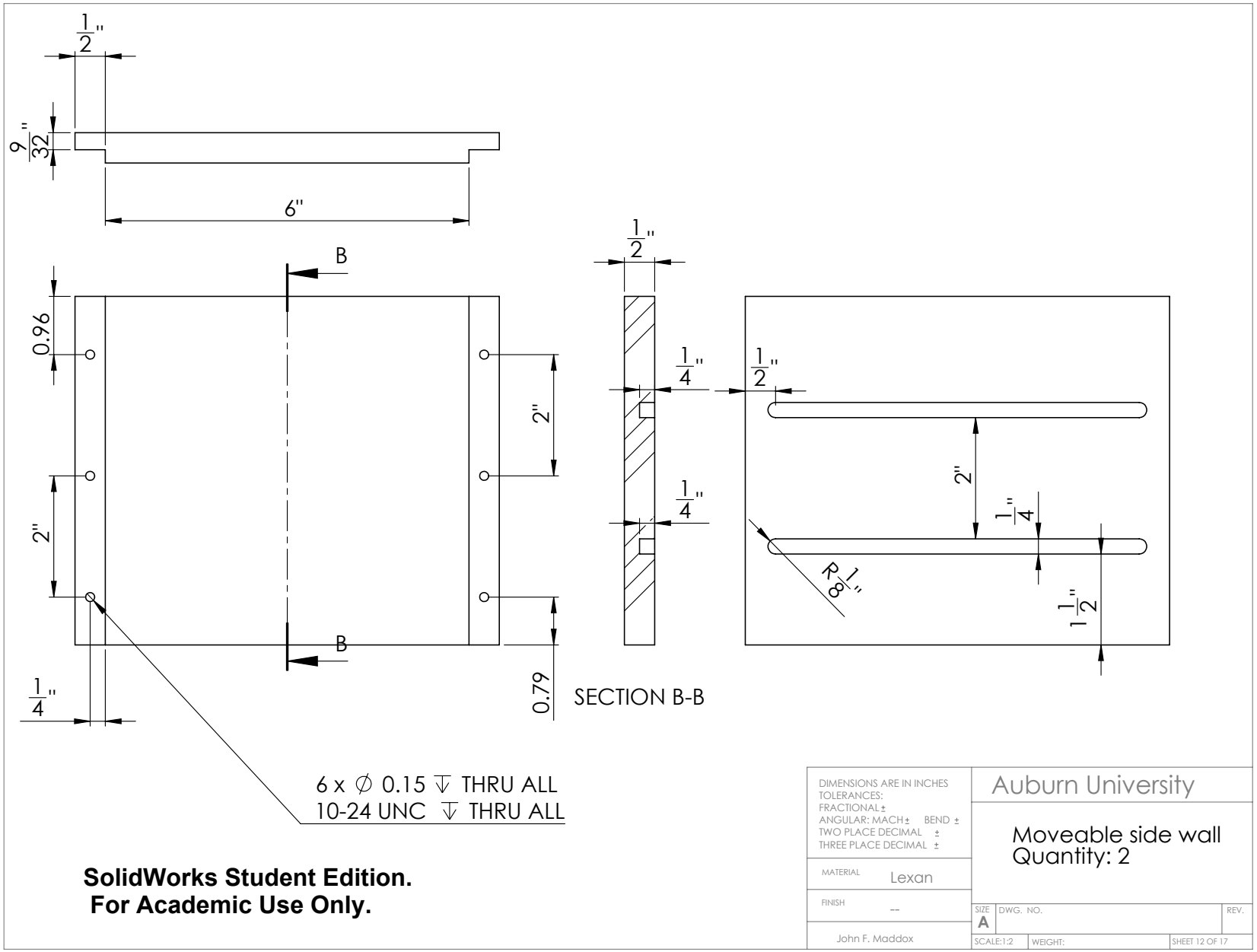

Figure A.11: Lexan interior side wall

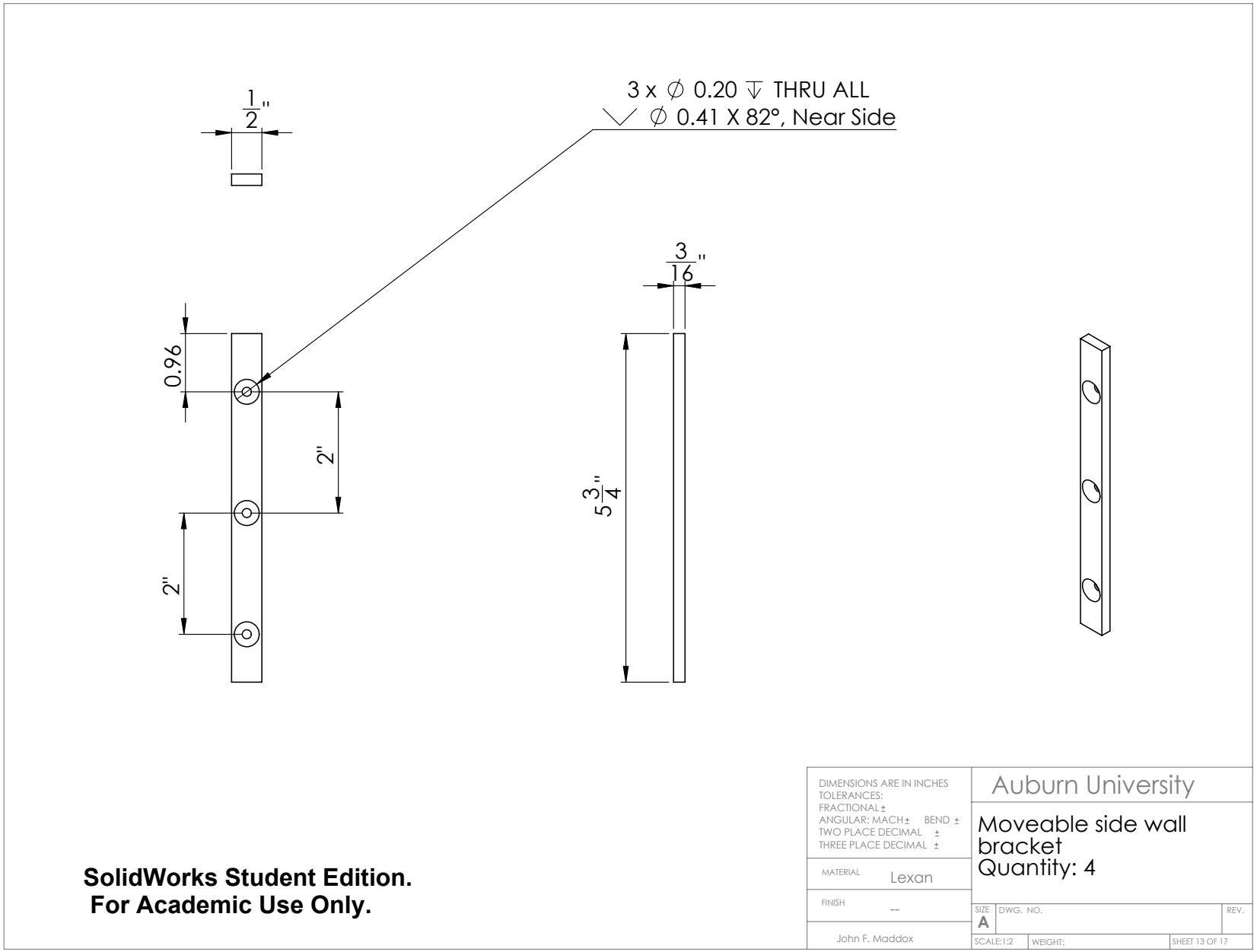

Figure A.12: Lexan interior side wall bracket

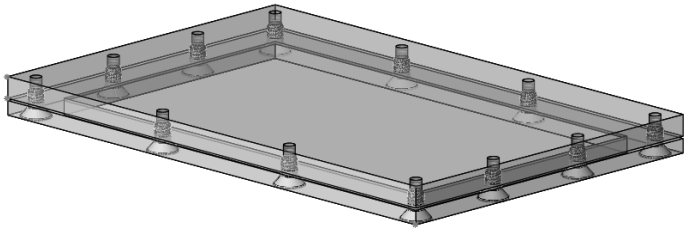

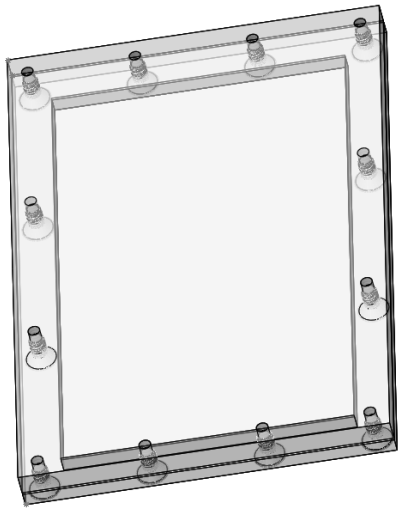

DIMENSIONS ARE IN INCHES TOLERANCES: FRACTIONAL ± ANGULAR: MACH ± BEND ± TWO PLACE DECIMAL ± THREE PLACE DECIMAL ±	Auburn University
MATERIAL --	
FINISH --	SIZE A | DWG. NO. | REV.
John F. Maddox	SCALE:1:2 | WEIGHT: | SHEET 14 OF 17

Figure A.13: Assembled interior top wall

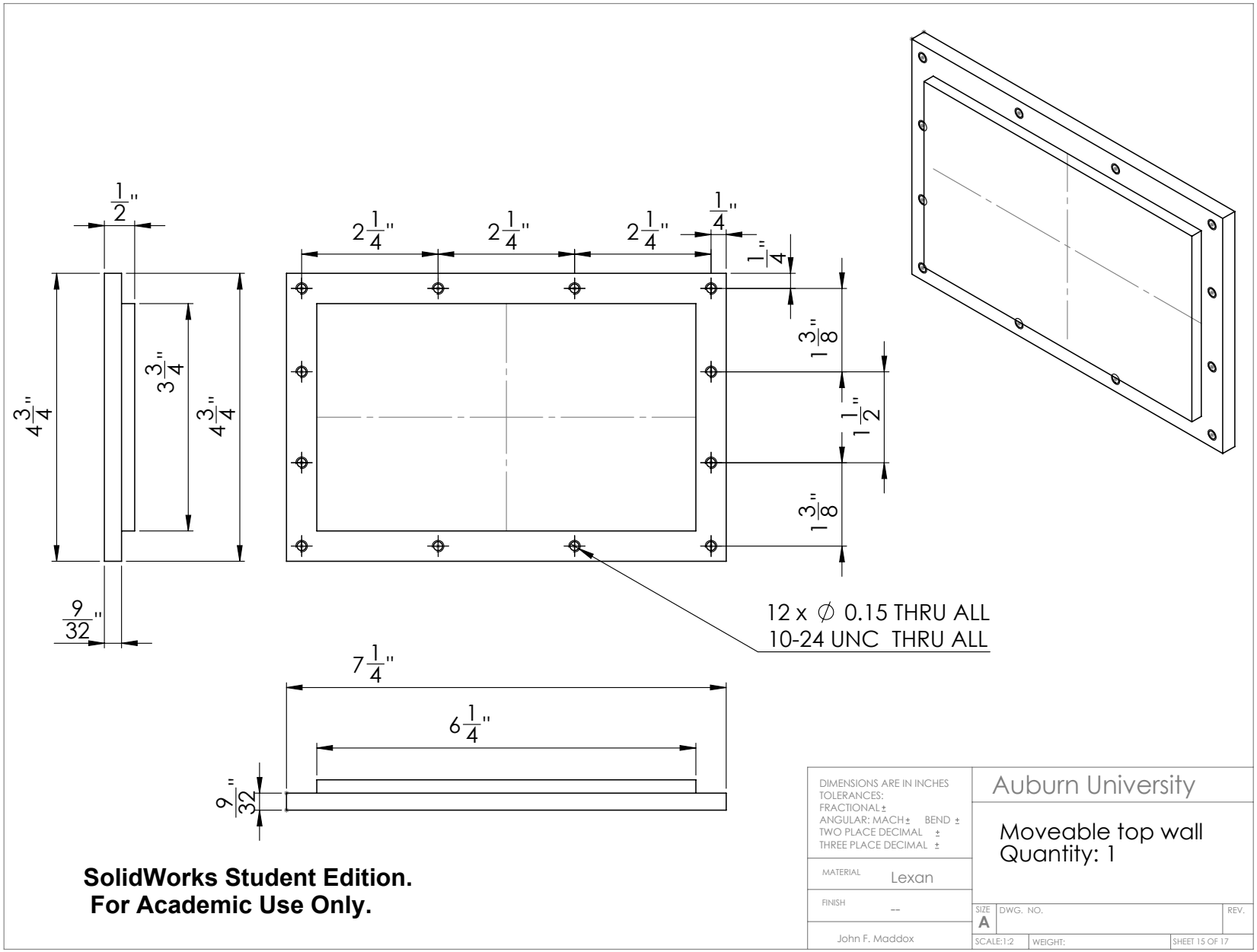

Figure A.14: Lexan interior top wall

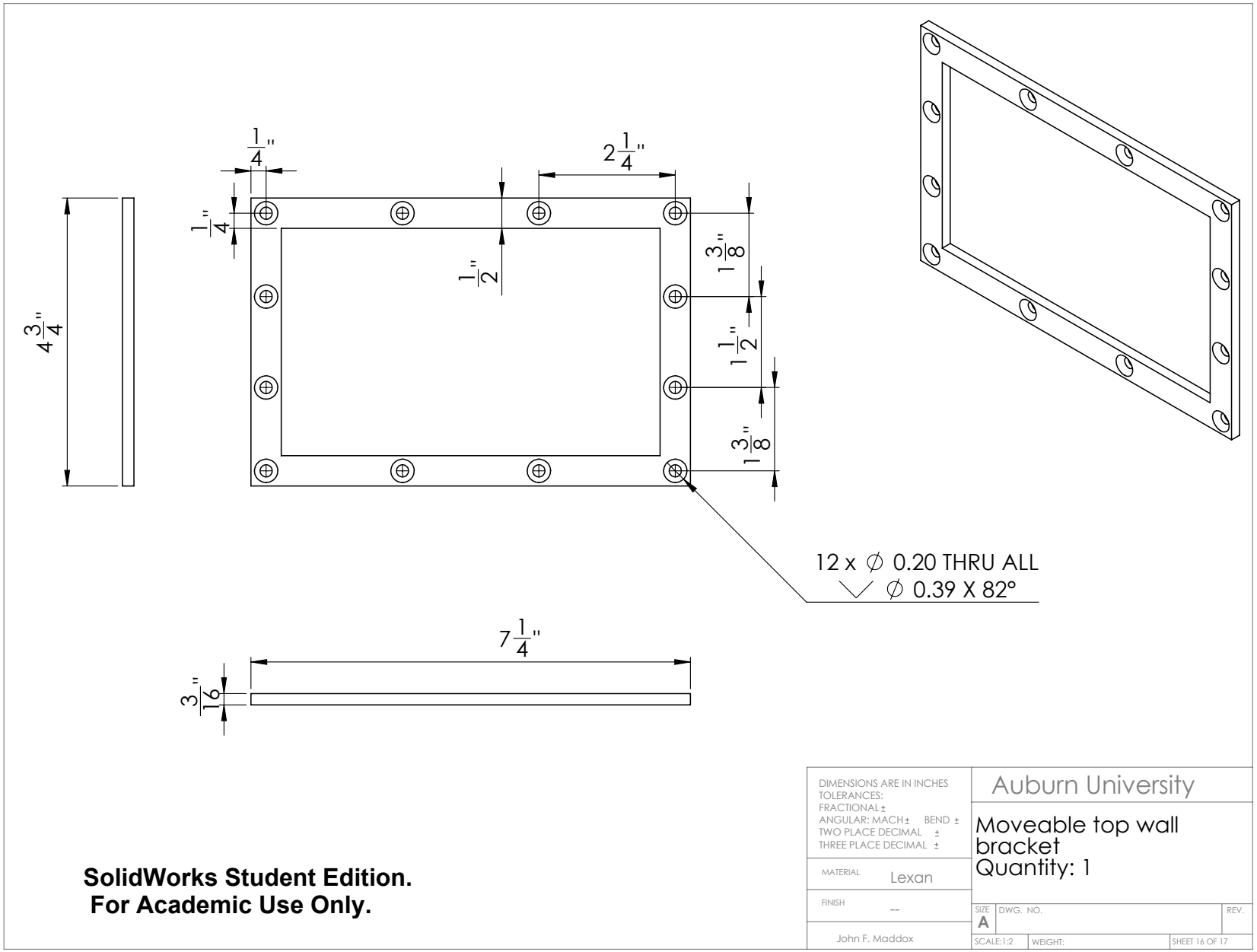

Figure A.15: Lexan interior top wall bracket

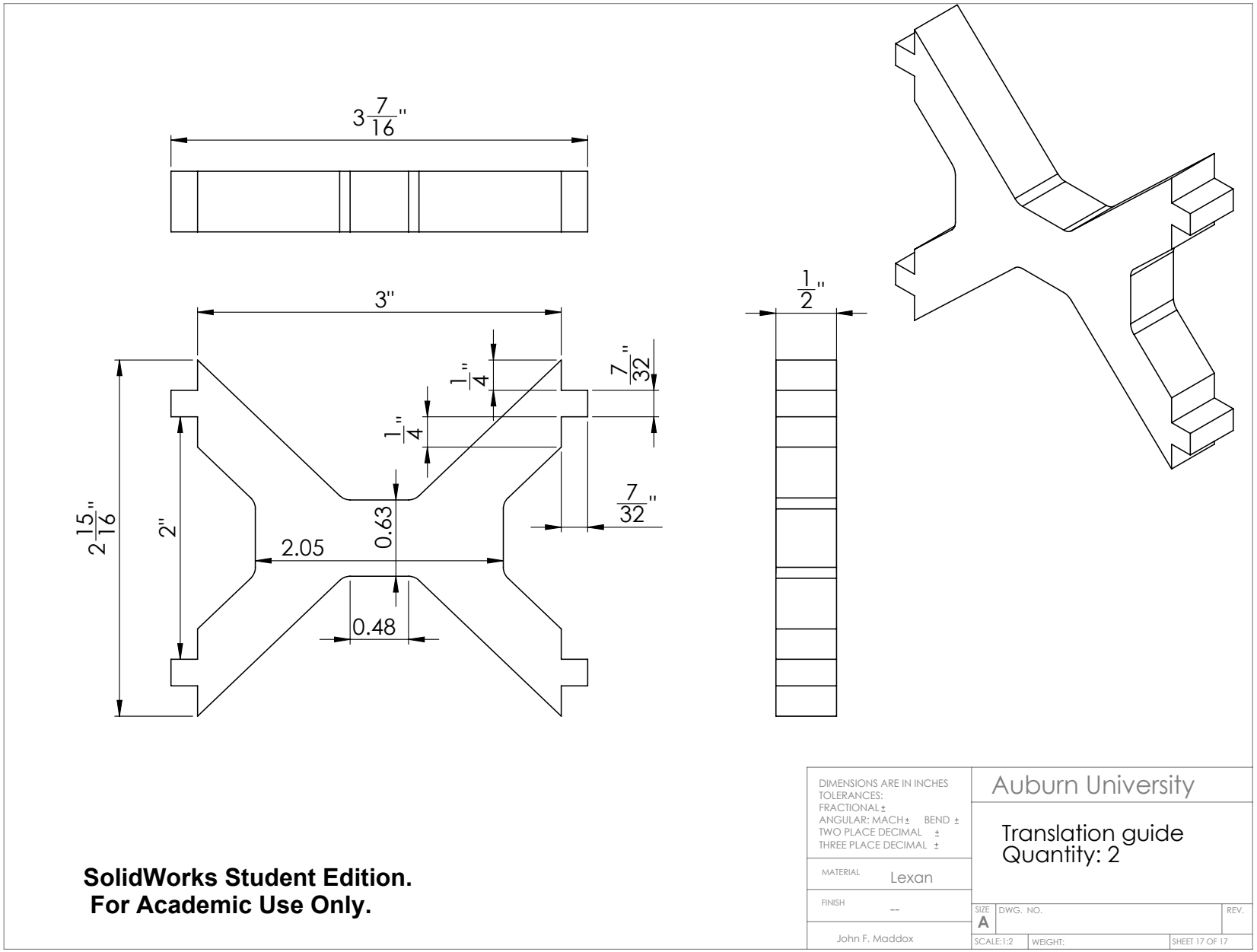

Figure A.16: Lexan translation guide

Appendix B

Data Acquisition

B.1 Procedure

In order for the system to perform as intended the steps for assembling and adjusting the flow chamber need to be performed in a particular order.

B.1.1 Opening the Flow Chamber

1. close the valve beneath the liquid reservoir to prevent the chamber from over flowing when it is opened
2. loosen the top needle valve to relieve the pressure from the lid
3. loosen one of the x-direction needle valves by six turns to relieve the pressure from the wall studs against the holes in the lid (keep track of which side was loosened)
4. loosen all the wing nuts on the top of the tank by half a turn to relieve the tension
5. finish unscrewing and remove all the wing nuts from the top of the tank
6. tighten the top needle valve to separate the lid from the gasket along the walls (if only one side lifts off of the gasket, it may be necessary to push down on the side that side to force the other side to lift separate as well)
7. remove the lid from the tank and set aside
8. tighten the x-direction needle valve, that was loosened in step 2, back to its original location (six turns) to relieve the pressure from the walls of the tank on the interior top wall

9. gently peel the rubber gasket apron from the wall of the chamber

10. use the rubber gasket to pull the top wall out of the chamber and set aside

B.1.2 Closing the Flow Chamber

1. ensure that the x-direction needle valves are tightened (this pushes the side wall apart slightly, allowing room for the interior top wall to be inserted)

2. ensure that the liquid level in the chamber is flush with the top of the interior movable side wall

3. place the interior top wall into the chamber and align the gasket with the studs extending from the exterior walls of the chamber

4. loosen one the x-direction needle valves by six turns

5. loosen the needle valve on the lid

6. place the lid onto the chamber

7. replace all the wing nuts and tighten them gradually until all are snug

8. tighten the x-direction needle valve that was loosened in step 4 back to its original location

9. tighten the lid needle valve until it is snug

B.1.3 Replacing the Jet Plate

1. open the chamber following the steps in B.1.1

2. loosen one of the x-direction needle valves by six turns

3. loosen the y-direction translation screws on one side by three turns

4. remove the plenum wall on the downstream side of the chamber
5. remove the old jet plate from the chamber
6. place the new jet plate into the chamber (initially insert it at 90° from the intended orientation to prevent air bubbles from being trapped beneath the plate)
7. replace the plenum wall on the downstream side of the chamber
8. inspect the plenum wall to ensure that the opening in the plenum wall is the correct size for the plate being tested
9. tighten the y-direction translation screws that were loosened in step 3 back to their original location
10. tighten the x-direction needle valve that was loosened in step 2 back to its original location
11. close the chamber following the steps in B.1.2

B.1.4 Translating in the x-direction

1. loosen the lid needle valve
2. loosen the y-direction translation screws on one side by three turns
3. loosen the x-direction needle valve on the side that the plate will be moving towards (3 full turns of the handle will move the needle 3.175mm (1/8”))
4. tighten the x-direction needle valve on the opposite side to push the inner chamber in the desired direction
5. tighten the y-direction translation screws that were loosened in step 2 back to their original location
6. tighten the lid needle valve until it is snug

B.1.5 Translating in the y-direction

1. loosen the lid needle valve
2. loosen one of the x-direction needle valves by three turns
3. loosen the y-direction translation screws on the side that the plate will be moving towards (2.5 turns of the screw will move the tip by 3.175mm (1/8"))
4. loosen the y-direction translation screws on one side by three turns
5. tighten the y-direction translation screws on the opposite side to push the inner chamber in the desired direction
6. tighten the x-direction needle valve that were loosened in step 2 back to their original location
7. tighten the lid needle valve until it is snug

B.1.6 Changing the Height of the Jet Plate

1. open the chamber following the steps in B.1.1
2. loosen one of the x-direction needle valves by six turns
3. loosen the y-direction translation screws on one side by three turns
4. turn the four set screws in the jet plate clockwise to raise the plate or counter-clockwise to lower the plate (three full turns with change the elevation by 3.175 mm (1/8"))
5. tighten the y-direction translation screws that were loosened in step 3 back to their original location
6. tighten the x-direction needle valve that was loosened in step 2 back to its original location
7. close the chamber following the steps in B.1.2

B.1.7 Initializing the System

1. turn on the chiller
2. set the chiller to approximately 21°C
3. ensure that the valve beneath the liquid reservoir is open[1]
4. ensure that the pump/VFD is plugged into a 3-phase power outlet
5. flip the "On/Off" toggle switch to "On"
6. flip the "Local/Remote" toggle switch to "Local"
7. turn the pump frequency to the desired value (40–50)
8. point the bypass tube into the liquid reservoir and open its valve to allow the liquid to push the air out of the tube
9. close the bypass tube and elevate it to allow the vapor bubbles to collect in it upstream of the flow chamber
10. let the system run for 10–20 minutes to allow the temperatures to equalize

B.2 Hardware

A diagram of the flow loop and data acquisition hardware is shown in Figure B.1.

[1] since the liquid reservoir is both downstream of and elevated above the flow chamber, the valve beneath the reservoir should be left *open* whenever the pump is on

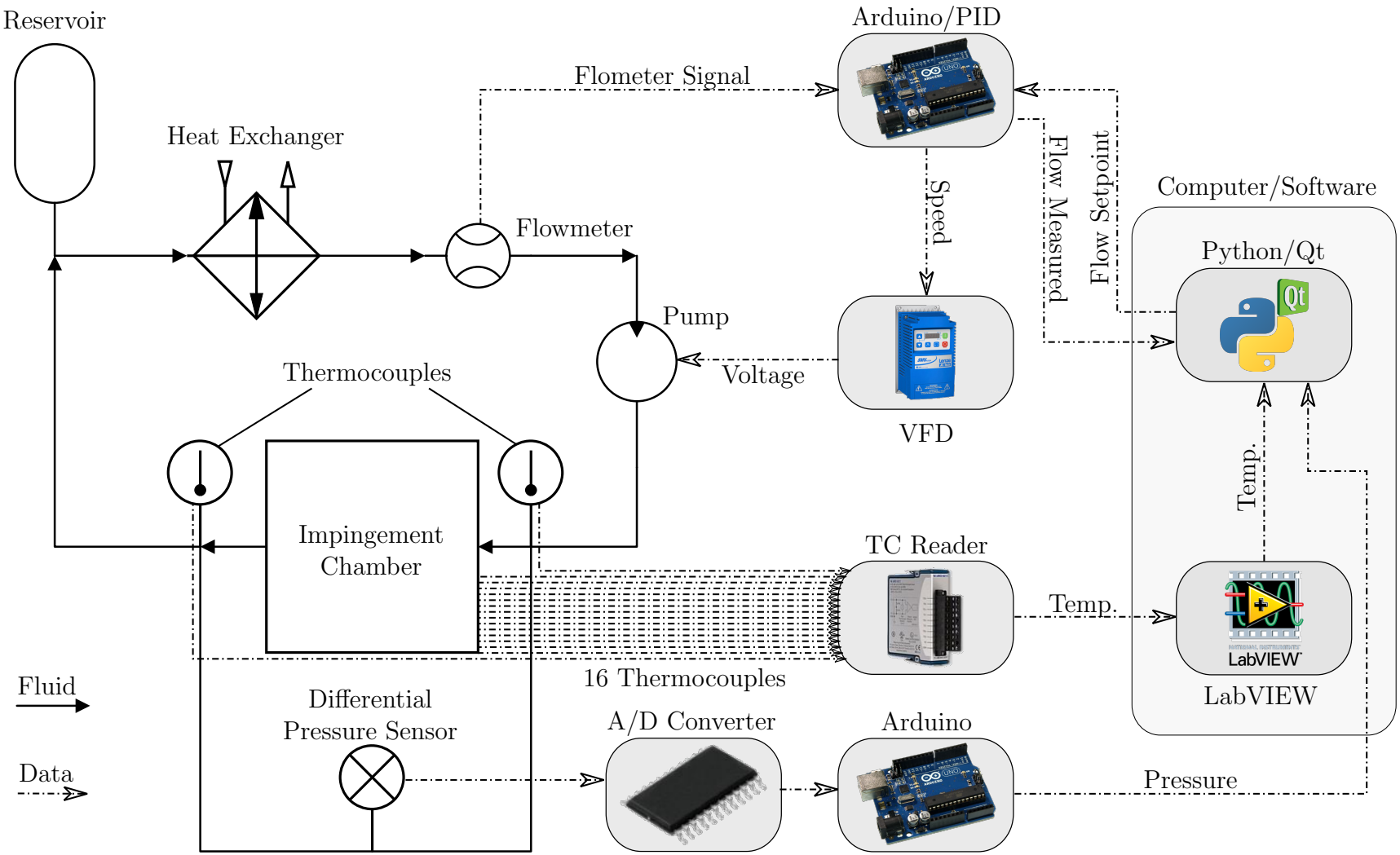

Figure B.1: Data acquisition diagram

B.3 Software

B.3.1 Database Format

All of the data acquired during an experiment is stored in plain text format. The data is continuously written to disk during the experiment. So if an interruption occurs, all of the data that was acquired prior to the interruption will be saved.

Each time a test is run, a new sub-folder is created inside the "Data" folder with the date and time as the folder name. This prevents the possibility of accidentally overwriting a previous test and it provides a record of when the test was conducted. The data acquisition software creates six text files within each test folder:

- Flow.csv: records the output from the Arduino that reads the flow meter and controls the VFD
- Geometry.txt: contains the x position, y position, channel angle, pitch, jet height, and channel height values that were enter into the GUI by the user
- NI_temperatures.csv: created by the accompanying LabView VI and contains measured values from all of the thermocouples
- Steady_States.txt: records the times at which the system reached a steady state
- Power.csv: records the setting of the power supply during the test
- Pressure.csv: records the output from the Arduino that reads the pressure sensor

Appendix C

Data Reduction

C.1 Calculating Local Surface Values

For illustration purposes, the process of converting raw temperature measurements into a map of the surface values is presented here for a small data set, shown in Table C.1, where $T_{TC,1}$–$T_{TC,3}$ are for the upstream thermocouples, $T_{TC,4}$–$T_{TC,6}$ are for the central thermocouples, $T_{TC,7}$–$T_{TC,9}$ are for the downstream thermocouples, $T_{TC,10}$–$T_{TC,12}$ are for the transverse thermocouples, and $T_{TC,in}$ is for the fluid inlet thermocouple.[1]

Table C.1: Sample data set: temperatures

Upstream			Central			Downstream			Transverse			
$T_{TC,1}$ (°C)	$T_{TC,2}$ (°C)	$T_{TC,3}$ (°C)	$T_{TC,4}$ (°C)	$T_{TC,5}$ (°C)	$T_{TC,6}$ (°C)	$T_{TC,7}$ (°C)	$T_{TC,8}$ (°C)	$T_{TC,9}$ (°C)	$T_{TC,10}$ (°C)	$T_{TC,11}$ (°C)	$T_{TC,12}$ (°C)	$T_{TC,in}$ (°C)
41.95	42.84	43.73	41.59	42.60	43.57	41.70	42.75	43.71	41.54	42.54	43.35	30.72
41.99	42.88	43.76	41.62	42.62	43.60	41.72	42.78	43.73	41.58	42.57	43.38	30.71
41.99	42.89	43.77	41.63	42.63	43.61	41.73	42.79	43.75	41.60	42.58	43.38	30.72
42.02	42.92	43.81	41.67	42.66	43.64	41.76	42.81	43.78	41.61	42.60	43.41	30.73
41.99	42.88	43.77	41.60	42.63	43.61	41.72	42.78	43.75	41.57	42.56	43.37	30.72

The local surface properties for each thermocouple group are calculated independently from the other thermocouple groups. Detailed sample calculations for the central group are given below.

[1]For brevity, this sample data set only includes 5 measurements for each thermocouple. However, 300 measurements were used for each thermocouple in the full calculations.

The temperature of each thermocouple within the copper block is first converted to a temperature difference relative to the fluid inlet temperature,

$$\Theta_{\mathrm{TC},i} = T_{\mathrm{TC},i} - T_{\mathrm{TC,in}} \tag{C.1}$$

$$\begin{aligned} \Theta_{\mathrm{TC},4} &= T_{\mathrm{TC},4} - T_{\mathrm{TC,in}} \\ &= 41.59^{\circ}\mathrm{C} - 30.72^{\circ}\mathrm{C} \\ &= 10.87^{\circ}\mathrm{C}. \end{aligned} \tag{C.2}$$

The temperature differences are then averaged for each thermocouple,

$$\overline{\Theta}_{\mathrm{TC},i} = \frac{1}{n}\sum_{j=1}^{n} \Theta_{\mathrm{TC},i,j} \tag{C.3}$$

$$\begin{aligned} \overline{\Theta}_{\mathrm{TC},4} &= \frac{1}{5}\sum_{j=1}^{5} \Theta_{\mathrm{TC},4,j} \\ &= \frac{1}{5}\left(10.87^{\circ}\mathrm{C} + 10.90^{\circ}\mathrm{C} + 10.91^{\circ}\mathrm{C} + 10.94^{\circ}\mathrm{C} + 10.88^{\circ}\mathrm{C}\right) \\ &= 10.90^{\circ}\mathrm{C} \end{aligned} \tag{C.4}$$

The resulting temperature differences for the sample data set are shown in Table C.2, with the average for each column shown in the bottom row.

Table C.2: Calculated temperature differences with the bottom row showing the average of each column

Upstream			Central			Downstream			Transverse		
$\Theta_{\mathrm{TC},1}$ (°C)	$\Theta_{\mathrm{TC},2}$ (°C)	$\Theta_{\mathrm{TC},3}$ (°C)	$\Theta_{\mathrm{TC},4}$ (°C)	$\Theta_{\mathrm{TC},5}$ (°C)	$\Theta_{\mathrm{TC},6}$ (°C)	$\Theta_{\mathrm{TC},7}$ (°C)	$\Theta_{\mathrm{TC},8}$ (°C)	$\Theta_{\mathrm{TC},9}$ (°C)	$\Theta_{\mathrm{TC},10}$ (°C)	$\Theta_{\mathrm{TC},11}$ (°C)	$\Theta_{\mathrm{TC},12}$ (°C)
11.23	12.12	13.01	10.87	11.88	12.85	10.98	12.03	12.99	10.82	11.82	12.63
11.28	12.17	13.05	10.91	11.91	12.89	11.01	12.07	13.02	10.87	11.86	12.67
11.27	12.17	13.05	10.91	11.91	12.89	11.01	12.07	13.03	10.88	11.86	12.66
11.29	12.19	13.08	10.94	11.93	12.91	11.03	12.08	13.05	10.88	11.87	12.68
11.27	12.16	13.05	10.88	11.91	12.89	11.00	12.06	13.03	10.85	11.84	12.65
11.27	12.16	13.05	10.90	11.91	12.89	11.01	12.06	13.02	10.86	11.85	12.66

The thermocouples in each group are located 3 mm, 8 mm, and 13 mm below the impingement surface.

$$z_{\mathrm{TC},1} = z_{\mathrm{TC},4} = z_{\mathrm{TC},7} = z_{\mathrm{TC},10} = -0.003\,\mathrm{m} \tag{C.5}$$

$$z_{\mathrm{TC},2} = z_{\mathrm{TC},5} = z_{\mathrm{TC},8} = z_{\mathrm{TC},11} = -0.008\,\mathrm{m} \tag{C.6}$$

$$z_{\mathrm{TC},3} = z_{\mathrm{TC},6} = z_{\mathrm{TC},9} = z_{\mathrm{TC},12} = -0.013\,\mathrm{m} \tag{C.7}$$

A linear regression is applied to the three average temperature differences of each thermocouple group based on the distance of the thermocouples from the surface to obtain a correlation of the form,

$$\Theta = m_g z + b_g \tag{C.8}$$

where the slope of the line, m_g, is calculated with

$$m_g = \frac{\sum_i (z_{\mathrm{TC},i} - \overline{z}_g)(\overline{\Theta}_{\mathrm{TC},i} - \overline{\Theta}_g)}{\sum_i (z_{\mathrm{TC},i} - \overline{z}_g)^2}, \tag{C.9}$$

and the intercept, b_g, is calculated with

$$b_g = \overline{\Theta}_g - m_g \overline{z}_g \tag{C.10}$$

For the central thermocouple group in the sample data set, the linear regression calculation would be:

$$\begin{aligned}\overline{\Theta}_2 &= \frac{10.9°\mathrm{C} + 11.91°\mathrm{C} + 12.88°\mathrm{C}}{3} \\ &= 11.90°\mathrm{C}\end{aligned} \tag{C.11}$$

$$\begin{aligned}\overline{z}_2 &= \frac{(-0.003\,\mathrm{m}) + (-0.008\,\mathrm{m}) + (-0.013\,\mathrm{m})}{3} \\ &= -0.008\,\mathrm{m}\end{aligned} \tag{C.12}$$

$$\begin{aligned}m_2 &= \frac{\sum_{i=4}^{6}(z_{\mathrm{TC},i} - \overline{z}_2)(\overline{\Theta}_{\mathrm{TC},i} - \overline{\Theta}_2)}{\sum_{i=4}^{6}(z_{\mathrm{TC},i} - \overline{z}_2)^2} \\ &= \frac{(-0.003\,\mathrm{m} - [-0.008\,\mathrm{m}])(11.90°\mathrm{C} - 10.9°\mathrm{C}) + \ldots}{(-0.003\,\mathrm{m} - [-0.008\,\mathrm{m}])^2 + \ldots} \\ &= -198.4\,\frac{°\mathrm{C}}{\mathrm{m}}\end{aligned} \tag{C.13}$$

$$\begin{aligned}b_2 &= \overline{\Theta}_2 - m_2\overline{z}_2 \\ &= 11.90°\mathrm{C} - \left(-198.4\,\frac{°\mathrm{C}}{\mathrm{m}}\right)(-0.008\,\mathrm{m}) \\ &= 10.31°\mathrm{C}\end{aligned} \tag{C.14}$$

The slope of the regression, m_g, is an estimate of temperature gradient at the surface,

$$\left.\frac{\partial T_g}{\partial z}\right|_{z=0} \approx m_g, \tag{C.15}$$

and the intercept of the correlation, b_g, is an estimate of the temperature rise at the surface,

$$\Theta_g \approx b_g. \tag{C.16}$$

The local heat flux at the surface can be obtained by using the estimated temperature gradient at the surface with Fourier's law,

$$\dot{q}_g'' = -k_c \left. \frac{\partial T_g}{\partial z} \right|_{z=0} \tag{C.17}$$

where $k_c = 401\,\mathrm{W/(m \cdot K)}$ is the thermal conductivity of the copper block.

The estimated surface temperature rise and the estimated heat flux can then be used to estimate the local heat transfer coefficient using Newton's law of cooling,

$$h_g = \frac{\dot{q}_g''}{\Theta_g}. \tag{C.18}$$

The heat transfer coefficient can then be used to calculate the local Nusselt number,

$$Nu_{D_n,g} = \frac{h_g D_n}{k_w} \tag{C.19}$$

where $D_n = 3.175\,\mathrm{mm}$ is the inside nozzle diameter and $k_w = 0.614\,\mathrm{kW/(m \cdot K)}$ is the thermal conductivity of the water.

For the central thermocouple group in the sample data set, the surface values would be calculated as

$$\Theta_2 \approx b_2 = 10.31^{\circ}\mathrm{C} \tag{C.20}$$

$$\left.\frac{\partial T_2}{\partial z}\right|_{z=0} \approx m_2 = -198.4\,\frac{^{\circ}\mathrm{C}}{\mathrm{m}} \tag{C.21}$$

$$\begin{aligned} \dot{q}_2'' &= -k_c \left.\frac{\partial T_2}{\partial z}\right|_{z=0} \\ &= -401\,\frac{\mathrm{W}}{\mathrm{m}\cdot\mathrm{K}}\left(-198.4\,\frac{^{\circ}\mathrm{C}}{\mathrm{m}}\right) \\ &= -79,558\,\frac{\mathrm{W}}{\mathrm{m}^2} \end{aligned} \tag{C.22}$$

$$\begin{aligned} h_2 &= \frac{\dot{q}_2''}{\Theta_2} \\ &= \frac{79,558\,\mathrm{W/m^2}}{10.31\,^{\circ}\mathrm{C}} \\ &= 7,715\,\frac{\mathrm{W}}{\mathrm{m}^2\cdot\mathrm{K}} \end{aligned} \tag{C.23}$$

$$\begin{aligned} Nu_{D_n,2} &= \frac{h_2 D_n}{k_w} \\ &= \frac{7,715\,\mathrm{W/(m^2\cdot K)}\cdot 0.003175\,\mathrm{m}}{0.614\,\mathrm{W/(m\cdot K)}} \\ &= 39.90 \end{aligned} \tag{C.24}$$

The resulting surface values for the sample data set are shown in Table C.3.

Table C.3: Calculated local surface values

	Upstream	Central	Downstream	Transverse
$\Theta\,(^{\circ}\mathrm{C})$	10.74	10.31	10.41	10.35
$\dot{q}''\,(\mathrm{kW/m^2})$	71.38	79.56	80.92	72.09
$h\,(\mathrm{kW/(m^2\cdot K)})$	6.65	7.72	7.77	6.97
Nu_{D_n}	34.38	39.90	40.17	36.02

C.2 Calculating Average Surface Values

Nine translated tests were conducted for each case (geometric parameters and flow rates) in the study. The steps shown above in C.1 were performed for each test, resulting in 36 local surface values for each case. An example of the local surface values obtained for one set of geometric parameters at one flow rate is shown in Table C.4.

Table C.4: Sample data set: local surface values

$\gamma\,(^\circ)$	P^*	H^*	L_n^*	Re_{D_n}	x^*	y^*	$\Theta\,(^\circ\mathrm{C})$	$\dot{q}''\,(\mathrm{kW/m^2})$	$h\,(\mathrm{kW/(m^2\cdot K)})$	Nu_{D_n}
0	6	1	0	5,600	−4	−1	11.56	75.49	6.53	33.78
0	6	1	0	5,600	−4	0	10.91	73.98	6.78	35.05
0	6	1	0	5,600	−4	1	11.38	75.19	6.61	34.18
0	6	1	0	5,600	−3	−1	10.79	75.77	7.02	36.30
0	6	1	0	5,600	−3	0	10.39	76.59	7.37	38.12
0	6	1	0	5,600	−3	1	11.00	76.12	6.92	35.78
0	6	1	0	5,600	−2	−1	11.46	76.93	6.71	34.71
0	6	1	0	5,600	−2	0	10.97	76.82	7.01	36.23
0	6	1	0	5,600	−2	1	10.56	78.18	7.40	38.27
0	6	1	0	5,600	−1	−1	11.28	81.36	7.22	37.31
0	6	1	0	5,600	−1	0	10.66	79.64	7.47	38.64
0	6	1	0	5,600	−1	1	11.14	80.28	7.20	37.26
0	6	1	0	5,600	−1	2	11.37	72.58	6.38	33.01
0	6	1	0	5,600	−1	3	10.85	70.41	6.49	33.55
0	6	1	0	5,600	−1	4	11.42	73.66	6.45	33.34
0	6	1	0	5,600	0	−1	10.55	81.96	7.77	40.18
0	6	1	0	5,600	0	0	10.15	82.70	8.15	42.13
0	6	1	0	5,600	0	1	10.80	81.76	7.57	39.16
0	6	1	0	5,600	0	2	10.61	73.13	6.90	35.66
0	6	1	0	5,600	0	3	10.37	73.48	7.09	36.65
0	6	1	0	5,600	0	4	11.04	74.71	6.77	35.00
0	6	1	0	5,600	1	−1	11.37	79.11	6.96	35.97
0	6	1	0	5,600	1	0	10.90	78.69	7.22	37.34
0	6	1	0	5,600	1	1	10.55	80.02	7.58	39.22
0	6	1	0	5,600	1	2	11.41	70.35	6.16	31.87
0	6	1	0	5,600	1	3	11.05	69.69	6.31	32.61
0	6	1	0	5,600	1	4	10.75	73.03	6.79	35.13
0	6	1	0	5,600	2	−1	11.47	74.13	6.46	33.41
0	6	1	0	5,600	2	0	10.92	70.87	6.49	33.55
0	6	1	0	5,600	2	1	11.42	71.74	6.28	32.49
0	6	1	0	5,600	3	−1	10.83	74.25	6.86	35.45
0	6	1	0	5,600	3	0	10.48	73.99	7.06	36.50
0	6	1	0	5,600	3	1	11.13	72.88	6.55	33.86
0	6	1	0	5,600	4	−1	11.56	73.89	6.39	33.06
0	6	1	0	5,600	4	0	11.11	72.98	6.57	33.97
0	6	1	0	5,600	4	1	10.89	73.86	6.78	35.06

The local surface values were numerically integrated over the area of interest, shown in Figure 3.7, to obtain the average surface value. The average heat transfer coefficient is defined as

$$\overline{h} = \frac{2}{(P^*)^2} \int_{-\frac{P^*}{2}}^{\frac{P^*}{2}} \int_{0}^{\frac{P^*}{2}} h \, dy^* dx^*. \tag{C.25}$$

While the area of interest varies with the pitch, the sampled locations from the translated tests were not sufficient to fully cover the unit cell of the central jet due to the missing regions at the corners furthest from the stagnation region. Neglecting the regions outside of the sampled area in the averaging calculations would lead to artificially high average heat transfers due to overweighting the effects of the high heat transfer in the stagnation region. In order to avoid this effect, the sampled values were used to create best guess estimates for the missing locations in the unit cell. The estimates were obtained by averaging the values at the known locations at comparable distances from the stagnation point as the missing location. For instance, the missing heat transfer coefficient values, $h_{(x^*,y^*)}$, were estimated as:

$$h_{(-2,2)} \approx \frac{h_{(-3,1)} + h_{(-1,3)}}{2} \tag{C.26}$$

$$h_{(2,2)} \approx \frac{h_{(3,1)} + h_{(1,3)}}{2} \tag{C.27}$$

$$h_{(-3,2)} \approx h_{(-4,1)} \tag{C.28}$$

$$h_{(-2,3)} \approx h_{(-1,4)} \tag{C.29}$$

$$h_{(3,2)} \approx h_{(4,1)} \tag{C.30}$$

$$h_{(2,3)} \approx h_{(1,4)} \tag{C.31}$$

$$h_{(-3,3)} \approx \frac{h_{(-4,1)} + h_{(-1,4)}}{2} \tag{C.32}$$

$$h_{(3,3)} \approx \frac{h_{(4,1)} + h_{(1,4)}}{2} \tag{C.33}$$

The integration was performed using a 2-D rectangle rule calculation. The value at each measured/estimated location was treated as being the value for a cell extending half-way to the next location. The products of the area and the magnitude for each measurement cell were summed and then divided by the area of the jet unit cell to get the average surface value for the jet.

$$\overline{h} = \frac{2}{(P^*)^2} \sum_{x^*=-\frac{P^*}{2}}^{\frac{P^*}{2}} \sum_{y^*=0}^{\frac{P^*}{2}} h_{(x^*,y^*)} \cdot A_{(x^*,y^*)} \tag{C.34}$$

$$A_{(x^*,y^*)} = \begin{cases} \Delta x^* \cdot \Delta y^* & |x^*| < \frac{P^*}{2} \text{ and } 0 < y^* < \frac{P^*}{2} \\ \frac{\Delta x^* \cdot \Delta y^*}{2} & |x^*| < \frac{P^*}{2} \text{ and } y^* = 0 \text{ or } \frac{P^*}{2} \\ \frac{\Delta x^* \cdot \Delta y^*}{2} & |x^*| = \frac{P^*}{2} \text{ and } 0 < y^* < \frac{P^*}{2} \\ \frac{\Delta x^* \cdot \Delta y^*}{4} & |x^*| = \frac{P^*}{2} \text{ and } y^* = 0 \text{ or } \frac{P^*}{2} \end{cases} \tag{C.35}$$

For the sample data given in Table C.4, the average heat transfer coefficient would be calculated as

$$\begin{aligned}\overline{h} = \frac{2\Delta x^*\Delta y^*}{(P^*)^2}\Bigg(&\frac{h_{(-3,0)}}{4} + \frac{h_{(-2,0)}}{2} + \frac{h_{(-1,0)}}{2} + \frac{h_{(0,0)}}{2} + \frac{h_{(1,0)}}{2} + \frac{h_{(2,0)}}{2} + \frac{h_{(3,0)}}{4} \\ &+ \frac{h_{(-3,1)}}{2} + h_{(-2,1)} + h_{(-1,1)} + h_{(0,1)} + h_{(1,1)} + h_{(2,1)} + \frac{h_{(3,1)}}{2} \\ &+ \frac{h_{(-3,2)}}{2} + h_{(-2,2)} + h_{(-1,2)} + h_{(0,2)} + h_{(1,2)} + h_{(2,2)} + \frac{h_{(3,2)}}{2} \\ &+ \frac{h_{(-3,3)}}{4} + \frac{h_{(-2,3)}}{2} + \frac{h_{(-1,3)}}{2} + \frac{h_{(0,3)}}{2} + \frac{h_{(1,3)}}{2} + \frac{h_{(2,3)}}{2} + \frac{h_{(3,3)}}{4}\Bigg)\end{aligned} \tag{C.36}$$

$$\begin{aligned}\overline{h} = \frac{2}{6^2}\Bigg(&\frac{7.37}{4} + \frac{7.01}{2} + \frac{7.47}{2} + \frac{8.15}{2} + \frac{7.22}{2} + \frac{6.49}{2} + \frac{7.06}{4} \\ &+ \frac{6.92}{2} + 7.40 + 7.20 + 7.57 + 7.58 + 6.28 + \frac{6.55}{2} \\ &+ \frac{6.53}{2} + 6.705 + 6.38 + 6.90 + 6.16 + 6.43 + \frac{6.78}{2} \\ &+ \frac{6.53}{4} + \frac{6.45}{2} + \frac{6.49}{2} + \frac{7.09}{2} + \frac{6.31}{2} + \frac{6.79}{2} + \frac{6.785}{4}\Bigg)\frac{\text{kW}}{\text{m}^2 \cdot \text{K}}\end{aligned} \tag{C.37}$$

$$\overline{h} = 6.87\,\frac{\text{kW}}{\text{m}^2 \cdot \text{K}} \tag{C.38}$$

Appendix D

Experimental Uncertainty Analysis

D.1 Sequential Perturbations

The uncertainty of a quantity derived from a combination of measurements, each with their own uncertainties, can be found through the method of sequential perturbations as presented by Moffat [99]. In this approach the best guess values for each of the measurements are used to calculate the parameter of interest which is stored. Each of the constituent measurements are then individually perturbed by their uncertainty and the difference between the new value and the original value is stored. Once all the variables have been perturbed, the differences are added in quadrature. The resulting uncertainty can be expressed as

$$\delta_X = \pm \sqrt{\sum_i \left(\frac{|X_o - X_{i+\delta_i}| + |X_o - X_{i-\delta_i}|}{2} \right)^2} \tag{D.1}$$

where X_o is the original value that would have been calculated if the uncertainties were ignored, $X_{i+\delta_i}$ is the value that would have been calculated if the i^{th} measurement had been increased by its uncertainty, and $X_{i-\delta_i}$ is the value that would have been calculated if the i^{th} measurement had been decreased by its uncertainty.

D.2 Thermocouple Uncertainty

Each thermocouple was individually calibrated to a reference thermistor. The uncertainty of each thermocouple measurement was approximated by the uncertainty of the calibration fit.

$$\delta_{T_1} = \pm(0.0091 \cdot T_1 + 0.569)^\circ\text{C} \tag{D.2}$$

$$\delta_{T_2} = \pm(0.0109 \cdot T_2 + 0.676)^\circ\text{C} \tag{D.3}$$

$$\delta_{T_3} = \pm(0.0054 \cdot T_3 + 0.334)^\circ\text{C} \tag{D.4}$$

$$\delta_{T_4} = \pm(0.0051 \cdot T_4 + 0.318)^\circ\text{C} \tag{D.5}$$

$$\delta_{T_5} = \pm(0.0034 \cdot T_5 + 0.223)^\circ\text{C} \tag{D.6}$$

$$\delta_{T_6} = \pm(0.0035 \cdot T_6 + 0.219)^\circ\text{C} \tag{D.7}$$

$$\delta_{T_7} = \pm(0.0035 \cdot T_7 + 0.221)^\circ\text{C} \tag{D.8}$$

$$\delta_{T_8} = \pm(0.0049 \cdot T_8 + 0.307)^\circ\text{C} \tag{D.9}$$

$$\delta_{T_9} = \pm(0.0046 \cdot T_9 + 0.290)^\circ\text{C} \tag{D.10}$$

$$\delta_{T_{10}} = \pm(0.0085 \cdot T_{10} + 0.527)^\circ\text{C} \tag{D.11}$$

$$\delta_{T_{11}} = \pm(0.0092 \cdot T_{11} + 0.573)^\circ\text{C} \tag{D.12}$$

$$\delta_{T_{12}} = \pm(0.0115 \cdot T_{12} + 0.718)^\circ\text{C} \tag{D.13}$$

For each experiment, the system was allowed to reach steady state. The temperature was then taken to be the average of 300 readings. The uncertainty of each average temperature was found through the method of sequential perturbations. Typical values for the average uncertainties of the temperature measurements are:

$$\delta_{T_{1,\text{avg}}} = \pm 0.054^{\circ}\text{C} \tag{D.14}$$

$$\delta_{T_{2,\text{avg}}} = \pm 0.064^{\circ}\text{C} \tag{D.15}$$

$$\delta_{T_{3,\text{avg}}} = \pm 0.032^{\circ}\text{C} \tag{D.16}$$

$$\delta_{T_{4,\text{avg}}} = \pm 0.030^{\circ}\text{C} \tag{D.17}$$

$$\delta_{T_{5,\text{avg}}} = \pm 0.021^{\circ}\text{C} \tag{D.18}$$

$$\delta_{T_{6,\text{avg}}} = \pm 0.021^{\circ}\text{C} \tag{D.19}$$

$$\delta_{T_{7,\text{avg}}} = \pm 0.021^{\circ}\text{C} \tag{D.20}$$

$$\delta_{T_{8,\text{avg}}} = \pm 0.030^{\circ}\text{C} \tag{D.21}$$

$$\delta_{T_{9,\text{avg}}} = \pm 0.027^{\circ}\text{C} \tag{D.22}$$

$$\delta_{T_{10,\text{avg}}} = \pm 0.050^{\circ}\text{C} \tag{D.23}$$

$$\delta_{T_{11,\text{avg}}} = \pm 0.054^{\circ}\text{C} \tag{D.24}$$

$$\delta_{T_{12,\text{avg}}} = \pm 0.068^{\circ}\text{C} \tag{D.25}$$

D.3 Local Surface Measurement Uncertainties

The averaged temperature measurements were used in conjunction with their locations to create a linear fit. The intercept of the linear fit was used to estimate the surface temperature and the slope of the linear fit was used to estimate the temperature gradient at the surface. The temperature gradient was combined with the known thermal conductivity of the copper measurement block to estimate the heat flux at the surface. The heat flux at the surface was combined with the temperature difference between the surface and the fluid inlet temperature to obtain the heat transfer coefficient. The method of sequential perturbations was used to propagate the temperature uncertainties and the location tolerances into the surface property calculations. Typical values for the uncertainties of the local surface

measurements are:

$$\delta_{\Theta_{s,1}} = \pm 1.07\% \qquad \delta_{\dot{q}''_{s,1}} = \pm 7.72\% \qquad \delta_{h_1} = \pm 8.73\% \tag{D.26}$$

$$\delta_{\Theta_{s,2}} = \pm 1.24\% \qquad \delta_{\dot{q}''_{s,2}} = \pm 7.63\% \qquad \delta_{h_2} = \pm 8.76\% \tag{D.27}$$

$$\delta_{\Theta_{s,3}} = \pm 1.15\% \qquad \delta_{\dot{q}''_{s,3}} = \pm 6.40\% \qquad \delta_{h_3} = \pm 7.42\% \tag{D.28}$$

$$\delta_{\Theta_{s,4}} = \pm 1.14\% \qquad \delta_{\dot{q}''_{s,4}} = \pm 7.70\% \qquad \delta_{h_4} = \pm 8.77\% \tag{D.29}$$

where $\delta_{\Theta_{s,i}}$ is the uncertainty in the local temperature rise at the surface, $\delta_{\dot{q}''_{s,i}}$ is the uncertainty in the local heat flux at the surface, and δ_{h_i} is the uncertainty in the local heat transfer coefficient for the i^{th} location.

D.4 Surface Average Measurement Uncertainties

The mean heat transfer coefficient and mean Nusselt Number, for each configuration, were obtained by integrating over the area of interest shown in Figure 3.7, half the area of the central jet,

$$\overline{h} = \frac{2}{(P^*)^2} \int_{-\frac{P^*}{2}}^{\frac{P^*}{2}} \int_{0}^{\frac{P^*}{2}} h \, dy^* dx^* \tag{D.30}$$

$$\overline{Nu}_{D_n} = \frac{2}{(P^*)^2} \int_{-\frac{P^*}{2}}^{\frac{P^*}{2}} \int_{0}^{\frac{P^*}{2}} Nu_{D_n} \, dy^* dx^* \tag{D.31}$$

The uncertainty of the average surface quantities was again found through the method of sequential perturbations. Typical values for the uncertainties of the surface average heat transfer coefficient are:

$$\delta_{\overline{h}} = \pm 2.50\% \quad \text{for} \quad P^* = 4 \tag{D.32}$$

$$\delta_{\overline{h}} = \pm 1.89\% \quad \text{for} \quad P^* = 6 \tag{D.33}$$

The uncertainty of the surface average, $\delta_{\overline{h}}$, is dependent on the pitch, P^*, because the number of local measurements that fall into the region of interest varies with pitch. The largest pitch, $P^* = 6$, has more measurements included in the surface integral than the smallest pitch, $P^* = 4$. Therefore, the surface average at the larger pitch is less sensitive to the uncertainty of each of the constituent measurements than is the surface average at the smaller pitch.

Appendix E

Experimental Results

E.1 Experimental Data Summary

The numerical experimental results are presented in Table E.1, where each row includes both the average and local maximum values for both the heat transfer coefficient and the Nusselt number. Each geometry and flow rate were tested at nine different translated locations, resulting in 36 individual surface measurements and a minimum of 4.5 hours of testing for each row in the table.

Table E.1: Summary of experimental data

γ	P^*	H^*	L_n^*	Re_{D_n}	$\overline{h}\,(\mathrm{W/m^2K})$	$h_{\max}\,(\mathrm{W/m^2K})$	$\overline{Nu}_{D_n}$	$Nu_{D_n,\max}$
0	4	1	0	5,600	6,970	7,670	36.0	39.7
0	4	1	0	8,400	8,760	9,650	45.3	49.9
0	4	1	0	11,200	10,300	11,400	53.2	58.9
0	4	1	0	14,000	11,500	12,700	59.2	65.9
0	4	1	2	11,200	10,900	12,400	56.1	64.1
0	4	2	0	5,600	7,970	8,550	41.2	44.2
0	4	2	0	8,400	10,000	10,800	51.8	55.9
0	4	2	0	11,200	11,700	12,800	60.6	66.1
0	4	2	0	14,000	13,100	14,300	67.6	74.1
0	4	2	2	11,200	10,300	11,500	53.0	59.3
0	4	3	0	5,600	6,750	7,590	34.9	39.3
0	4	3	0	8,400	8,410	9,550	43.5	49.4

Continued on next page

Table E.1 (continued): Summary of experimental data

γ	P^*	H^*	L_n^*	Re_{D_n}	$\overline{h}\,(\mathrm{W/m^2K})$	$h_{\max}\,(\mathrm{W/m^2K})$	$\overline{Nu}_{D_n}$	$Nu_{D_n,\max}$
0	4	3	0	11,200	9,830	11,200	50.8	57.9
0	4	3	0	14,000	10,900	12,600	56.6	65.3
0	4	3	2	11,200	9,150	10,300	47.3	53.2
0	6	1	0	5,600	6,870	8,150	35.5	42.1
0	6	1	0	8,400	8,880	10,600	45.9	54.9
0	6	1	0	11,200	10,700	12,600	55.2	65.3
0	6	1	0	14,000	12,000	13,900	62.2	71.9
0	6	1	2	5,600	7,540	8,700	39.0	45.0
0	6	1	2	8,400	9,690	11,400	50.1	58.8
0	6	1	2	11,200	11,600	13,600	59.8	70.2
0	6	1	2	14,000	13,100	15,600	67.5	80.5
0	6	2	0	5,600	7,870	8,930	40.7	46.2
0	6	2	0	8,400	9,940	11,100	51.4	57.6
0	6	2	0	11,200	11,700	13,300	60.6	68.6
0	6	2	0	14,000	13,100	14,700	67.7	75.9
0	6	2	2	5,600	7,410	8,770	38.3	45.4
0	6	2	2	8,400	9,370	11,100	48.5	57.2
0	6	2	2	11,200	11,000	12,900	57.1	66.5
0	6	2	2	14,000	12,200	14,200	63.2	73.5
0	6	3	0	5,600	7,800	8,980	40.3	46.4
0	6	3	0	8,400	9,780	11,300	50.6	58.2
0	6	3	0	11,200	11,500	13,200	59.4	68.3
0	6	3	0	14,000	12,800	14,700	66.4	76.3

Continued on next page

Table E.1 (continued): Summary of experimental data

γ	P^*	H^*	L_n^*	Re_{D_n}	$\overline{h}\,(\mathrm{W/m^2K})$	$h_{\max}\,(\mathrm{W/m^2K})$	$\overline{Nu}_{D_n}$	$Nu_{D_n,\max}$
0	6	3	2	5,600	7,180	8,850	37.1	45.8
0	6	3	2	8,400	9,020	11,100	46.7	57.5
0	6	3	2	11,200	10,700	13,000	55.2	67.1
0	6	3	2	14,000	12,000	14,500	62.2	74.7
5	4	1	0	5,600	7,900	9,200	40.8	47.6
5	4	1	0	8,400	9,980	11,700	51.6	60.7
5	4	1	0	11,200	11,800	13,700	61.2	70.9
5	4	1	0	14,000	13,100	15,100	67.5	77.9
5	4	2	0	5,600	7,240	8,300	37.4	42.9
5	4	2	0	8,400	9,140	10,500	47.2	54.4
5	4	2	0	11,200	10,700	12,300	55.4	63.7
5	4	2	0	14,000	11,900	13,700	61.7	70.7
5	4	3	0	5,600	6,490	6,930	33.6	35.8
5	4	3	0	8,400	8,200	8,630	42.4	44.6
5	4	3	0	11,200	9,570	10,100	49.5	52.2
5	4	3	0	14,000	10,600	11,400	55.0	59.0
5	6	1	0	5,600	7,040	8,160	36.4	42.2
5	6	1	0	8,400	9,040	10,400	46.8	53.7
5	6	1	0	11,200	10,700	12,300	55.5	63.5
5	6	1	0	14,000	12,100	13,900	62.5	72.1
5	6	2	0	5,600	7,520	8,570	38.9	44.3
5	6	2	0	8,400	9,640	10,900	49.9	56.4
5	6	2	0	11,200	11,400	12,800	59.1	66.3

Continued on next page

Table E.1 (continued): Summary of experimental data

γ	P^*	H^*	L_n^*	Re_{D_n}	$\overline{h}\,(\mathrm{W/m^2K})$	$h_{\max}\,(\mathrm{W/m^2K})$	$\overline{Nu}_{D_n}$	$Nu_{D_n,\max}$
5	6	2	0	14,000	12,700	14,300	65.5	74.2
5	6	3	0	5,600	6,930	7,910	35.8	40.9
5	6	3	0	8,400	8,770	10,100	45.3	52.3
5	6	3	0	11,200	10,300	11,800	53.3	61.0
5	6	3	0	14,000	11,500	13,200	59.6	68.4
10	4	1	0	11,200	8,610	9,910	44.5	51.3
10	6	1	0	5,600	6,970	8,390	36.1	43.4
10	6	1	0	8,400	8,950	10,500	46.3	54.5
10	6	1	0	11,200	10,600	12,600	54.8	65.3
10	6	1	0	14,000	12,000	14,100	62.2	73.0
10	6	2	0	5,600	7,110	8,160	36.8	42.2
10	6	2	0	8,400	8,910	10,100	46.1	52.4
10	6	2	0	11,200	10,500	11,900	54.1	61.4
10	6	2	0	14,000	11,600	13,100	60.0	67.8
10	6	3	0	5,600	7,450	8,520	38.5	44.0
10	6	3	0	8,400	9,280	10,600	48.0	54.9
10	6	3	0	11,200	10,800	12,300	55.8	63.7
10	6	3	0	14,000	11,800	13,700	61.1	70.6

E.2 Experimental Surface Maps

Additional surface maps for visualizing the effects of varying the geometric and flow parameters are presented below. The variation with Reynolds number for a constant geometry is shown in Figures E.1–E.5, the variation with jet height with all other parameters being constant is shown in Figures E.6–E.9, the variation with pitch with all other parameter

begin constant is shown in Figures E.10–E.11, and the variation with angle with all other parameters being constant is shown in Figures E.12–E.13.

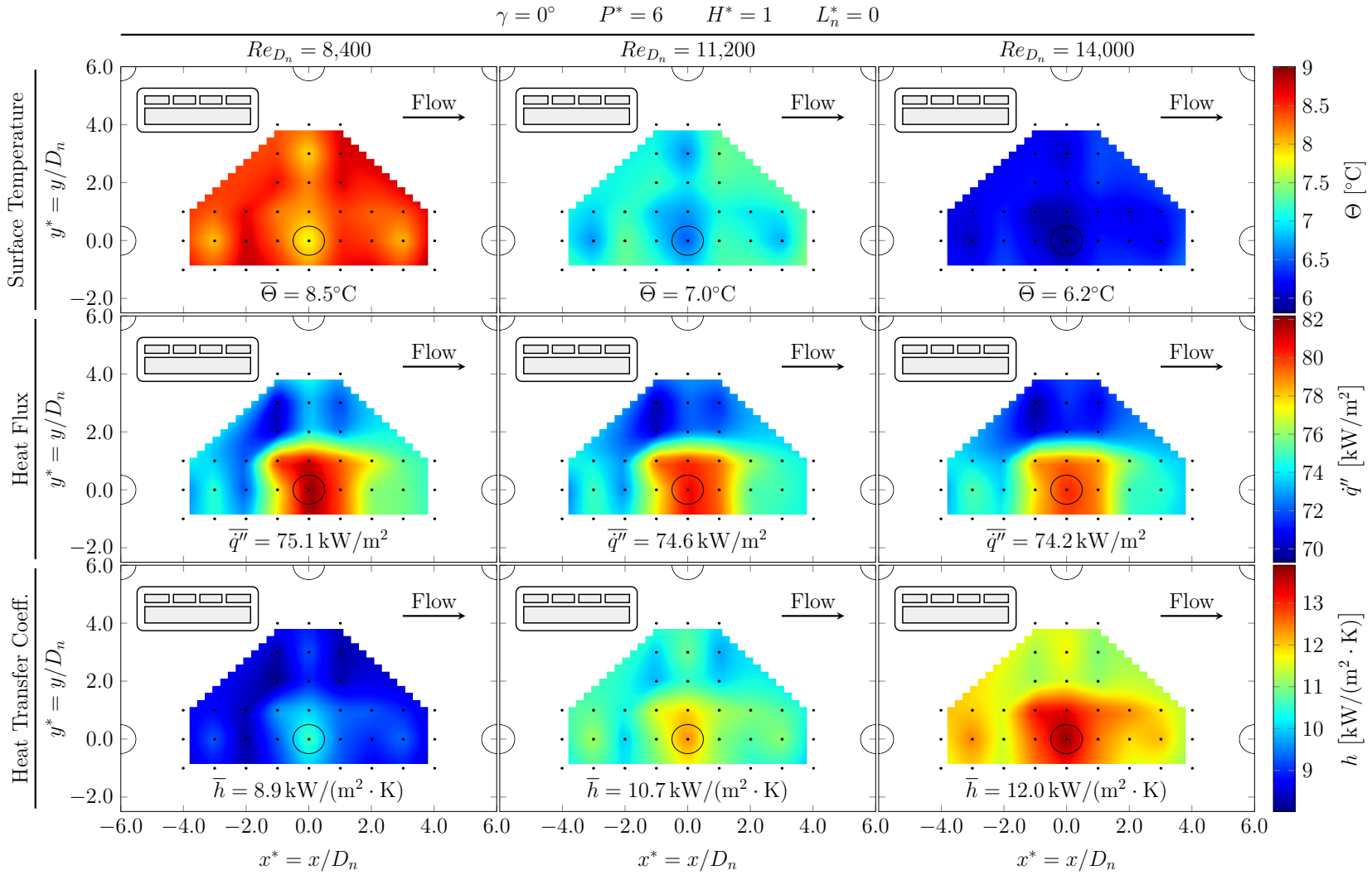

Figure E.1: Surface map comparison of variation with Reynolds number for orifice plates with P^*=6 and H^*=1

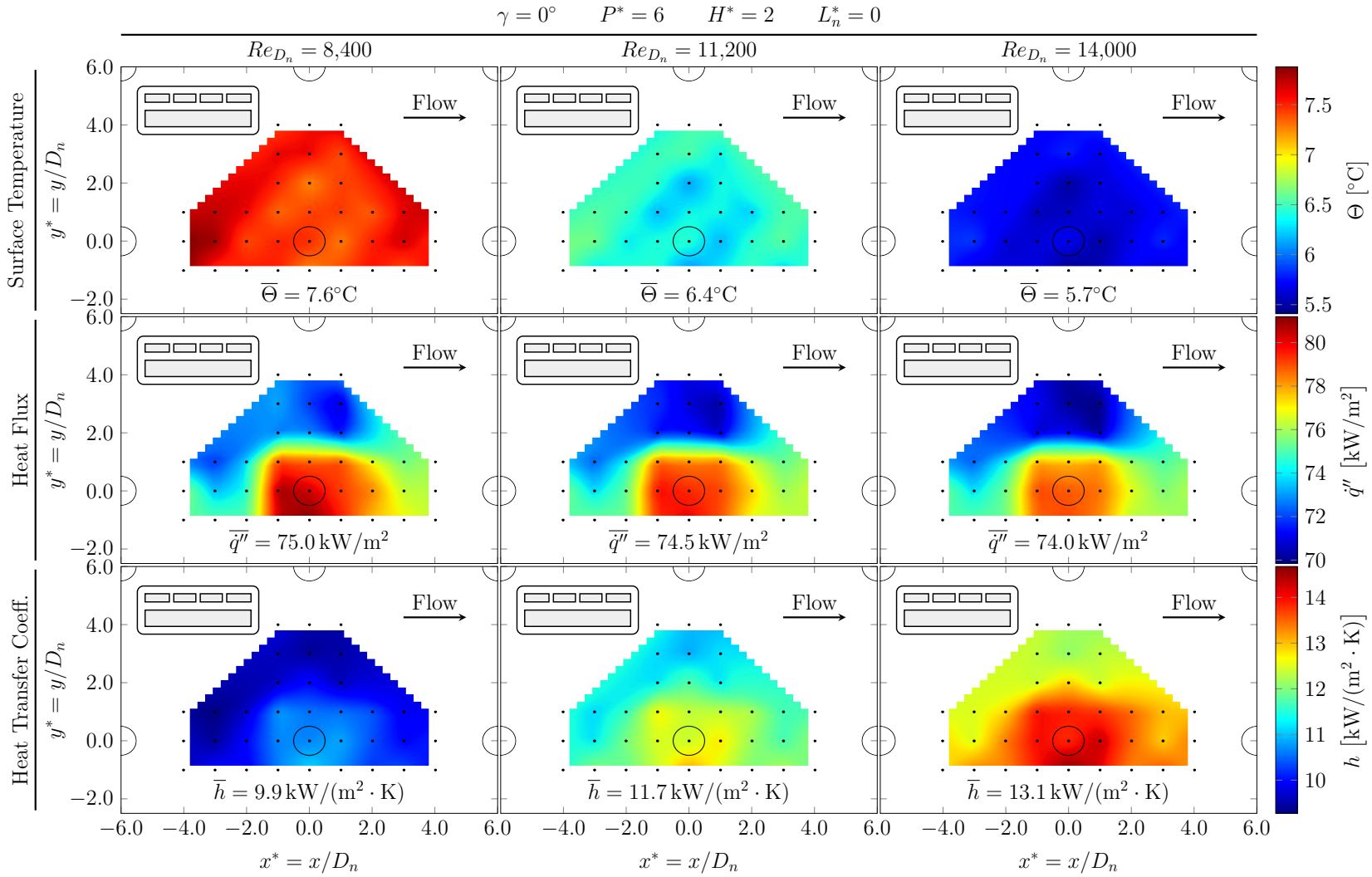

Figure E.2: Surface map comparison of variation with Reynolds number for 5° angled plate with P^*=6 and H^*=2

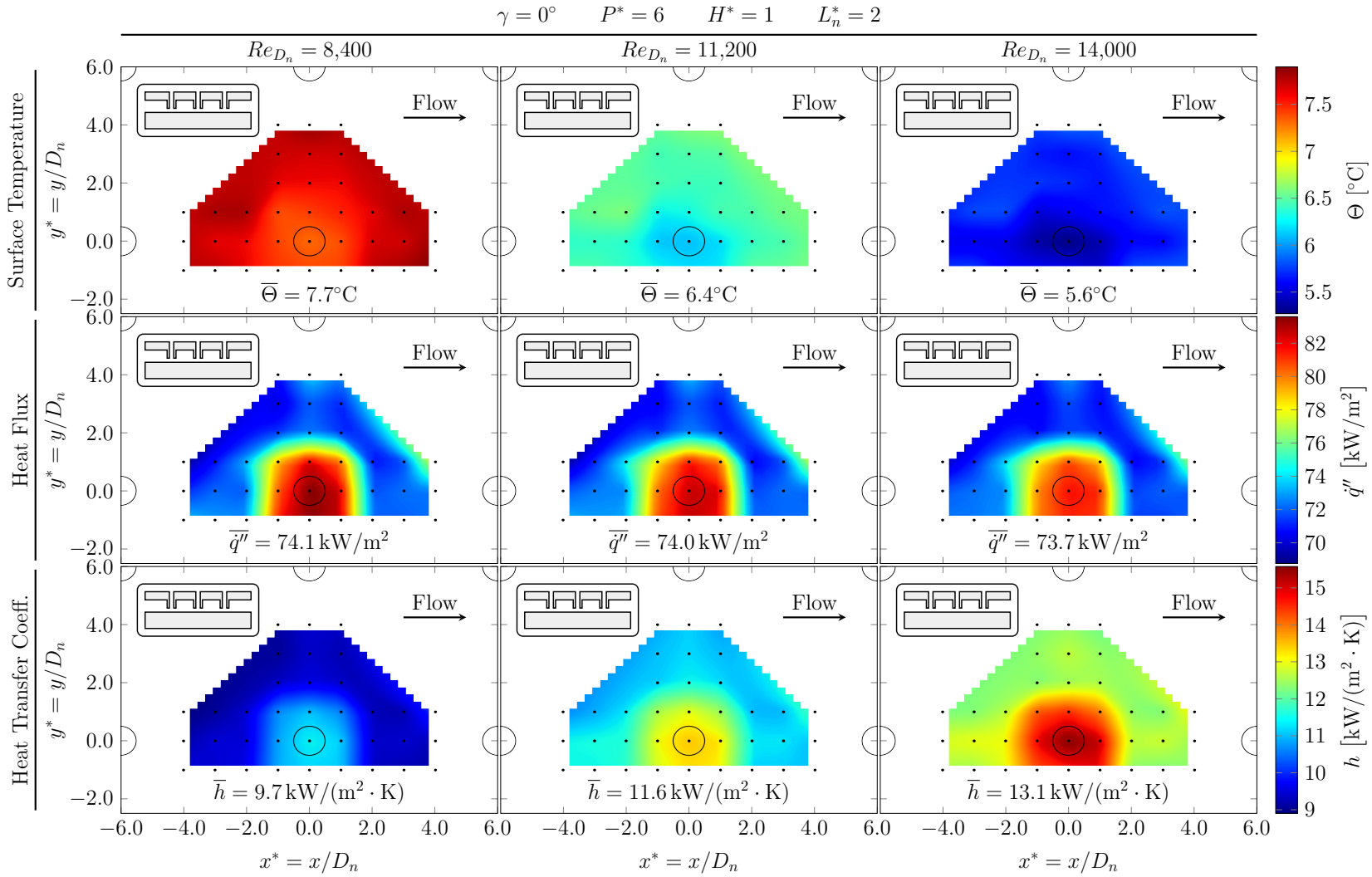

Figure E.3: Surface map comparison of variation with Reynolds number for parallel nozzle plate with P^*=6 and H^*=1

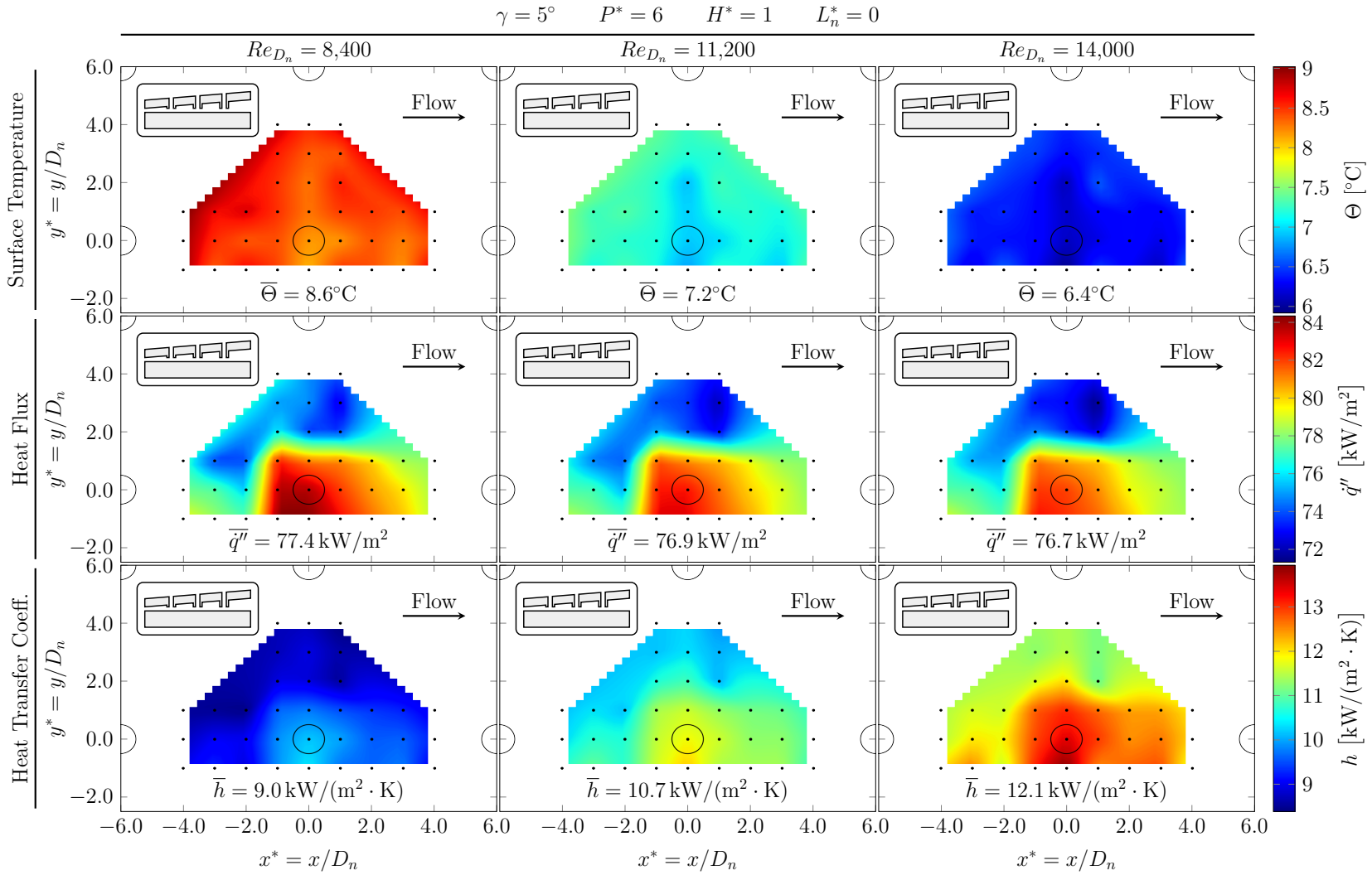

Figure E.4: Surface map comparison of variation with Reynolds number for 5° angled plate with P^*=6 and H^*=1

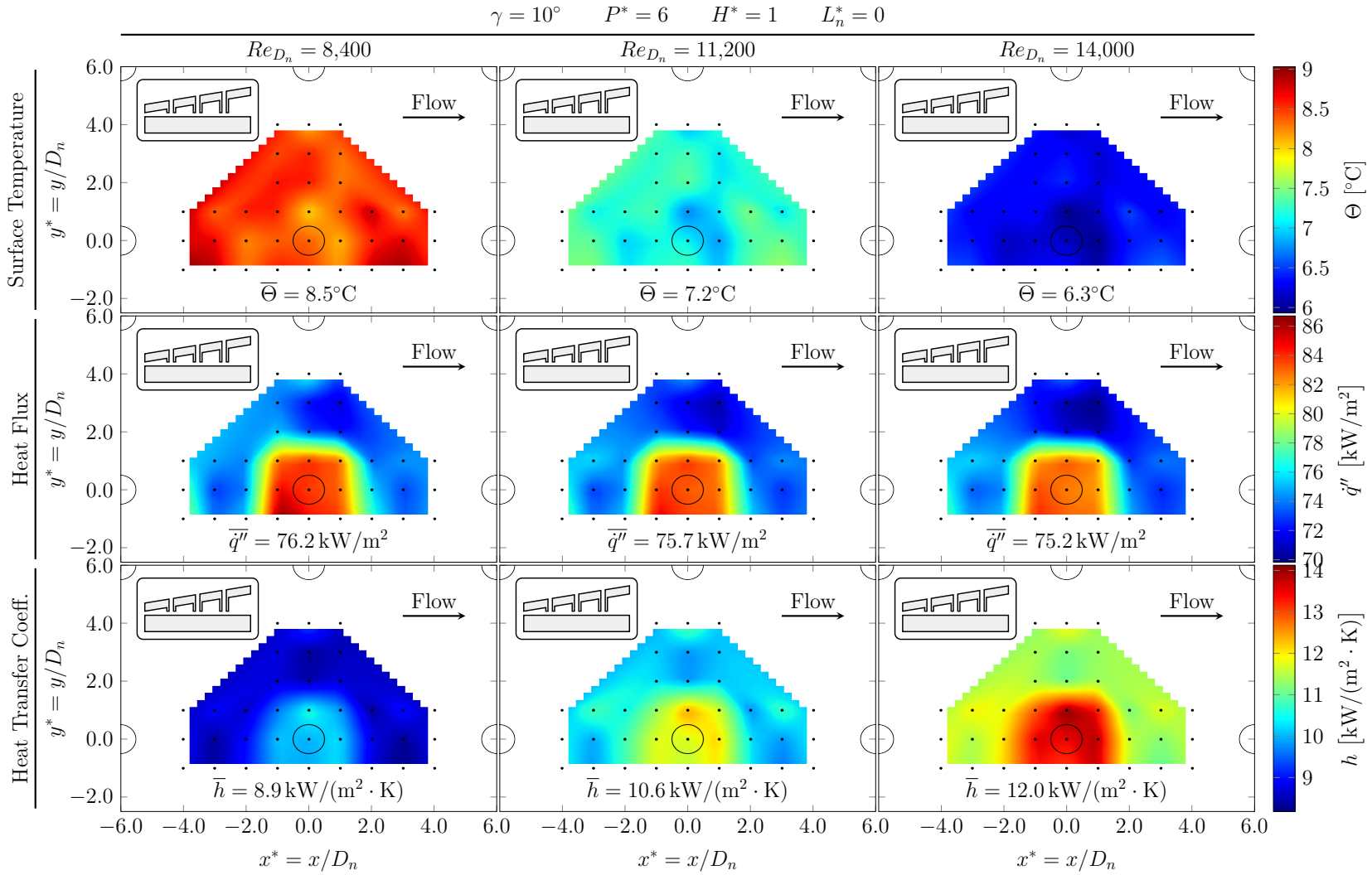

Figure E.5: Surface map comparison of variation with Reynolds number for 10° angled plate with P^*=6 and H^*=1

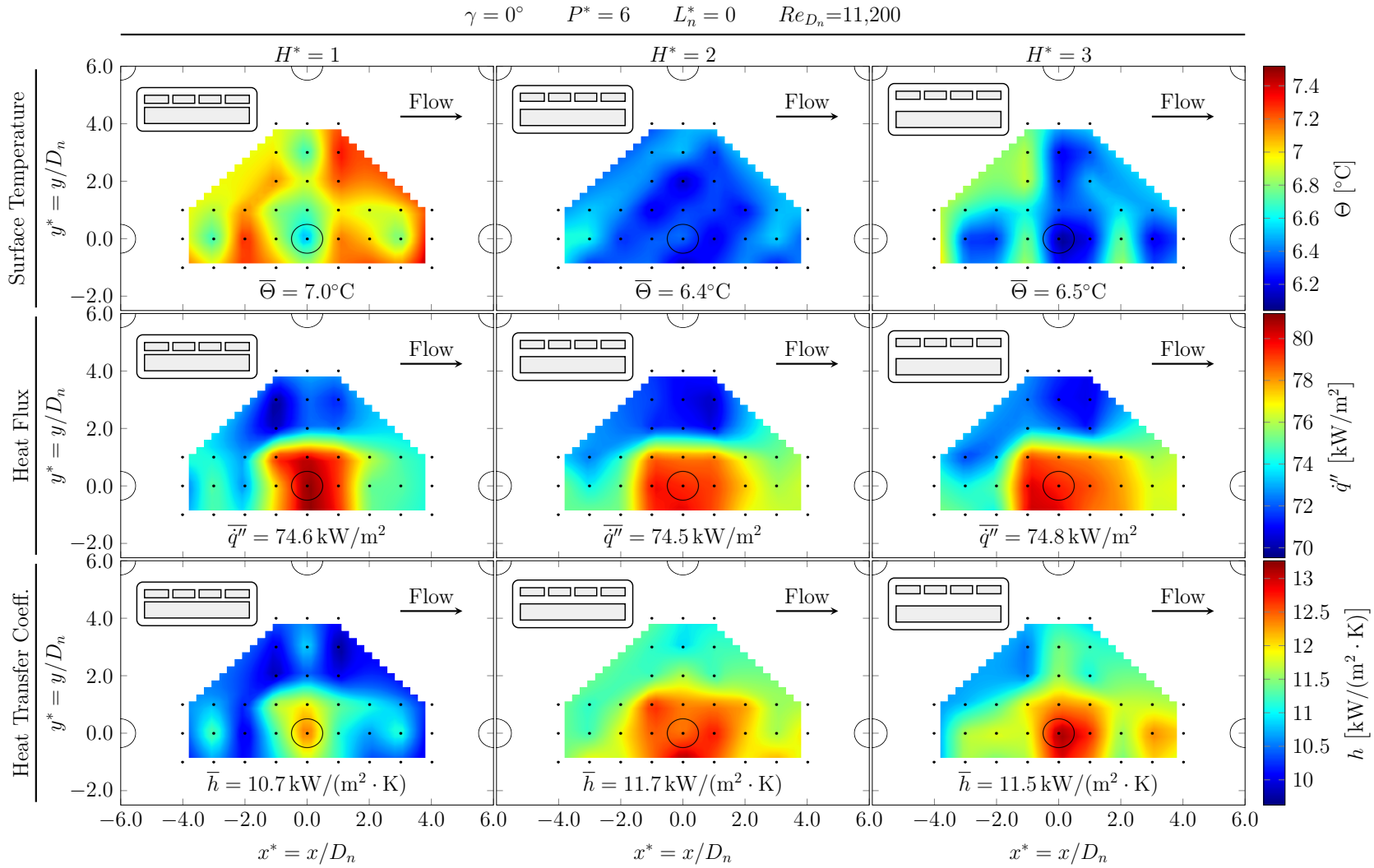

Figure E.6: Surface map comparison of variation with jet height for orifice plate with P^*=6 and Re_{D_n}=11,200

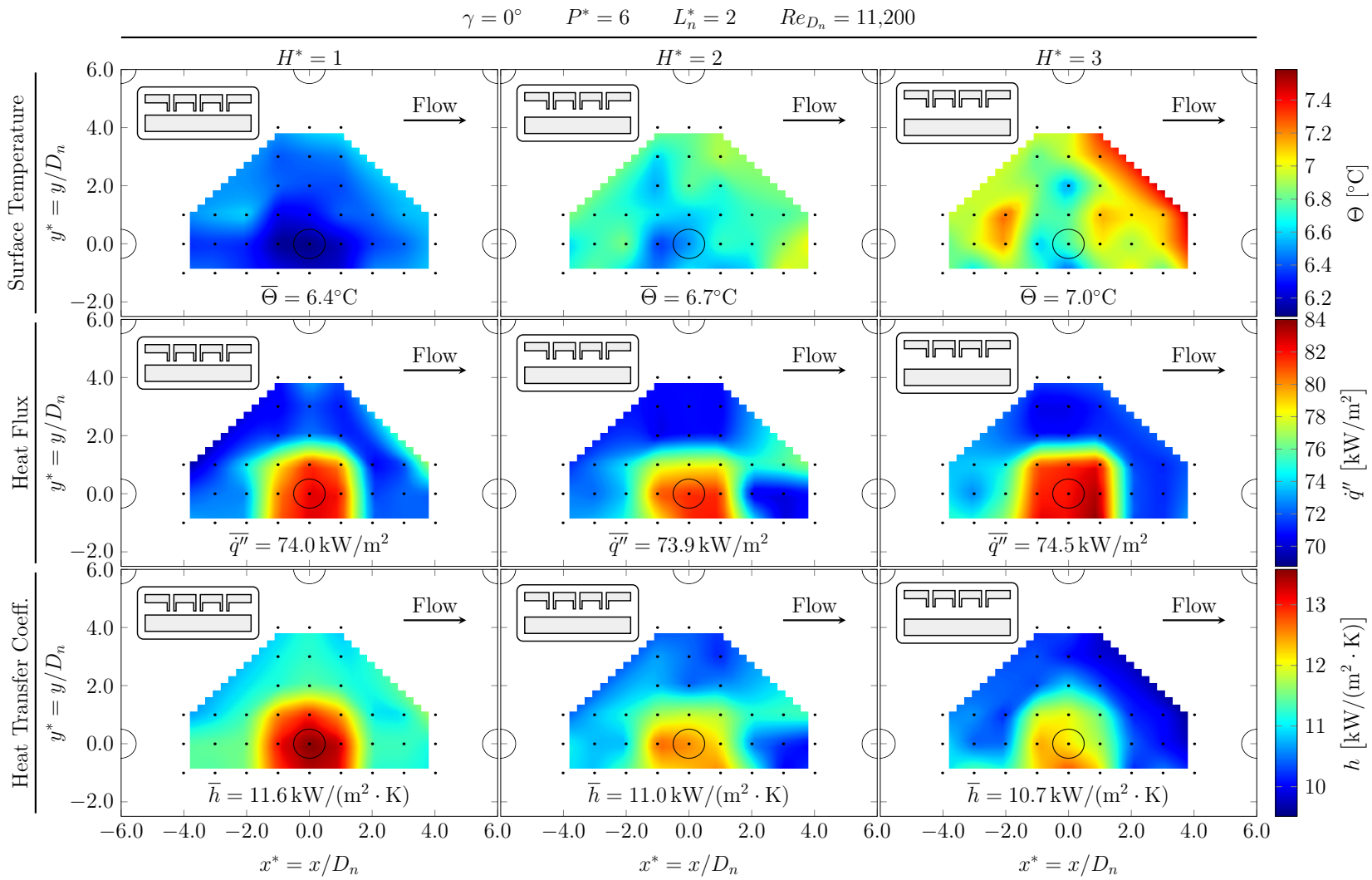

Figure E.7: Surface map comparison of variation with jet height for parallel nozzle plate with P^*=6 and Re_{D_n}=11,200

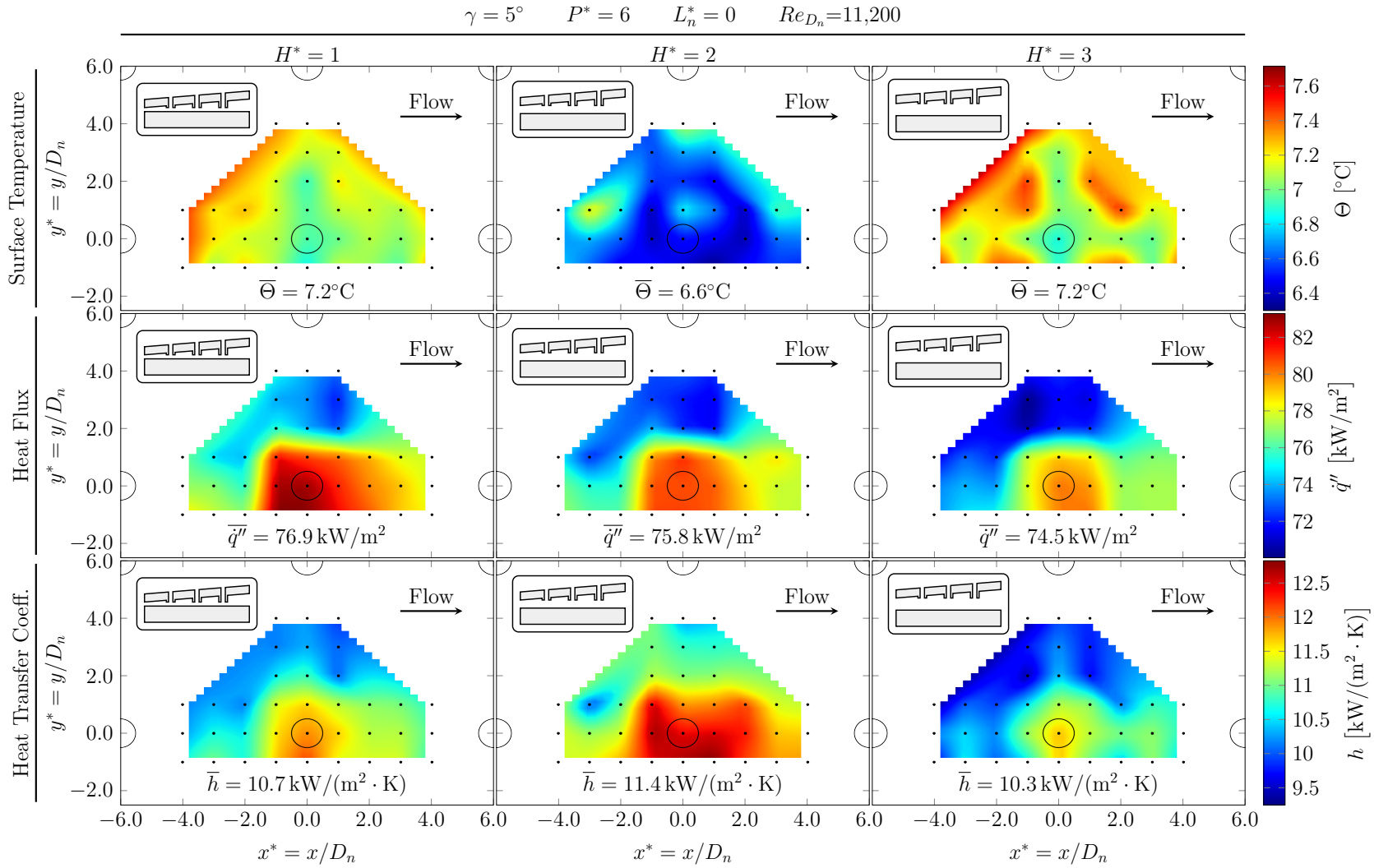

Figure E.8: Surface map comparison of variation with jet height for 5° angled plate with P^*=6 and Re_{D_n}=11,200

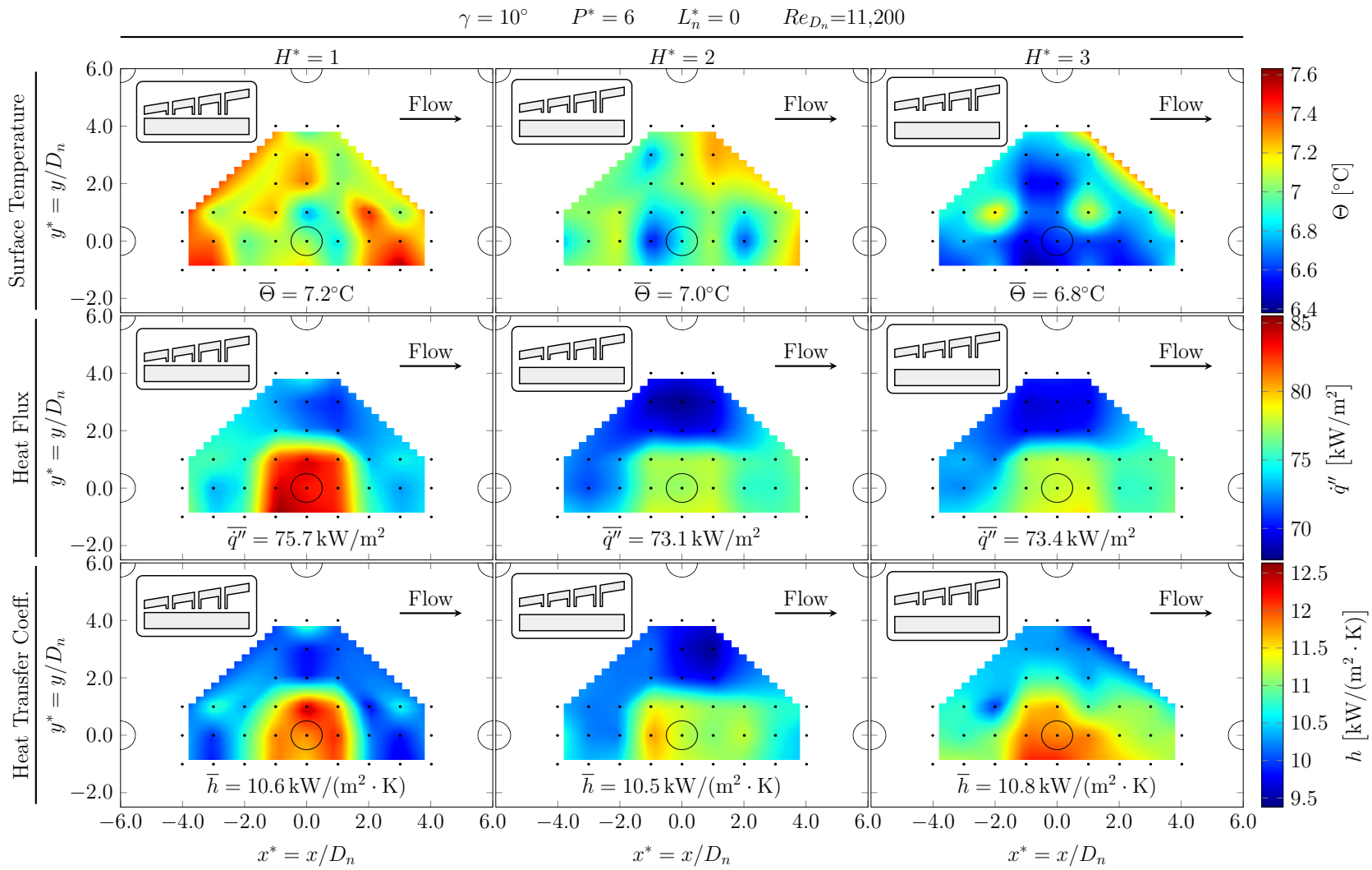

Figure E.9: Surface map comparison of variation with jet height for 10° angled plate with P^*=6 and Re_{D_n}=11,200

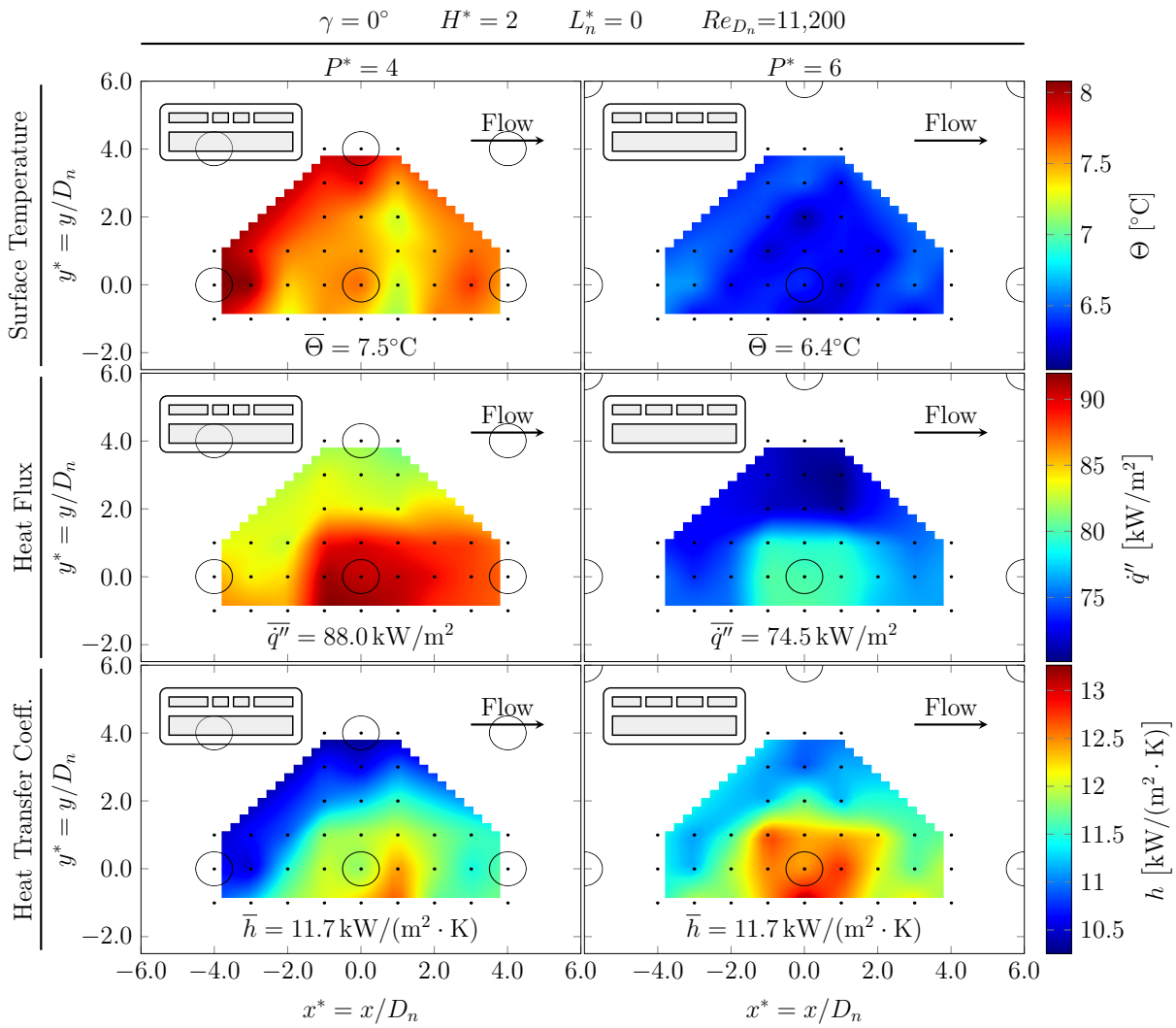

Figure E.10: Surface map comparison of variation with pitch for orifice plates with H^*=2 and Re_{D_n}=11,200

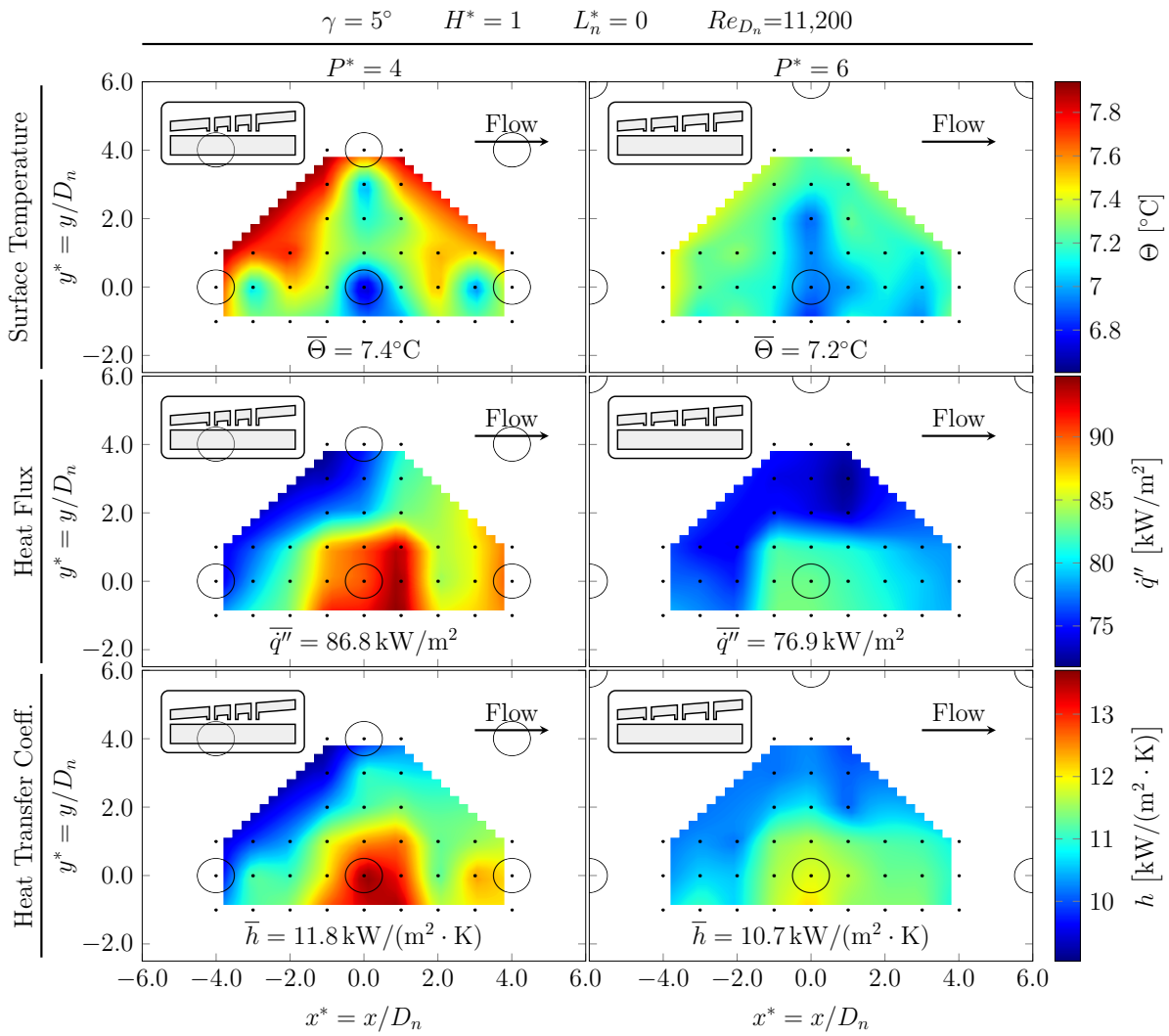

Figure E.11: Surface map comparison of variation with pitch for 5° angled plate with H^*=1 and Re_{D_n}=11,200

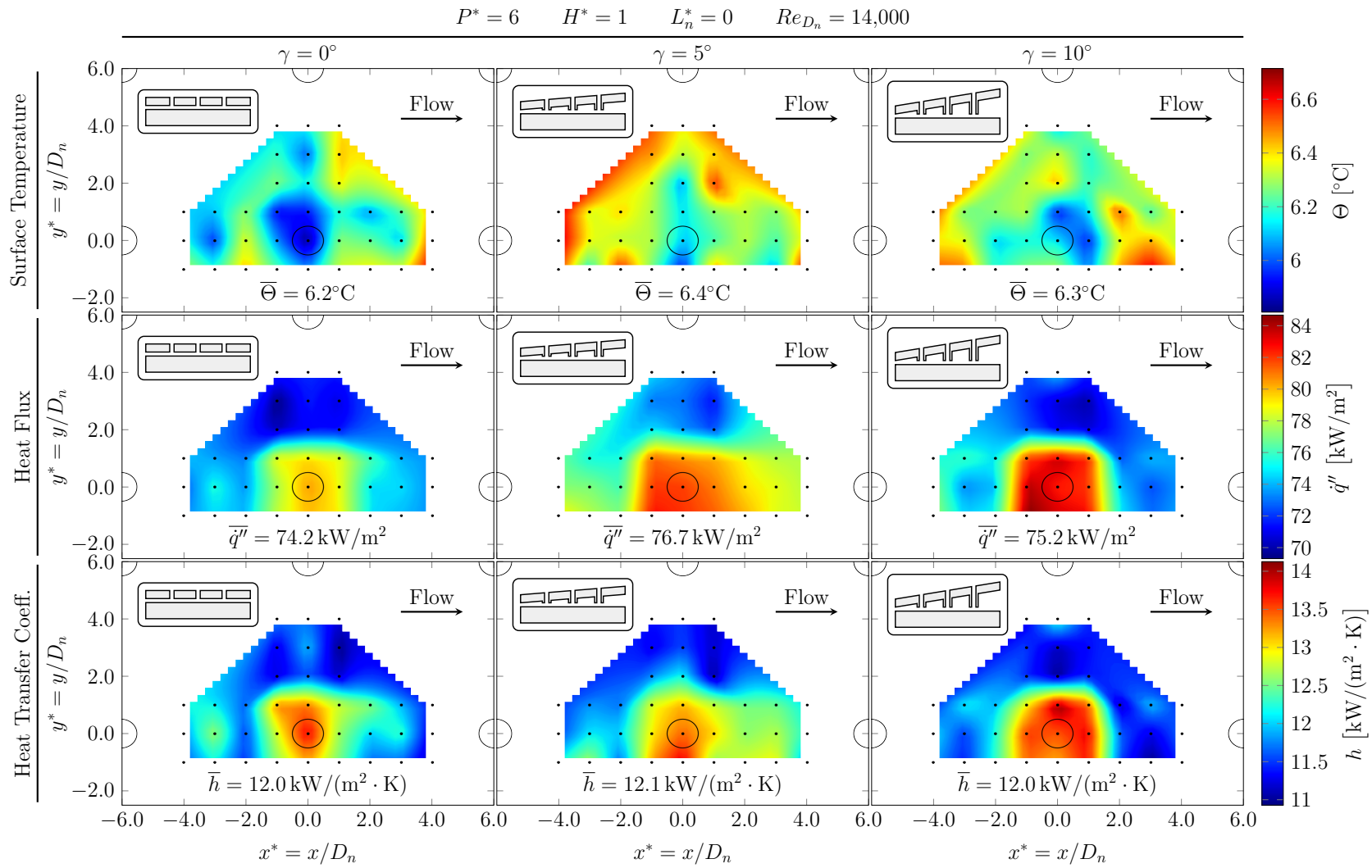

Figure E.12: Surface map comparison of variation with angle for P^*=6, H^*=1, and Re_{D_n}=14,000

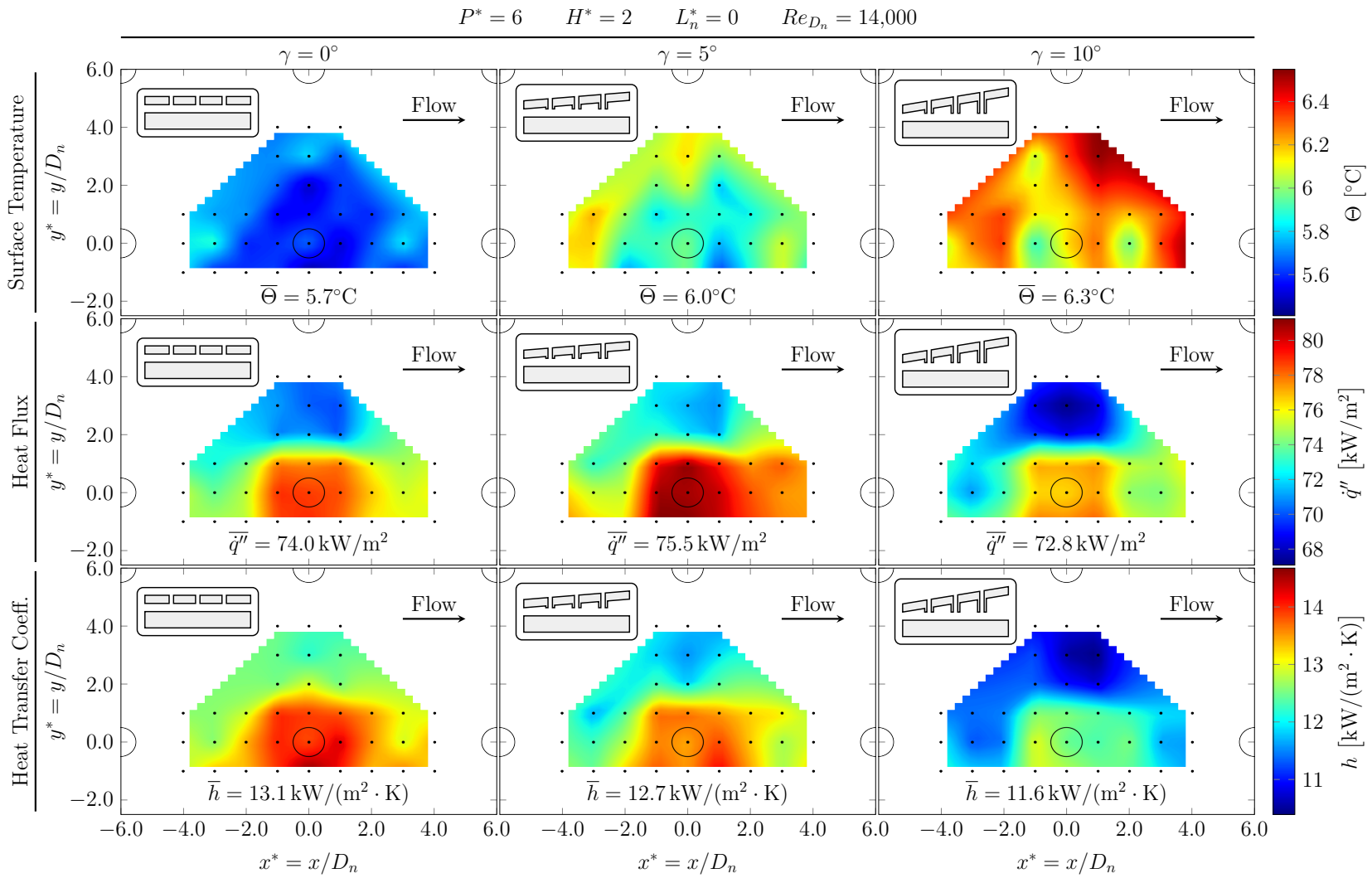

Figure E.13: Surface map comparison of variation with angle for P^*=6, H^*=2, and Re_{D_n}=14,000